Pulsed Power Technology and Its Applications to Plasma Science

Edited by Weihua Jiang, Keiichi Kamada and Tetuo Ozaki

March 6-7, 2008
National Institute for Fusion Science
Toki, Gifu, Japan

Abstract

In this proceedings, the papers presented at the symposium on “Pulsed Power Technology and Its Applications to Plasma Science” held at National Institute for Fusion Science on March 6-7, 2008 are collected. The papers reflect the present status and recent progress in the experimental and theoretical works on plasma science using pulsed power technology.

Keywords: high energy density plasma, warm dense matter, microwave, EUV, laser, plasma focus, z-pinch, high power ion beam, material processing, micro plasma.

Editor's Preface

The symposium on "Pulsed Power Technology and Its Applications to Plasma Science" was held at National Institute for Fusion Science on March 6-7, 2008. Forty scientists from universities and institute joined in fruitful discussions in the symposium. Twenty papers presented at the symposium are included in this proceeding. The papers cover wide range of science and applications using pulsed power technology. We would like to express our thanks to all authors, participants and National Institute of Fusion Science.

Weihua Jiang
Nagaoka University of Technology

Keiichi Kamada
Kanazawa University

Tetuo Ozaki
National Institute for Fusion Science

Contents

List of participants

M. Glyavin	(Institute of applied physics, Russian academy of science)
H. Ito	(Toyama University)
K. Masugata	(Toyama University)
H. Miyake	(Toyama University)
H. R. Yousefi	(Toyama University)
Z. P. Wang	(Toyama University)
K. Takasugi	(Nihon University)
Maeda	(Nihon University)
T. Yoshinaga	(Nihon University)
T. Ohshima	(Nihon University)
S. Ibuka	(Tokyo Institute of Technology)
M. Kanemaru	(Tokyo Institute of Technology)
J. Kikuchi	(Tokyo Institute of Technology)
J. Yamada	(Tokyo Institute of Technology)
K. Horioka	(Tokyo Institute of Technology)
E. Hotta	(Tokyo Institute of Technology)
T. Sasaki	(Tokyo Institute of Technology)
M. Watanabe	(Tokyo Institute of Technology)
H.Yamada	(Gunma University)
M. Sato	(Gunma University)
S. Furuya	(Gunma University)
N. Nomura	(Kumamoto University)
S. Katsuki	(Kumamoto University)
T. Kikuchi	(Utsunomiya University)
Y. Iizuka	(Utsunomiya University)
T. Higashiguchi	(Utsunomiya University)
Nishida	(Osaka University)
T. Ozaki	(National Institute for Fusion Science)
T. Tazima	
R. Ando	(Kanazawa University)
T. Kurihara	(Kanazawa University)
K. Aizawa	(Kanazawa University)
M. Kawamura	(Kanazawa University)
M. Ohbayashi	(Kanazawa University)
S. Iwano	(Kanazawa University)
S. Odawara	(Kanazawa University)
S. Matsuura	(Kanazawa University)
F. Kondo	(Kanazawa University)
K. Tamura	(Kanazawa University)
T. Hirochi	(Kanazawa University)
K. Kamada	(Kanazawa University)

DEVELOPMENT OF LASER TRIGGERED TIN DISCHARGE EUV LIGHT SOURCE

Junzaburo Yamada*, Zhu Qiushi, Nozomu Kishi, Masato Watanabe, Akitoshi Okino, Tohru Kawamura, Kazuhiko Horioka, and Eiki Hotta

Department of Energy Sciences, Tokyo Institute of Technology

4259, Nagatsuta, Midori-ku, Yokohama 226-8502, Japan

*yamada.j.aa@m.titech.ac.jp

ABSTRACT

Extreme ultraviolet (EUV) lithography is the most promising technology for 32 nm technology node. There are many issues for realizing EUV lithography, such as development of optical components and radiation sources. One of the most important challenging tasks is to develop an EUV light source. In present study, we are using tin (Sn) as EUV emitting material which is expected to improve conversion efficiency and are developing a new EUV light source called a laser triggered Sn discharge EUV light source. The temporal evolutions of EUV emission were compared for different laser irradiation energy. When the laser energy was 381 mJ, the EUV emission could not be observed. However, when the laser energy was reduced to 54 mJ, a continuous EUV emission could be observed on an output signal of EUV diode. From framing photographs measured with a high speed camera, it was considered that the position and the time of the maximum pinch were determined by the balance between the magnetic and the Sn plasma pressures.

I. Introduction

Owing to the high degree of integration of the semiconductor device, small electronics with high performance have appeared. To aim at further integration, a light source with shorter wavelength is required for the lithography. Extreme ultraviolet (EUV) light with wavelength of 13.5 nm is considered to be a promising candidate as a light source for next generation lithography [1]. However, higher output, reduction of debris generation, and longer lifetime are required for practical use of EUV light sources [2].

Xenon (Xe) and tin (Sn) are known as materials having strong emission spectra at wavelength of 13.5 nm. More attention is paid to Sn because Sn has higher conversion efficiency from input energy to the EUV energy, and the Sn EUV light source has been developed all over the world [3].

Since Sn is solid at room temperature, to get discharge produced plasma it is necessary to ablate Sn. Therefore, a laser was used to get Sn vapor by ablation. In this study, we have conducted experiments on the laser triggered Sn discharge EUV light source and effects of laser irradiation energy on EUV output have been investigated.

II. Laser triggered Sn discharge EUV light source

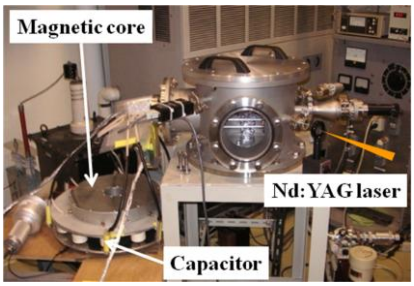

Fig.1 Sn discharge device

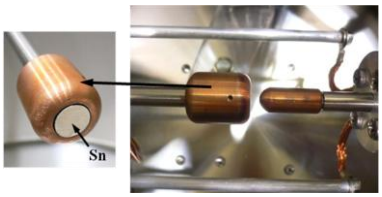

Fig.2 Electrodes for the Sn discharge

Figures 1 and 2 show photographs of the apparatus and the electrodes, respectively. A solid Sn rod was embedded in the center of one of the electrodes. An Nd:YAG laser (sure lite II-10, manufactured by Continuum), the maximum output energy of which was 650 mJ, was used to irradiate the Sn rod surface. The laser beam, which had a wavelength and a pulse width of 1064 nm and 4~7 ns, respectively, was focused on the surface of Sn rod by a lens of 300 mm focal length. The laser beam acted as a trigger of vacuum switch which was a light source as well and the ablated Sn vapor initiated the discharge in between the electrodes.

Figure 3 shows the schematic diagram of power supply circuit. The circuit consists of a magnetic core, a capacitor and a plasma load connected in series.

Figure 4 shows a typical current waveform. When a capacitor of 80 nF was used and the charging voltage of which was 20 kV, a current with amplitude of 9 kA and pulse width of 700 ns was supplied.

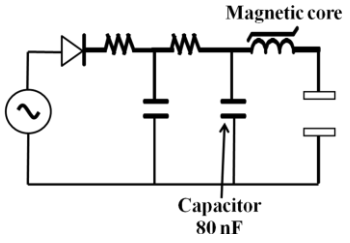

Fig.3 Schematic diagram of power supply

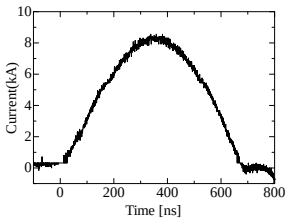

Fig.4 Current waveform

Experimental parameters were inter-electrode gap length, which could be changed from 4 to 10 mm, and laser irradiation energy, which could be varied from 23 to 399 mJ.

A photodiode (AXUV20HS1, manufactured by IRD) coated with Si/Zr (100/200 nm) was used to measure the EUV emission ranging from 11 nm to 18 nm.

A high speed framing camera (IMACON468, manufactured by Hadland), which had the gate pulse width of 10 ns, was used to measure the temporal evolution of the spatial distribution of plasma in the visible region.

Using a pinhole camera (pinhole diameter was 50 μm) equipped with an X-ray CCD and a band-pass filter (transmission wavelength region was 7~16 nm), time integrated EUV emission images were taken.

III. Experimental results and discussion

A. EUV emission characteristics

The temporal evolutions of EUV emission were compared for the different laser irradiation energy and the result is shown in Fig. 5. When the laser energy is 52 mJ, repetitive pulsed EUV emission (photodiode signal) can be observed. However, when the laser energy is increased to 381 mJ, the EUV emission cannot be observed. The cause of this phenomenon is considered as follows: Higher laser irradiation energy produces the larger amount of evaporated metal and hence higher pressure of produced vapor. This leads to the larger plasma

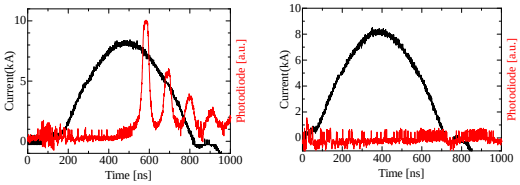

Laser energy: 52 mJ 381 mJ

Fig.5 EUV emission waveforms for different laser energy (capacitance: 80 nF, electrode gap length: 6 mm, and Sn anode is irradiated with laser beam)

radius. Since the azimuthal magnetic pressure generated by constant axial current is inversely proportional to the square of radius, the produced plasma with larger radius is difficult to be compressed by the magnetic pressure. Especially a small leakage current flowing in the non-saturation phase of magnetic core, which is not enough to compress the plasma, heats the produced plasma and it leads to the further increase of plasma radius. Therefore, if the main current begins to flow after the leakage current phase, during which the plasma expands, it becomes much more difficult for the main current to compress the plasma. Thus it is considered that no pinched plasma was obtained and hence no EUV emission was observed for higher laser irradiation energy.

B. Influence of magnetic core on plasma dynamics

In order to eliminate the influence of the magnetic core on the plasma expansion, the magnetic core was removed. Figure 6 shows EUV output waveforms observed when the magnetic core was removed. When the laser energy is 381 mJ, the EUV emission cannot be observed in the same way as that shown in Fig. 5 where the magnetic core is connected. However, when the laser energy is reduced to 54 mJ, a continuous EUV emission can be observed on an output signal of EUV diode in contrast to a pulse train of EUV emission observed in Fig. 5. Because the EUV output energy can be obtained by time integration of the EUV output power, this indicates that EUV emission energy increases in this case.

Figure 7 shows framing photographs taken with

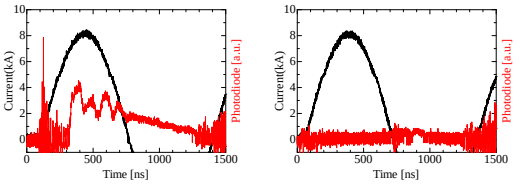

Laser energy: 52 mJ 381 mJ

Fig.6 Current and EUV output waveforms observed when a magnetic core is removed (capacitance: 80 nF, electrode gap length: 6 mm, Sn anode is irradiated with laser beam)

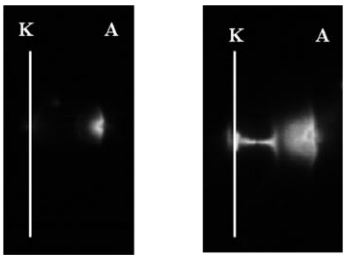

(a) magnetic core: used (b) magnetic core: not used

350 ns 300 ns

Fig.7 Framing photographs taken near the time of current peak (capacitance: 80 nF, laser energy: 52 mJ, electrode gap length: 6 mm, Sn cathode is irradiated with laser beam)

and without the magnetic core. When the magnetic core is used (Fig.7(a)), the pinch cannot be observed. However, when the leakage current is eliminated by removal of the magnetic core, plasma expansion by Joule heating is suppressed and effective compression of plasma occurs as observed in Fig.7(b). In the latter case, the kinetic energy obtained in the implosion phase is converted into thermal energy by collision at the maximum pinch and the plasma temperature becomes higher than that shown in Fig.7(a).

C. Plasma dynamics

It is important to understand the pinch mechanism to know how hot and dense plasma can be generated. In this section, plasma dynamics will be described. Figure 8 shows framing photographs and Fig. 9 shows the time integrated EUV emission images. From these figures, the following phenomena can be observed. The maximum pinch occurs at 354 ns after current rise and the EUV emission can be observed on the cathode side when the laser energy is 54 mJ. On the other hand, when the laser energy is 104 mJ, the maximum pinch occurs at 448 ns after current rise, which is later than that obtained for laser energy of 54 mJ, and the maximum EUV emission point moves to the anode side compared with that observed in the case for the laser energy of 54 mJ.

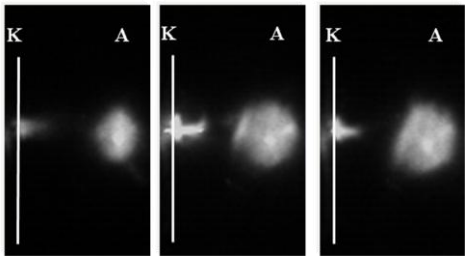

(a) 260 ns (b) 354 ns (c) 409 ns
laser energy: 54 mJ

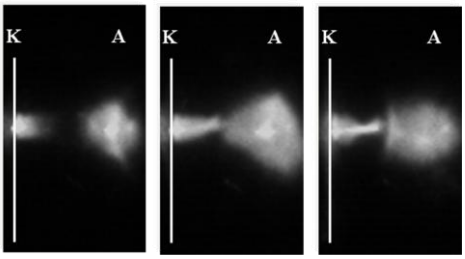

(a) 288 ns (b) 344 ns (c) 448 ns
laser energy: 104 mJ

Fig.8 Framing photographs taken in visible region (capacitance: 80 nF, electrode gap length: 7 mm, Sn cathode is irradiated with laser beam)

The cause of this phenomenon is considered as follows: The Nd:YAG laser irradiates the Sn rod surface and the plasma plume is produced on the cathode. When the laser energy is 54 mJ, a small amount of tin vapor is generated. And because the plasma pressure is low in this case, the implosion starts early in a discharge current much before its peak and the plasma pinches on the cathode side soon after the laser incidence. Hence the kinetic energy obtained is low. As a result, the temperature obtained at the maximum pinch becomes low. It is thought that low density and low temperature are factors which contributes to the result that EUV emission observed for the laser energy of 54 mJ is weak as shown in Fig. 9. When the laser energy is increased to 104 mJ, the larger amount of plasma is produced. Hence it is considered that the plasma pressure becomes higher than the magnetic pressure on the cathode side. Therefore, the pinch does not occur on the cathode side. The radius of the current layer, the plasma pressure, and the current value changes with time. Hence, the magnetic pressure which is inversely proportional to the square of radius of the current layer and proportional to the square of the current value changes with time.

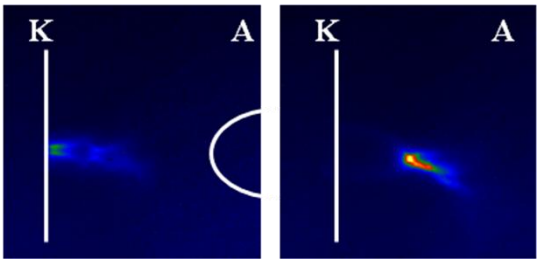

(a) laser energy: 54 mJ (b) laser energy: 104 mJ

Fig.9 Pinhole photographs taken in EUV region (capacitance: 80 nF, electrode gap length: 7 mm, Sn cathode is irradiated with laser beam)

Additionally the plasma pressure varies with the position between the electrodes. As a result, the position and the time of the maximum pinch are determined by the balance between the magnetic and the Sn plasma pressures.

IV. Conclusion

In this study, temporal evolutions of EUV emission were compared for the different laser irradiation energy. When the laser energy is 52 mJ, repetitive pulsed EUV emission (photodiode signal) can be observed. However, when the laser energy is increased to 381 mJ, the EUV emission cannot be observed. Higher laser irradiation energy produces the larger amount of evaporated metal and hence higher pressure of produced vapor. This leads to the larger plasma radius. Since the azimuthal magnetic pressure generated by axial current is inversely proportional to the square of radius, the produced plasma with larger radius is difficult to be compressed by the magnetic pressure. Especially a small leakage current flowing in the non-saturation phase of magnetic core, which is not enough to compress the plasma, heats the produced plasma and it leads to the further increase of plasma radius. Therefore, if the main current begins to flow after the leakage current phase, during which the plasma expands, it becomes much more difficult for the main current to compress the plasma. Thus it is considered that no pinched plasma was obtained and hence no EUV emission was observed for higher laser irradiation energy.

In order to eliminate the influence of the magnetic

core on the plasma expansion, the magnetic core was removed. However, when the laser energy is 381 mJ, the EUV emission cannot be observed in the same way as that shown in Fig. 5 where the magnetic core is connected. On the other hand, when the laser energy is reduced to 54 mJ, a continuous EUV emission can be observed on an output signal of EUV diode in contrast to a pulse train of EUV emission observed in Fig. 5. From framing photographs measured with a high speed camera, the followings are shown. The maximum pinch occurs at 354 ns after current rise and the EUV emission can be observed on the cathode side when the laser energy is 54 mJ. On the other hand, when the laser energy is 104 mJ, the maximum pinch occurs at 448 ns after current rise, which is later than that obtained for laser energy of 54 mJ, and the maximum EUV emission point moves to the anode side compared with that observed in the case for the laser energy of 54 mJ. When the laser energy is 104 mJ, the larger amount of plasma with higher pressure is produced and this leads to the larger plasma radius. The produced plasma with larger radius is difficult to be compressed by the magnetic pressure. It is considered that higher plasma pressure leads to the larger plasma radius and hence the pinch does not occur on the cathode side. The magnetic pressure may become larger than the plasma pressure somewhere in between electrodes and the implosion begins at this position in this case. Consequently, to obtain a pinch near the cathode, the radius of the current layer soon after the laser incidence should be made smaller. If the current rise rate could be increased, the current value soon after the laser incidence also could be increased and the radius of the current layer in the initial phase would be made smaller. Therefore, it is planned to increase the current rise rate by decreasing the circuit inductance. The result will be appeared in the future.

Acknowledgement

This work was partially supported by NEDO and JSPS Grant-in-Aid for Scientific Research (A), Japan.

References

1) Katsuhiko Murakami, Shinji Okazaki, “EUV Lithography and Exposure Tool”, J.Plasma Fusion Res., Vol.79, No.3 (2003) pp. 221-225

2) Eiki Hotta, “Discharge Produced Plasma Light Sources - Present Status of Discharge Produced Plasma Light Sources Development”, J.Plasma Fusion Res., Vol.79, No.3 (2003) pp. 245-251

3) Naoya Iizuka, “Optimization of a Gas Jet-Type Z-pinch Plasma Light Source for EUV Lithography”, Tokyo Institute of Technology Master’s Thesis (2007) p.8

GENERATION OF EUV BY PLASMA FOCUS DEVICE WITH GAS-PUFF OPERATION

H.Yamada, M. Sato and K. Shimoda

Department of Electronic Engineering, Gunma University,
1-5-1 Tenjin-cho, Kiryu, 376-8515, Japan

ABSTRACT

We reduced the number of the condensers to make lower the temperature of the pinched plasma and generation of the soft X-ray was suppressed. We performed the experiments with the grazing-incidence spectroscope to analyze the wavelengths of the EUV light. From the spectral lines, generation of the EUV light of 13.5 nm was verified. We improved our small plasma focus device to the gas-puff style to increase the EUV output. In the gas-puff style, the peak value at the first peak became about twice higher than that in the mixed gas style.

Keywords: plasma focus, EUV, gas-puff operation

1. Introduction

Recently, with miniaturization of semiconductors, the wavelength of light source used for the lithography becomes shorter. Therefore development of the light source is an urgent task. The EUV (Extreme Ultra-Violet) light source is noticed for future lithography, because a Mo/Si multilayer mirror was developed. EUV is obtained from a high temperature and high density plasma by DPP (Discharge Produced Plasma) and LPP (Laser Produced Plasma). The plasma focus is a type of DPP and also is well known as an inexpensive device and a compact source of EUV[1)]. It can produce the high temperature and high density plasma easily. And also it can convert electrical energy to heat energy efficiently. About the debri, plasma focus device can prevent it because magnetic pressure generates and it is flown over the Z-axis. The EUV output for EUV lithography is needed 115W at intermediate point or 1kW at luminous point. The purpose of our research is a development of the EUV light source and an improvement of its output.

We have performed the experiments with a 120 kJ plasma focus device[2)] and a small plasma focus device for many years. The 120 kJ plasma focus device has been used to investigate generation of soft x-rays. On the other hand, the small plasma focus device has been used to generate a EUV light. For the small plasma focus device, there were two problems. First problem was the temperature of the plasma. Though the stored energy of our small plasma focus device was 5 kJ (about 1 kJ in operation), soft x-rays were detected in the output of a photo diode. This means that the temperature of the plasma is higher. To solve this problem, we reduced the number of condensers. It was expected that the temperature of the plasma became low by decreasing of the discharge current. Second problem was the intensity of the EUV light. To increase the output of the EUV light, we improved the small plasma focus device to gas-puff style[3)] (with gas-puff operation). In gas-puff style, the current sheet composed from only helium ions moved fast, and the xenon ions as the heavy atom were puffed onto the inner electrode. As a result, it was expected that the output of the EUV light increased.

In this paper, details of the small plasma focus device with gas-puff operation and the results obtained by our experiments are presented.

2. Experimental Arrangement

Figure 1 shows the schematic drawings of the experimental setup and the four stages in plasma focus operation. In the small plasma focus device, the four stages in plasma focus operation are same as those in the usual plasma focus devices. (1) Breakdown Phase; when the charged voltage applies between inner electrode and outer electrode, breakdown occurs on the surface of the insulator. The current sheet (a layer of columnar plasma) is produced. (2) Run down Phase; the current sheet is accelerated toward the electrode upper part in Fig. 1. At this time, the gases existed in front of the current sheet are ionized and collected. (3) Collapse Phase; the current sheet which reaches to the top of the inner electrode moves radially toward the center axis of the inner electrode by Lorentz force. (4) Focused Phase; the current sheet moved radially compress the plasma toward the center axis of the inner electrode. The compressed plasma becomes the high temperature and high density plasma. Afterward, the plasma breaks up because of instability of the plasma but various electromagnetic waves are generated. In the case of gas-puff style, a fast opening valve is firstly operated. With the delay time of several milliseconds, the condenser bank shown in Fig. 1 is triggered. Operation of the plasma focus device is same as mentioned above, but small amount of xenon gas is puffed immediately before focused phase. Xenon gas puffed from a hole located at the center of the inner electrode is ionized by the pinched plasma, and xenon ions are generate EUV lights.

Our small plasma focus device is consisted of a condenser bank, a vacuum vessel, several cables and a fast opening valve. The condenser bank is composed from four condensers which are connected in parallel. The each capacitance of these condensers is 3 μF. The vacuum vessel is made of aluminum. In the vessel, a plasma focus device is located. The schematic drawing of the plasma focus device is shown in Fig. 2. The plasma focus device is consisted of an inner and an outer electrode. Between the electrodes, an insulator is located. These electrodes are made of copper and the sizes of those electrodes are also shown in Fig. 2. This plasma focus device is a squirrel cage type, and the outer electrode is consisted of 12 copper rods of which diameter are 8 mm. Along the axis of the inner electrode, a small hole is drilled to pass through xenon gas. The diameter of the hole is 3 mm. The insulator is made of Pyrex glass of which thickness is 5 mm. The outer diameter and the length of the insulator are 30 mm and 39 mm, respectively. Each condenser and the electrodes are connected through 12 coaxial cables to make lower the inductance.

In the case of gas-puff operation, a fast opening valve is used. The cross sectional view of the valve is shown in Fig. 3. This valve is consisted of a magnetic coil, an iron hammer, a titanium valve and a stainless housing. This device is located between the plasma focus device and a gas bomb, and is used for puffing the xenon gas as a working gas onto the inner electrode. The power source for the magnetic coil is the condensers. The total capacity and the maximum charged voltage of the condensers are 150 μF and 10 kV, respectively. In the experiments, the condensers are charged to 2 kV, and the gas pressure of the gas bomb is set at 2 atm. When a current flows to the magnetic coil, the iron hammer is moved and the titanium valve is opened. Through the opened small space, a small amount of the xenon gas is flowed into the inner electrode. The titanium valve is closed by a return spring instantly. Since there is a time delay from moving of the titanium valve to puffing of the xenon gas onto the inner electrode, a delay pulsar is used to triggering of the condenser bank. The delay time by the delay pulsar was ranged from 5 to 8 ms.

In the experiments, a Rogowski coil was used to measure the discharge current, and a PIN diode and a photo diode (IRD, AXUV20HS1) were used to detect the soft X-ray and the EUV light generated from the pinched plasma. In front of the PIN diode, the beryllium foil of which thickness was 25 micrometers was set as a filter. The PIN diode can detect the soft X-rays of which wavelength is less than 2nm. A Si/Zr filter was vapor-deposited onto a light receiving part of the photo diode. The thicknesses of the silicon and the zirconium were 100 and 200 nm, respectively. By this Si/Zr filter the photo diode can detect the EUV light of which wavelength is 12~14 nm and the soft x-ray of which wavelength is less than 2nm. The spectroscopic measurement was performed with a grazing-incidence spectroscope to analyze spectrums of the EUV light which generated from pinched plasma. The experimental arrangement is shown in Fig. 4.

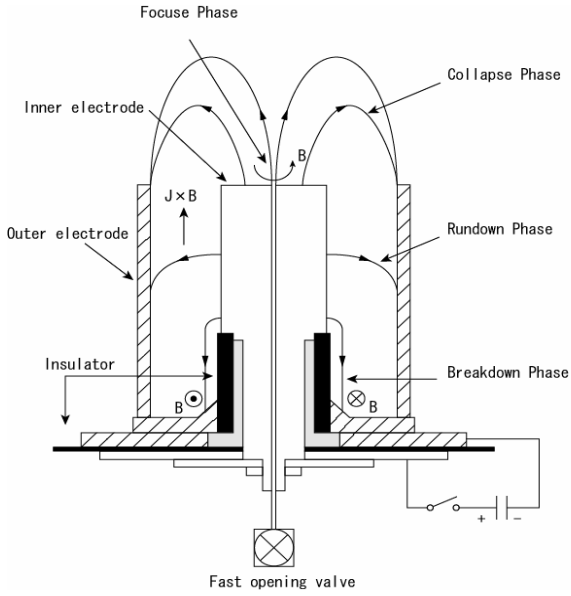

Fig. 1 The schematic drawings of the experimental setup and the four stages in plasma focus operation.

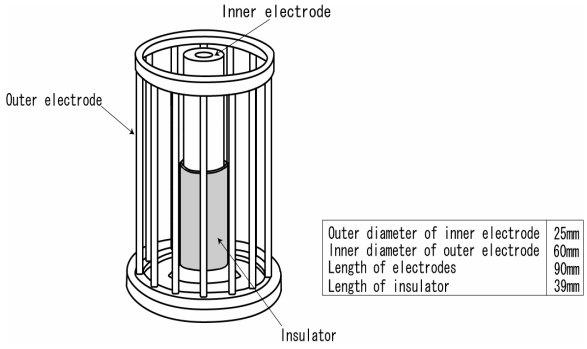

Fig. 2 The schematic drawing of the plasma focus device.

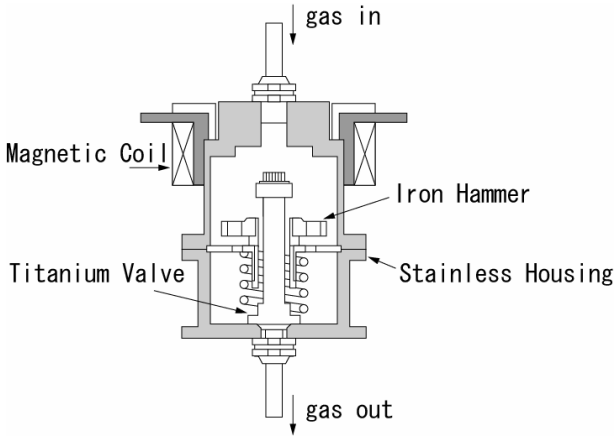

Fig. 3 The cross sectional view of the fast opening valve.

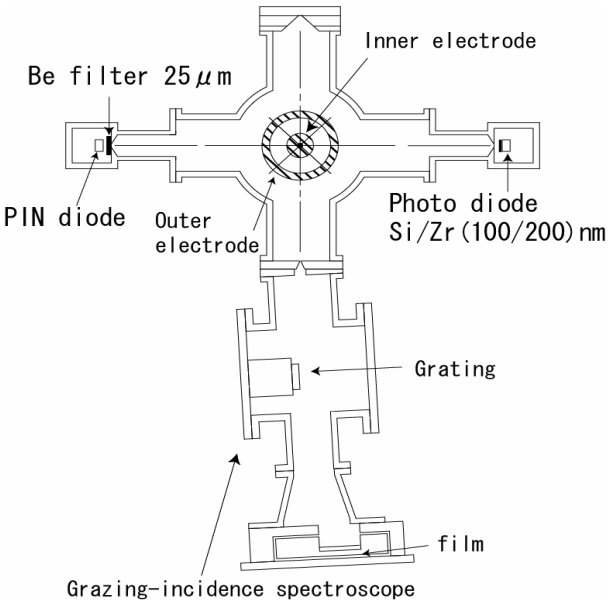

Fig. 4 The experimental arrangement.

3. Experimental Results

In the early experiment with the small plasma focus device, the number of the condensers was four; the total capacitance of the condenser bank was 12 μF. When the experiments were performed with the charged voltage of 15 kV, the maximum values of the discharge currents reached to 200 kA. This experiment was performed by a mixed gas style; a driving gas was the helium gas of 0.95 torrs, and the xenon gas of 0.05 torrs was mixed to it as a working gas. The typical waveforms of the discharge current and the diode signals are shown in Fig. 5. In this figure, the signal with the PIN diode was obtained. This means that the soft x-rays were generated in this experiment. From this result, the signal by the photo diode was mainly composed from EUV signal, but was also included the signal by the soft x-rays. This may be caused by the higher temperature of the pinched plasma. Therefore we reduced the number of the condenser bank from four to three. The total capacitance of the condenser bank became 9 μF. When the experiments were performed with the charged voltage of 15 kV, the maximum values of the discharge currents reduced to 150 kA. The conditions of the gases were same as those shown in Fig. 5. The typical waveforms of the discharge current and the diode signals are shown in Fig. 6. In the signal with the PIN diode shown in Fig. 6, the sharp signal was not seen, and the

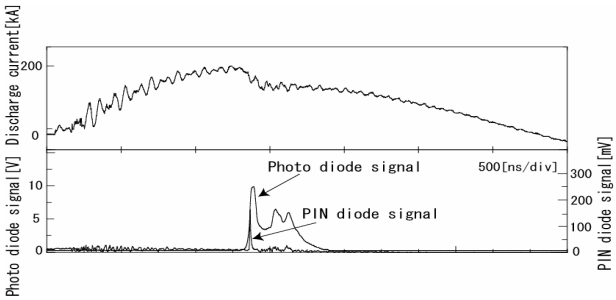

Fig. 5 Waveforms of early experiment with the small plasma focus device.

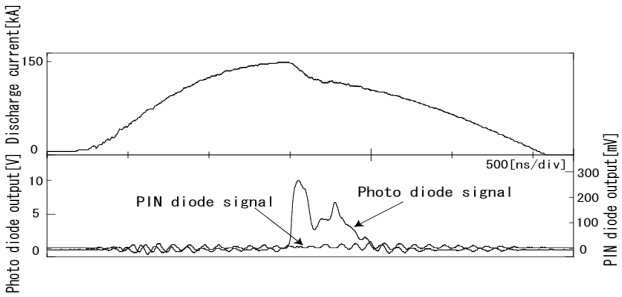

Fig. 6 Waveforms obtained with reduced condensers.

signal became a background oscillation. This means that generation of the soft x-ray is suppressed. From this result, it is considered that the photo diode signal is composed from only the EUV components and the soft x-ray components are not included in it. This may be caused by the lower temperature of the pinched plasma.

Figure 7 shows the spectrogram of the xenon plasma obtained with the grazing-incidence spectroscope. In Fig. 7 the figure shown at upper side was obtained by scanning the spectrogram, and that shows the densities of the spectrogram as a function of the wavelength. Figure 7 were obtained by superimposing the EUV light generated by ten experiments. These ten experiments were performed with the same parameters of the experiment shown in Fig. 6. The oval lines shown in Fig. 7 show the spectrum lines caused by the transition of $4d^8$-$4d^7 5p$ in xenon ions. The oval line shown in right side corresponds to the EUV light of 13.5 nm, and generation of the EUV light of 13.5 nm was verified.

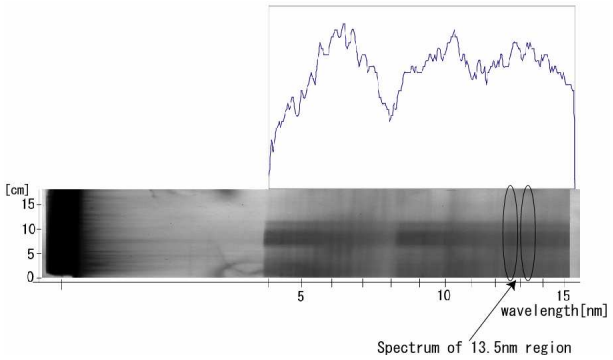

Fig. 7 Spectrogram of the xenon plasma.

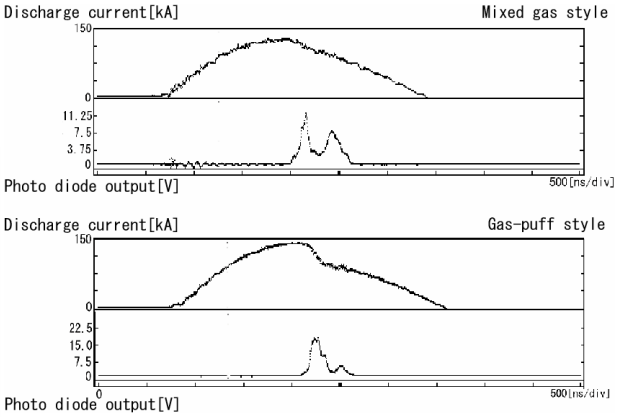

Fig. 8 Photo diode signals of gas-puff style and mixed gas style

Figures 8 show the experimental results with and without gas-puff operation. Here the experiment with gas-puff operation is so called as a gas-puff style and the experiment without gas-puff operation is so called as a mixed gas style. In the mixed gas style, the driving gas was the helium gas of 0.95 torrs, and the xenon gas of 0.05 torrs was mixed to it as a working gas. In the gas-puff style, the driving gas was the helium gas of 0.2 torrs and the working gas was puffed onto the inner electrode. The experiment was performed with the delay time of 7.0 ms. From comparison of the figures, two features are made clear. Firstly the dip in the discharge current is sharp in the gas-puff style. This may be caused by the faster velocity of the current sheet, because it is composed from only light helium ions. Secondly the signal of the photo diode becomes high in the gas-puff style; the peak value at the first peak becomes about twice higher than that in the mixed gas style.

Two peaks were seen in these photo diode signals. Since the first peak appeared at the same time with the dip in the discharge current, it is considered that it was the EUV signal generated by the pinched plasma. We carried out following experiments to investigate the second peak. Since the photo diode have a pin hole as shown in Fig. 9, the field of view of the photo diode changes with the distance from the photo diode. In the experiments mentioned above, the photo diode was located at the center of a measurement port; as like the PIN diode shown in Fig. 9. In this location the electrodes are located in the field of view, and there is a possibility that the copper ions sputtered from the inner electrode affect the EUV signal obtained with the photo diode. Therefore we moved the photo diode as shown in Fig. 9. In this location the electrodes are not located in the field of view, and it is considered that the effect by the copper ions decreases. The experiments in the gas-puff style were performed by location shown in Fig. 9, and the experimental results are shown in Fig. 10. The experimental conditions were same as that shown in Figs. 8 of the gas-puff style. From Fig. 10 the first peak

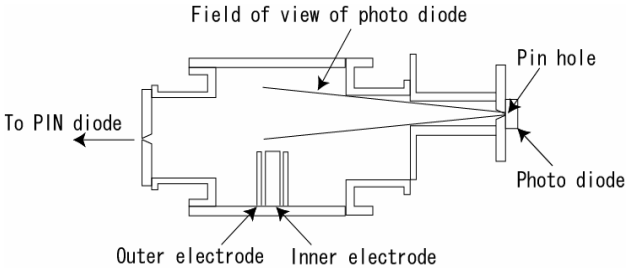

Fig. 9 The field of view of the photo diode.

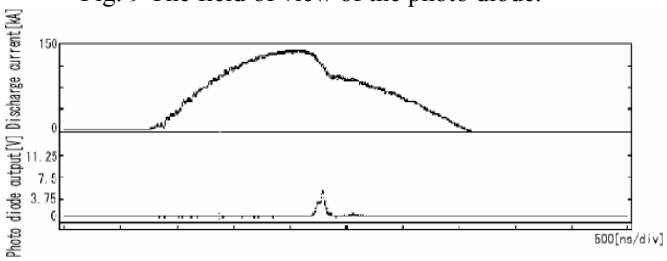

Fig. 10 The result which is not included over the inner electrode.

in the photo diode signal becomes low and the second peak disappears. Former means that the large amount of the EUV light is generated around the inner electrode. Latter also means that the second peak is composed from the EUV light which is generated around the inner electrode. It is considered that the second peak is caused by the copper ions sputtered from the inner electrode; the copper ions sputtered from the inner electrode by an electron beam are injected into the pinched plasma, and generate the EUV light.

4. Summary

We reduced the number of the condensers to make lower the temperature of the pinched plasma and generation of the soft X-ray was suppressed. We performed the experiments with the grazing-incidence spectroscope to analyze the wavelengths of the EUV light. From the spectral lines, generation of the EUV light of 13.5 nm was verified. We improved our small plasma focus device to the gas-puff style to increase the EUV output. In the gas-puff style, the peak value at the first peak became about twice higher than that in the mixed gas style. It was considered that the second peak appeared in the photodiode signal was caused by the copper ions sputtered from the inner electrode.

References

1) For examples;
I.V. Fomenkov, N. Böwering, C.L. Retting, S.T. Melnychuk, I.R. Oliver, J.R. Hoffman, O.V. Khodykin, R.M. Ness and W.N. Partlo, J. Phys. D, **37** (2004) 3266.
2) J. Mizuno, K. Shimoda and M. Sato, NIFS-PROC-61 (2004) 90.
3) H. Kitaoka, A. Sakurai, T. Yamamoto, K. Shimoda and K. Hirano, J. Phys. Soc. Jpn., **64** (1995) 4191.

DYNAMICS OF LASER-ASSISTED DISCHARGE PLASMS FOR EUV SOURCES

Sunao Katsuki, Nobufumi Tomimaru, Hideki Imamura, Takashi Sakugawa, Takao Namihira and Hidenori Akiyama

Graduate School of Science and Technology, Kumamoto University
39-1 Kurokami 2-chome, Kumamoto City, Kumamoto 860-8555, Japan

ABSTRACT

This paper describes the dynamics of laser-assisted discharge plasmas for an extreme ultraviolet (EUV) source. A pulsed laser light was focused on the tin cathode surface to form vapor jet across 5 mm long anode-cathode gap where pulsed power was applied later on. Time-resolved EUV photography was conducted by using a gated EUV pinhole camera in addition to visible high speed photography. The measurement shows that the EUV is emitted only from the neck of the plasma, which is as a result of m = 0 magnetohydrodynamic (MHD) instability. The hot neck plasma starts showing up near the laser spot on the cathode and moves away from the cathode. This movement of the neck plasma results in the enlargement of the EUV emissive region acting as its source.

I. Introduction

A Z-pinch plasma is one of the candidates of extreme ultraviolet (EUV) sources for the next generation of semiconductor lithography[1,2]. Both the huge radiation power exceeding 180 W at wavelength of 13.5 nm in 2% bandwidth and the one year operation without maintenance are required for its commercial use. There are several key technologies to approach the commercial EUV source. Tin is the most efficient target material for 13.5 nm emission[3,4]. The rotating disc electrodes (RDE) technology[5,6] is capable of handling the huge amount of heat exceeding 50 kW due to electrical input and preventing serious electrode consumption. The laser-assisted discharge (LAD) technology[5,6] helps to produce a localized dense gas distribution near the solid or liquid target surfaces, which enables to compress the plasma quickly and efficiently in comparison with conventional gas-fed Z-pinches[7,8]. The localized gas distribution also results in stabilizing the location of high density hot plasmas. In order to improve the conversion efficiency (CE) from the energy consumption in the plasma to the EUV emission yield, it is important to know the plasma dynamics and how the EUV emission takes place. This letter describes the dynamics of a laser–assisted discharge plasmas based on time-resolved visible and EUV photography. It also discusses a direction to improve the CE.

II. Experimental Setup and Procedure

FIG 1 shows a coaxial birdcage discharge head, which enables us to optically access the plasma easily. The discharge head consists of a planer tin cathode and a 6 mm diameter stainless steel ball anode. 7 ns long pulsed laser light (532 nm, Nd:YAG, Minilite, Continuum) was irradiated with a fluence of 10^{10} W/cm^2 to the cathode surface to deliver tin vapor jet across the 5 mm electrode gap. FIG. 2 shows the over all diagram of the experimental system. Voltage application to the gap was delayed a certain time from the laser irradiation because the ablated tin vapor jet expands dynamically and it takes hundreds ns to form the distribution for the breakdown.

In this paper we define *dt* as the time interval between the laser irradiation and the breakdown, which is one of the key factors for the plasma formation. 300 ns is the minimum value for *dt* to produce stable and reproducible discharge for the experimental condition. No discharge occurs at *dt* smaller than 250 ns. The minimum value of *dt* for the stable operation depends mainly on the gap distance, the laser irradiation fluence as well as the target material. The plasma was driven by a low inductance circuit with 42 nF capacitor bank, which is charged up to 27 kV by a repetitive pulsed power generator. The repetition rate of the operation was 10 Hz, which is determined by the laser device. The EUV emission intensity was monitored by a fast EUV photodiode (AXUV5, IRD) after passing through a spectrum band pass filter (2% at 13.5 nm) using two silicone/molybdenum multilayer mirrors. The plasma current was monitored using a calibrated pickup coil. A high speed camera (Quick E, Stanford Scientific Research) was employed to observe the visible emission from the plasma. A gated EUV pinhole camera was developed to obtain the time-resolved EUV images of the plasma. A 50 μm diameter pinhole was covered by a 200 nm thick zirconium film to specify the wavelength range between 4 and 17 nm. The EUV emission was visualized by a two-staged micro channel plate (MCP, Hamamatsu) with a phosphor screen. The MCP was driven by a 5 ns and 2 kV handmade pulse generator based on the semiconductor driven Marx circuit[9]. Since both visible and EUV cameras work as single frame operation, a set of sequential images was obtained by the combination of images at different times in different shots, based on the reproducibility of the operation.

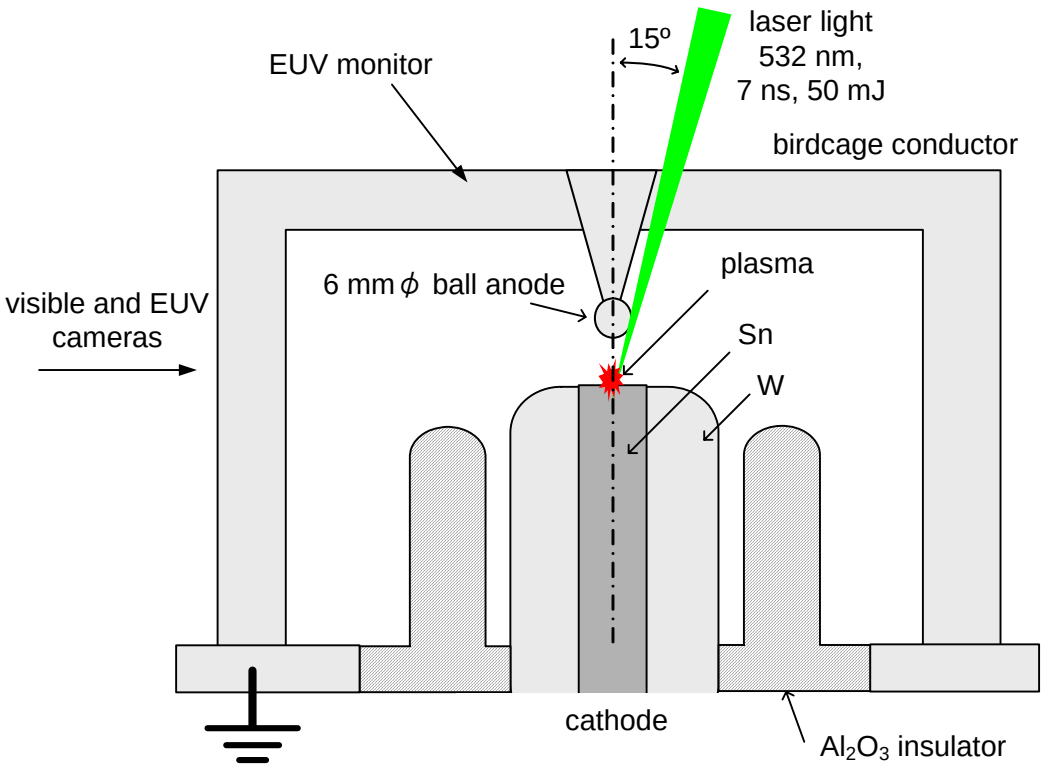

FIG. 1 Birdcage discharge head for the laser-assisted discharge.

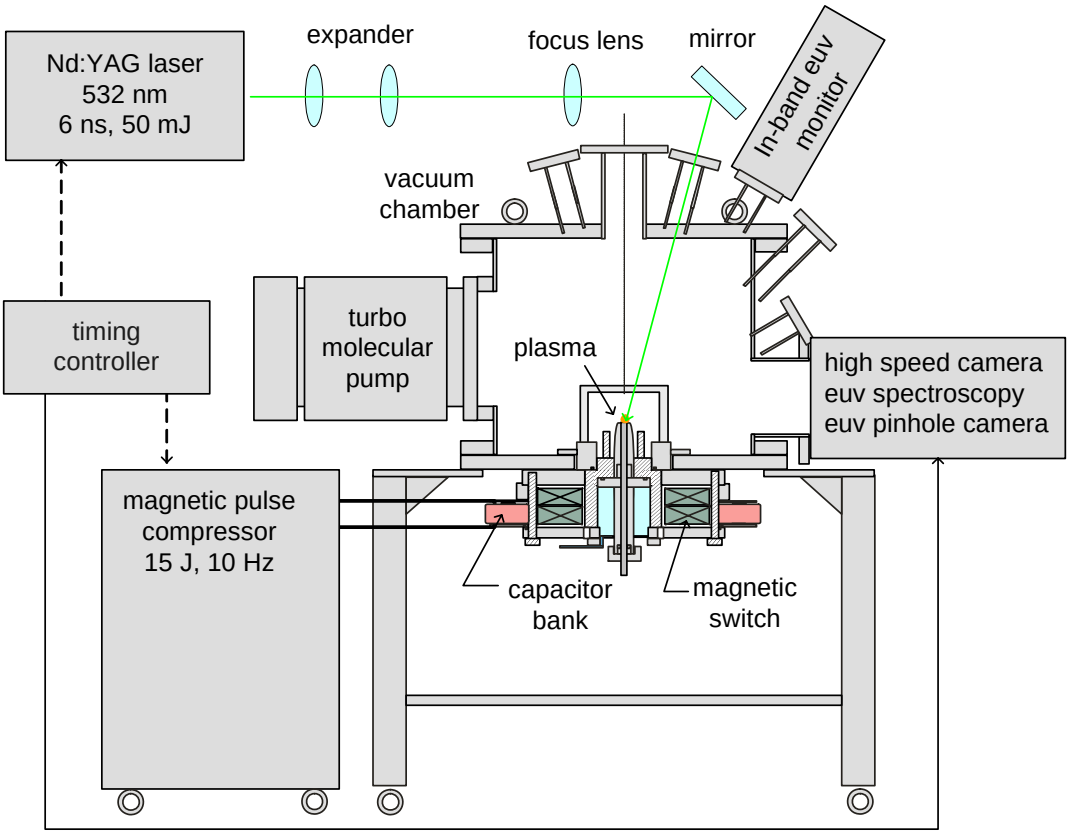

FIG. 2 Experimental setup.

IV. Results and Discussion

FIG. 3 shows the waveforms of the plasma current I_p and the signal of the EUV monitor for dt = 300 ns. t = 0 indicates the time when the current starts to increase rapidly. The EUV emission begins immediately after the current starts flowing through the plasma, and the strong emission occurs when the current becomes the maximum. The early emission is owing to the localization of gas achieved by the LADP technology. The LADP technology enables us to use extremely short current pulses to drive pinch plasmas efficiently, while the conventional gas-fed discharge needs long pulses to gather low density gas.

FIG. 4 shows the sequential time-resolved visible images of the plasma observed from the horizontal direction. The number shown in each image is identical to the time in FIG 3. At t = 10 ns, the emission is localized near the laser spot even after the time more than 300 ns passed from the laser irradiation. A weak emission, which is similar to an anode column in the low pressure direct current discharge, connects the bright part to the anode. A strong pinch occurs near the laser spot on the cathode at approximately t = 50 ns, which is due to the m = 0 magnetohydrodynamic (MHD) instability[7]. Afterward the bright spot moves away from the cathode, while another plasma shows up and covers the cathode surface. A thin neck bridges two plasma clouds, and the neck moves away from the cathode together with the clouds. Finally the neck disappears at approximately t = 110 ns when the EUV emission is fading away. During the EUV emission the voltage of 20 kV is across the anode-cathode gap. Most of the voltage seems to occur along the neck between the clouds, resulting in the generation of huge electric field of the order of 1 MV/cm. The electric field accelerates both electrons and ions inversely between the clouds. The accelerated electrons collide with the dense gas cloud in the anode column, and the ions

bombard the cathode surface, resulting in the surface plasma showing up after t = 65 ns. This exploding plasma lasts for several microseconds even after the current flow ends.

FIG. 5 shows the time-integrated and sequential time-resolved EUV images of the plasmas for the same condition as those in FIGs 3 and 4. Sight of each image is identical to the rectangular box region in the left-hand image in FIG 4. Repetitive 50 shots were accumulated in each image. The time–integrated image shows EUV emissive region is widely distributed between the anode-cathode gap. Approximately 60 % of the total emission takes place at the 1.1 mm long filamentary region near the cathode, which is quite stable and reproducible. According to the time-resolved images, the EUV emission began to occur near the laser spot at t = 50 ns, afterwards the EUV emissive region moved away from the cathode. Instantaneous size of the EUV emissive region at t = 80 ns is 700 × 300 $(\mu m)^2$. The EUV emission faded away at approximately t = 120 ns. This movement coincides with that of the plasma neck in FIG 4. During the movement, the EUV emission became intense in the range including 65 and 80 ns, when also the plasma current was at the maximum level. The current density in the neck plasma is estimated to be 30 MA/cm^2. The observation suggests the possible driving force of the hot plasma movement should be the zipper effect [7]. Variation of the intensity of the images is consistent with the EUV emission intensity measurement shown in FIG 3. The comparison between the visible and EUV images indicates that EUV emission occurs only from the neck between the clouds and neither from the anode column nor from the cathode surface plasma.

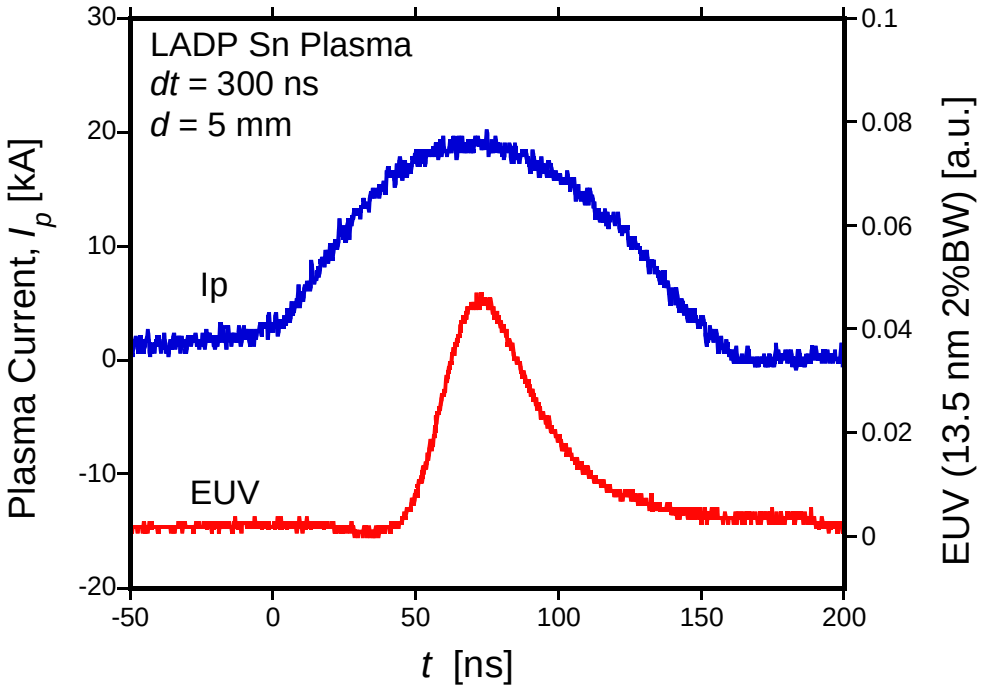

FIG. 3 Waveforms of the plasma current and the EUV emission intensity.

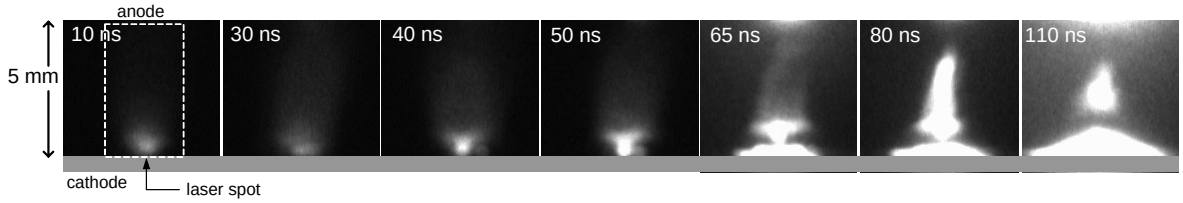

FIG. 4. Temporal variations of visible images of the laser assisted discharge plasmas taken by high speed camera with an acquisition time of 2 ns. The number in each image shows the time identical to that in FIG 3.

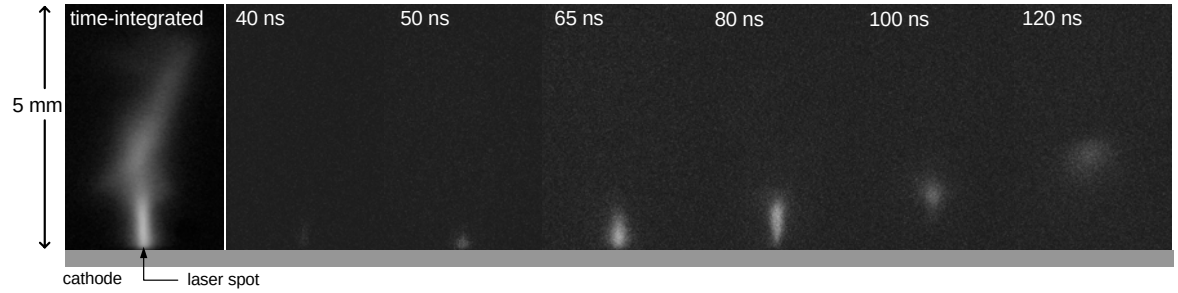

FIG. 5. A time-integrated EUV image (LEFT) and temporal variations of EUV images of the laser assisted discharge plasmas taken by a gated pinhole EUV camera. Time resolution is 5 ns. 50 shots are accumulated in each image. The number in each image shows the time identical to that in FIG 4.

V. Conclusion

In conclusion, the time-resolved observation indicates that the laser–assisted discharge plasma behaves dynamically during the discharge. The EUV emission occurs at the hot neck part of the plasma, which moves along the anode-cathode gap. This movement of the hot plasma enlarges the EUV emissive region, which is not favorable for EUV sources. The suppression of the dynamic behavior of the hot plasma would reduce the source size and improve the conversion efficiency.

Acknowledgement

This work has been supported by both New Energy and Industrial Technology Development Organization (NEDO) and 21st Century COE program on “Pulsed Power Science”.

References

1) V. Banine, R. Moors, Proceedings of SPIE, 4343, 203-214 (2001)
2) V. Bakshi (ed), EUV Sources for Lithography, SPIE, Bellingham (2005)
3) G. O'Sullivan, P.K. Carroll, J. Opt. Soc. Am. 71, 227 (1981).
4) M. Lysaght, D. Kilbane, N. Murphy, A. Cummings, P. Dunne, G. O’Sullivan, Phys. Rev. A 72, 014502 (2005)
5) V.M. Borisov, J. Phys. D: Appl. Phys. 34, 3254-3265 (2004)
6) J. Jonkers, Plasma Sources Sci. Technol. 15, S8-S16 (2006)
7) M.A. Liberman, J.S. De Groot, A. Toor, R.B. Spielman, Physics of High-Density Z-Pinch Plasmas, Springer-Verlag (1998)
8) S. Katsuki, A. Kimura, Y. Kondo, H. Horita, T. Namihira, T. Sakugawa, H. Akiyama, J. Appl. Phys. 99(1), 013305 (2006)
9) T. Heeren, T. Ueno, D. Wang; T. Namihira, S. Katsuki, H. Akiyama, IEEE Trans. Plasma Sci. 33 (4), 1205 - 1209 (2005)

Ultrashort, intense laser pulse propagation in a capillary discharge-produced plasma channel

T. Higashiguchi, H. Terauchi, J. Bai, M. Hikita, and N. Yugami

Department of Electrical and Electronic Engineering and Center for Optical Research & Education (CORE), Utsunomiya University, Yoto 7-1-2, Utsunomiya, Tochigi 321-8585 Japan

ABSTRACT

We have observed the energy spectrum of accelerated electrons, using a capillary discharge-produced plasma channel with a length of 1 cm to guide high-intensity laser pulses with the laser intensity of 5×10^{16} W/cm^2. The most probable energy of the accelerated electrons was measured to be 1.3 MeV. Simple laser wakefield analysis revealed that the high-intensity laser through the plasma channel formation of the electrons.

I. Introduction

The interaction of an ultrashort intense laser pulse with a wide variety of optical waveguides has been demonstrated in various applications, including a short wavelength laser,[1] high-order harmonic generation,[2] and charged-particle acceleration.[3] An ultrashort, high-intensity laser pulse cannot only be used for high-field plasma physics under extreme conditions, but can also yield temporally resolved ultrafast phenomena in a plasma. An intense laser-produced plasma wakefield has attracted significant attention as an efficient high energy laser accelerator with energy ranging from MeV to GeV, using a slow discharge-produced capillary plasma waveguide.[4] Such a waveguide produces a plasma channel with a parabolic hollow electron density structure profile.[5,6] The plasma channel is necessary to guide ultrashort high-intensity laser pulses along lengths much longer than the Rayleigh length. The radial electron density parabolic profile of a plasma channel is given by $n_e(r)=n_{e0}(r=0)+\Delta n_e(r/r_0)^2$, where $n_{e0}(r=0)$ is the axial electron density and Δn_e is the difference at radius $r=r_0$. In the case of a Gaussian laser profile, the matched spot size of the plasma channel is evaluated to be $w_0=[r_0^2/(\pi r_e \Delta n_e)]^{1/4}$, where r_e is the classical electron radius.[7]

We proposed a low laser intensity operation to demonstrate a practical compact electron source with a short bunch for x-ray generation and/or high power THz source.[8,9] High-energy laser wakefield electron sources for efficient x-ray sources that use a high power laser system with peak power ranging from a few TW to 40 TW have been developed. A 7-MeV from a gas-jet target energy has been demonstrated with an laser intensity of 5×10^{18} W/cm^2.[10] This method, however, requires a large facility and has a low repetition rate, resulting in limited application possibilities. The low laser intensity would require for high repetition rate operation. Our approach is to use of a capillary discharge-produced plasma waveguide with a discharge current of 400 A with a low laser intensity in the range of 10^{16} W/cm^2. Despite its low laser intensity, the electron energy would not be compromised by use of a capillary discharge-produced plasma waveguide to realize generation for MeV electrons.

In this paper, we report the observation of accelerated electrons using a 1-cm long capillary discharge-produced plasma channel to guide high intensity laser pulses with the laser intensity of 5×10^{16} W/cm^2. A most probable energy of accelerated electrons of 1.3 MeV was observed. A simple laser wakefield analysis revealed that the high-intensity laser passing through the plasma channel initiated the accelerated electrons.

II. Experimental setup

Figure 1 shows a schematic diagram of the experimental setup. A 10-Hz Ti:Sapphire laser at a wavelength of 800 nm produced a maximum energy of around 40 mJ with a pulse width of 100 fs [full width at half-maximum (FWHM)]. The laser pulse was then focused onto the entrance of a capillary discharge-produced plasma waveguide with a focal diameter of 36 μm (FWHM) in vacuum using a lens with a focal length of 17 cm. The focused laser intensity was fixed at 5×10^{16} W/cm^2. The capillary waveguide consisted of a 1-cm long alumina (Al_2O_3) tube with a diameter of 300 μm. Argon gas flowed through a gas cell to the pumping vacuum chamber

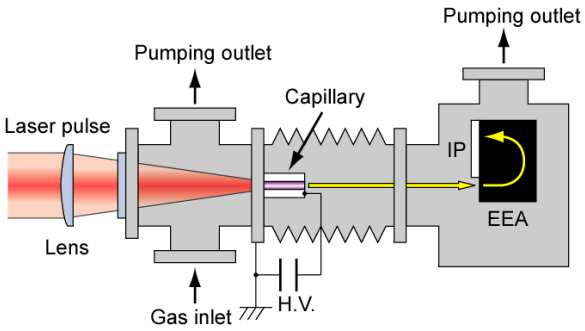

Fig. 1. Schematic diagram of the experimental setup.

for optical diagnostics and an electron energy analyzer (EEA), such that the steady-state pressure between the gas cell and the vacuum section was uniform. The pressure at the vacuum chamber was maintained at less than 1×10^{-6} Torr. A stainless-steel ground (earth) electrode was coaxially connected at the entrance of the capillary, with the laser pulse entering the capillary through a 300-μm diameter hole. The cathode, also the cupper electrode, was located at the exit of the capillary in a high-vacuum less than 1×10^{-6} Torr. The storage capacitance was 2 nF, charged to between 20 and 30 kV. The electron density of the plasma channel in the capillary was measured using a laser interferometer. The beam profiles of the laser pulse through the plasma channel were measured using a charge-coupled device (CCD) camera. The energy spectrum of the accelerated electron beam was observed using the ESA coupled with an imaging plate (IP).

III. Experimental results

Figure 2 shows the temporal histories of the discharge voltage and current at the discharge voltage of 30 kV. The pulse width of the discharge current was observed to be 100–150 ns (FWHM). The maximum discharge current was about 500 A at the discharge time delay of around 150 ns. A strong dip in the current waveform was observed at 100 ns due to the rapid increase in the load inductance (dL/dt). This suggests that plasma compression occurred at this time.

The plasma channel was measured by use of the laser interferometer. Figure 3 shows a radius distribution of the electron density in the uniform central section of a 1-cm long, 300-μm diameter capillary, and this profile was converted from a fringe shift by use of the Abel transformation. The axial electron density and difference of the density were $n_{e0} \approx 3\times10^{17}$ cm^{-3} and $\Delta n_e \approx 3.3\times10^{17}$ cm^{-3} with r_0=150 μm, respectively. The matched spot diameter of the plasma channel is largely independent of the shape of the electron density profile.[11] As a result,

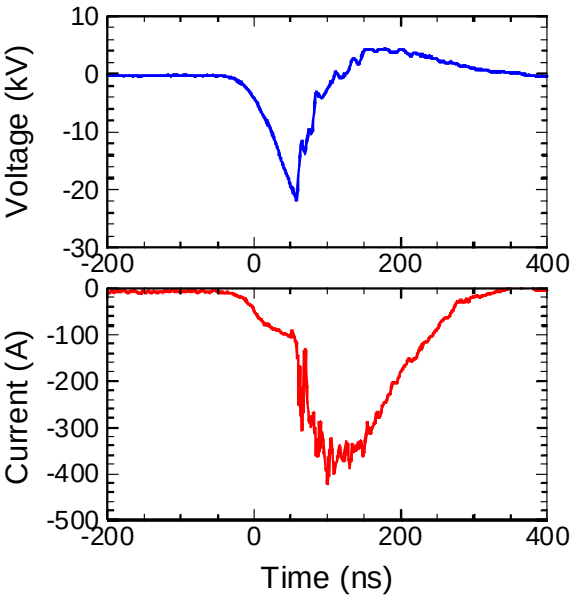

Fig. 2. Temporal histories of the discharge voltage (a) and its current (b), respectively.

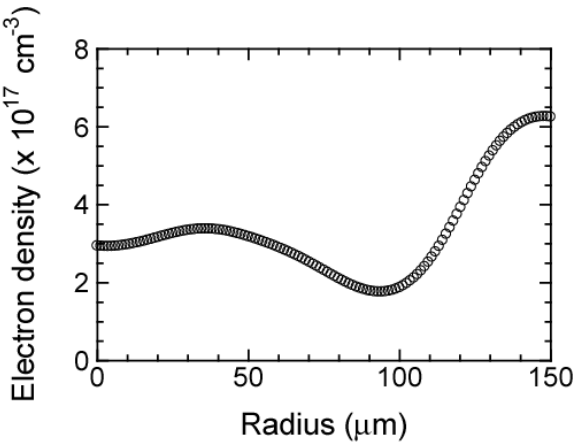

Fig. 3. Radial distribution of the electron density.

the matched spot diameter is evaluated to be 51.8 μm. Note that the average electron density on the longitudinal axis of the capillary was measured to be 3×10^{17} cm^{-3}.

Figure 4 shows photographs of the laser beam profile through the capillary without and with the discharge plasma channel at a discharge time delay of 150 ns. The transmitted coefficient of the laser pulse through the plasma channel with the electron plasma density of 3×10^{17} cm^{-3} was maximized at a discharge time delay of around 150 ns and a discharge current of 400 A. A comparison of these photographs showed evident optical guiding using the plasma channel. Without the plasma channel, the output beam through the capillary could not be

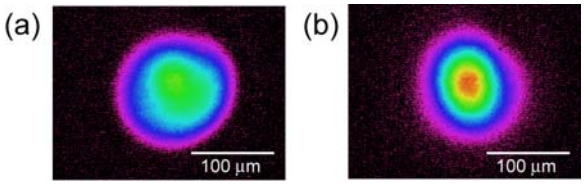

Fig. 4. Photographs of the transmitted laser profile at the capillary exit without (a) and with (b) the plasma channel.

propagated. As a result, the transmission coefficient was less than 1%. The beam diameter of the transmitted laser pulse, on the other hand, was observed to be about 36 μm (FWHM). According to the plasma channel measurement, this observed spot diameter was consistent with a matched spot diameter of 51.8 μm. The transmission coefficient was achieved to be 75% with the plasma channel. Note that, the intensities of the output beam cannot be compared with these photographs due to the different scale of the CCD camera sensitivity.

We demonstrated electron acceleration application using a 1-cm long capillary discharge-produced plasma channel. Figure 5 shows the energy spectrum of the accelerated electrons on the IP in the exit of the EEA with an average magnetic field of 6 kGauss, covering energies from 0.5 to 7 MeV. The most probable energy of the energy spectrum was 1.3 MeV at the discharge time delay of 150 ns, corresponding to an electron plasma density of 3×10^{17} cm^{-3}. The high energy slope of the energy spectrum by the spectral sensitivity of the IP. Even a small dip at 1.6 MeV was reproduced. Note that there was no laser intensity dependence of the energy spectrum in this paper due to the limitation of the output energy in the present laser system. The energy increasing would become measureable after further amplification of the laser beam and/or the increase the capillary plasma channel length. In addition, the flux of the accelerated electrons without the plasma channel was lower than the noise level in the detection system.

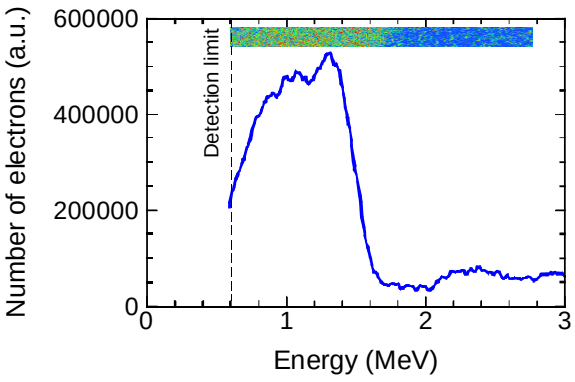

Fig. 5. Energy spectrum of the accelerated electron beams the discharge time delay of 150 ns.

Based on the linear theory of the laser wakefield,[7] the maximum electric field of the wakefield was roughly evaluated to be 4 MV/cm under experimental conditions of electron density on the order of 10^{17} cm^{-3} and a laser intensity of 5×10^{16} W/cm^2 with a pulse width of 100 fs (FWHM). The Rayleigh length in free space without the capillary was evaluated to be less than 0.5 mm. The maximum energy without the plasma channel, therefore, was expected to be 400 keV, which was lower than the experimental value of 1.3 MeV. Laser electron acceleration assisted by the capillary discharge-produced plasma channel was effective in producing high electron energy. As a result, the maximum energy of the accelerated electrons was expected to be 0.82 MeV for an interaction length of 2 mm, which is shorter than the capillary length of 1 cm. In the present case, the axial density perturbation was also evaluated to be $\Delta n/n \approx 0.14$. This simple analysis reproduced the observed maximum energy of the accelerated electrons.

IV. Summary

We have reported experimental results of a 1-cm long capillary discharge-produced plasma channel to be irradiated low intensity laser with the intensity of 10^{16} W/cm^2. The transmitted coefficient of the 800-nm laser pulse through a plasma channel with an electron plasma density of 3×10^{17} cm^{-3} was maximized at the discharge time delay of around 150 ns and a discharge current of 400 A, resulting in a beam diameter of 36 μm (FWHM) at the capillary exit with a plasma. We observed the energy spectrum of the accelerated electrons with the most probable energy of 1.3 MeV. The accelerated electrons with energy around 1 MeV can be applied for novel diagnostics, such as x-ray sources, THz sources, ultrafast electron spectroscopy, materials processing, and injection source into accelerators.

Acknowledgements

The authors are deeply indebted to Dr. Kun Li, and Mr. Tsukasa Oshima for useful discussions and technical support. This work was supported by CREST (Core Research for Evolutional Science and Technology) of the Japan Science and Technology Agency (JST). A part of this work was performed under the auspices of MEXT (Ministry of Education, Culture, Science and Technology, Japan). We also are grateful to the Cooperative Research Center and the Venture Business Laboratory of Utsunomiya University for providing the laser system.

References

1) A. Butler, A. J. Gonsalves, C. M. McKenna, D. J. Spence, S. M. Hooker, S. Sebban, T. Mocek, I. Bettaibi, and B. Cros, "Demonstration of a Collisionally Excited Optical-Field-Ionization XUV Laser Driven in a Plasma Waveguide", Phys. Rev. Lett. **91**, 205001 (2003).
2) D. M. Gaudiosi, B. Reagan, T. Popmintchev, M. Grisham, M. Berrill, O. Cohen, B. C. Walker, M. M. Murnane, H. C. Kapteyn, and J. J. Rocca, "High-Order Harmonic Generation from Ions in a Capillary Discharge", Phys. Rev. Lett. **96**, 203001 (2006).
3) K. Nakajima, D. Fisher, T. Kawakubo, H. Nakanishi, A. Ogata, Y. Kato, Y. Kitagawa, R. Kodama, K. Mima, H. Shiraga, K. Suzuki, K. Yamakawa, T. Zhang, Y. Sakawa, T. Shoji, Y. Nishida, N. Yugami, M. Downer, and T. Tajima, "Observation of Ultrahigh Gradient Electron Acceleration by a Self-Modulated Intense Short Laser Pulse", Phys. Rev. Lett. **74**, 4428 (1995).
4) W. P. Leemans, B. Nagler, A. J. Gonsalves, Cs. Toth, K. Nakamura, C. G. R Geddes, E. Esarey, C. B. Schroeder, and S. M. Hooker, "GeV electron beams from a centimetre-scale accelerator", Nature Phys. **2**, 696 (2006).
5) A. Butler, D. J. Spence, and S. M. Hooker, "Guiding of High-Intensity Laser Pulses with a Hydrogen-Filled Capillary Discharge Waveguide", Phys. Rev. Lett. **89**, 185003 (2002).
6) A. J. Gonsalves, T. P. Rowlands-Rees, B. H. P. Broks, J. J. A. M. van der Mullen, and S. M. Hooker, "Transverse Interferometry of a Hydrogen-Filled Capillary Discharge Waveguide", Phys. Rev. Lett. **98**, 025002 (2007).
7) E. Esarey, P. Sprangle, J. Krall, and A. Ting, "Overview of Plasma-Based Accelerator Concepts", IEEE Trans. Plasma Sci. **24**, 252 (1996).
8) N. Yugami, T. Higashiguchi, H. Gao, S. Sakai, K. Takahashi, H. Ito, Y. Nishida, and T. Katsouleas, "Experimental Observation of Radiation from Cherenkov Wakes in a Magnetized Plasma", Phys. Rev. Lett. **89**, 065003 (2002).
9) D. Dorranian, M. Starodubtsev, H. Kawakami, H. Ito, N. Yugami, and Y. Nishida, "Radiation from high-intensity ultrashort-laser-pulse and gas-jet magnetized plasma interaction", Phys. Rev. E **68**, 026409 (2003).
10) E. Miura, K. Koyama, S. Kato, N. Saito, M. Adachi, and Y. Kawada, "Demonstration of quasi-monoenergetic electron-beam generation in laser-driven plasma acceleration", Appl. Phys. Lett. **86**, 251501 (2005).
11) C. G. Durffe, J. Lynch, and H. M. Milchberg, "Mode properties of a plasma waveguide for intense laser pulses", Opt. Lett. **19**, 1937 (1994).

HIGH ENERGY DENSITY SCIENCE BASED ON PULSE POWER TECHNOLOGY

Kazuhiko Horioka, Tohru Kwamura, Mitsuo Nakajima, Toru Sasaki, Kotaro Kondo
Department of Energy Sciences, Interdisciplinary Graduate School of Science and Engineering, Tokyo Institute of Technology, Nagatsuta 4259, Midori-ku Yokohama Japan 226-8502

Plasmas driven by pulse power devices and/or intense ion beams were evaluated, concerning researches on high-energy density and warm dense matter physics. A warm and dense plasma was produced using pulse power driven exploding discharges in water. A high temperature plasma was formed in a pulse power device by electro-magnetically driven strong shock wave. A quasi-statically tamped target has been proposed to make a well-defined, warm dense state for equation of state (EOS) studies based on ion beam heated target. A planning experiment for study on hydrogen EOS at warm dense condition is also shown.

INTRODUCTION

Properties of dense and/or high temperature plasma are of interests concerning the high energy density (HED) physics [1,2]. We are working on three research topics. The first one is a warm dense plasma made by exploding wire discharges in water, the second is a high temperature plasma induced by a strong shock wave, and the third is a target driven by intense heavy ion beam. Those plasmas can be driven by compact pulse power devices with laboratory scale and/or intense ion beams.

A warm dense (WD) state is produced by a wire explosion in water using a small, cylindrically arranged, pulse power generator. Electrical conductivities are directly estimated from the voltage-current characteristics of the wire explosion. Compared with previous research [3], we intended to make a semi-empirical approach to the exploding wire plasma; we would like to make a self-consistent scaling of equation of state (EOS) and transport coefficients from comparisons of numerical calculations and experimental observations of hydrodynamic behaviors of cylindrically evolving high density plasma. As the structure and the hydrodynamics of HED plasma are dominated by the EOS and the transport coefficient of them, we can discuss those values from comparisons of experimental observation and numerical simulation. In particular, we propose to use shock wave trajectories in water as a fitting parameter of the hydrodynamic behaviors.

The structure of strong shock waves in high-Z gas is expected to be completely different from that of conventional hydrodynamic shock waves, because relaxation processes, radiative processes and interplay between them in the shock heated region should affect the structure of shock wave itself [4].

A structured target is proposed for WDM study using ion beam heating method [5]. The hydrodynamics of the beam driven target is tamped by an outer gold layer of the target, which enables us to make a well defined, uniform test sample for the WDM study.

For the discussion of such a complicated hydrodynamics, the geometry should be as simple as possible. The exploding plasma in water is tamped and stabilized by the surrounding water and it makes an expanding plasma with cylindrical symmetry.

To make a well-defined, steady state, high temperature plasma, we designed a compact pulse power device, which has a pair of tapered electrodes and a cylindrical guiding tube.

The beam driven target has a cylindrical structure with a tamper layer. These configurations enable us to use one-dimensional assumption.

WIRE EXPLOSION IN WATER

In order to make warm dense plasmas, thin (50 μ m-100 μ m dia.) wires are exploded in a water-filled chamber. In the experiments, wire materials, their radius and the charge voltage are changed to make dense plasmas over a wide range of parameters.

Experimental Arrangement

Figure 1 shows a schematic diagram of the exploding wire discharges in water [6,7,8]. A capacitor bank C, consists of cylindrically arranged 8x0.4μF low inductance capacitors. The stray inductance Ls of the device was estimated to be Ls=105nH and it drove the wire explosion in water with time scale of μsec. The current and the voltage are measured with a Rogowski coil and a resistive voltage divider.

The evolutions of wire/plasma boundary and the shock wave are measured with fast streak/framing camera. From these measurements; i.e., the voltage, the current, and the plasma radius, we can directly estimate the electrical conductivities of exploding plasma.

Electrical Conductivity

Using the framing camera, the particle density was estimated to be typically 10^{21}cm^{-3} at 2μsec from start of the discharge. Figure 2 shows typical evolution of electrical conductivities of aluminum (Al), copper (Cu), and tungsten (W) wires.

The dotted lines in the figure show theoretical values for conductivities based on a modified Sptzer's model, and as can be seen, the experimental observations of the conductivities are more than 10times of the theoretical values.

We calculate the hydrodynamic behavior of exploding plasma and the shock wave propagation in water using a 1D magneto-hydrodynamic simulation. To make the calculation, we need EOS models and the transport coefficients. In other wards, we can discuss the accuracy of EOS and transport coefficients from the comparison of numerical calculation and experimental observation.

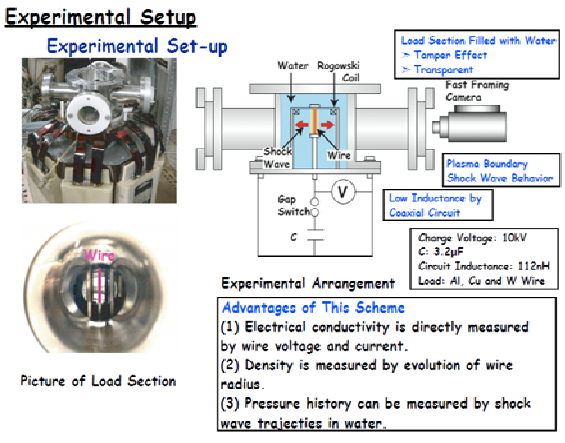

Fig.1 Experimental set-up and photograph of the device for exploding wire experiments

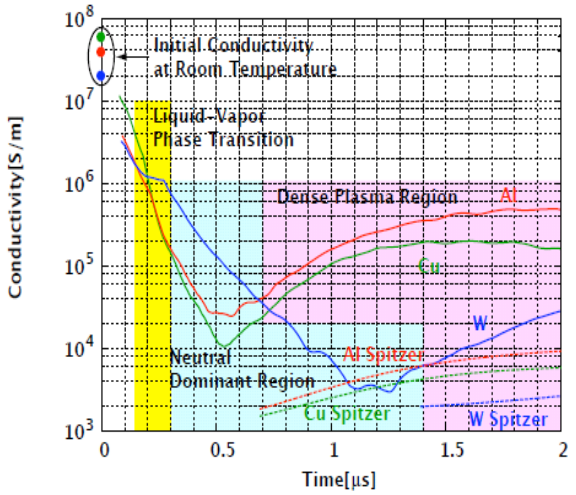

Fig.2 Evolution of conductivities for Al, Cu, and W wire explosion in water

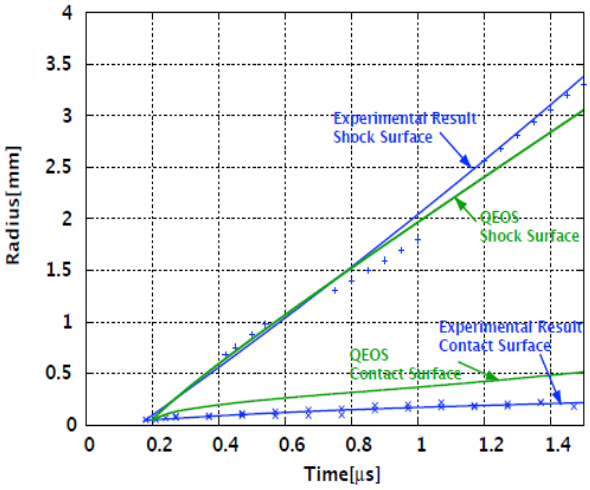

Fig.3 Experimental and numerical evolutions of wire/plasma boundary and shock surface in water

Figure 3 shows the comparisons of numerical and experimental evolution of the shock wave and the plasma boundary for Al wire explosion. Experimentally obtained conductivities and Q-EOS model [9] are used in this calculation.

As the hydrodynamics are strongly dependent on the EOS model, we can evaluate its applicability in the parameter region of WD plasma, by using it as a fitting parameter. In particular, the numerical shock trace is more strongly affected by that of plasma boundary; i.e., the EOS model. Symbols in Fig.3 show the experimentally observed plasma boundary and shock trajectory.

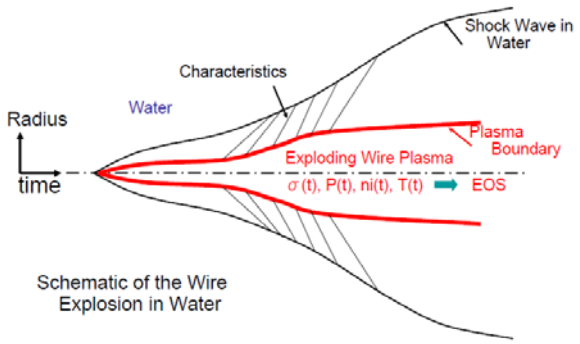

Fig.4 Schematic illustration of exploding wire discharges in water

Figure 4 shows a schematic illustration of the exploding wire evolution in water. As illustrated in Fig.4, The exploding wire/plasma induces a cylindrically developing shock wave, and the plasma boundary works as a piston. The shock trajectory is modified by the motion of the piston through the "characteristics" in water. The shock trace reflects the behavior of the plasma motion, both in space and time. This indicates that the shock wave trajectory in water is informative for estimation of the plasma pressure, i.e., for the EOS modeling.

FORMATION OF STRONG SHOCK WAVES WITH PULSE POWER DEVICE

Another compact pulse power device is constructed for generation of quasi-steady, one-dimensional, strong shock waves. The cross-section of the discharge region is gradually decreased with a pair of tapered electrodes. The shock wave induced by an electro-magnetically driven current sheet is guided through the tapered section to the top of electrodes. At the end of the electrodes, an acrylic guiding tube is attached to make one dimensional condition and optical measurements [11].

Experimental Arrangement

The experimental set up of the pulse power device for the strong shock experiments is shown in Fig.5. The acrylic guiding tube is advantageous to observe the shock wave propagation. The shock speed is measured by a fast framing/streak camera through the acrylic guiding tube. To drive the electro-magnetic pulse, twelve plastic capacitors are arranged in a cylindrical geometry. They are normally charged to 20kV and switched by a pressurized gap switch, which drove typically 160kA in the discharge chamber.

Experimtntal Results

Figure 6 shows typical experimental results. The solid line in the figure shows a criterion of radiative shock based on a steady state one dimensional flow [12,13]. As shown, the front velocity increased with the decrease of initial filling pressure of Xe. When

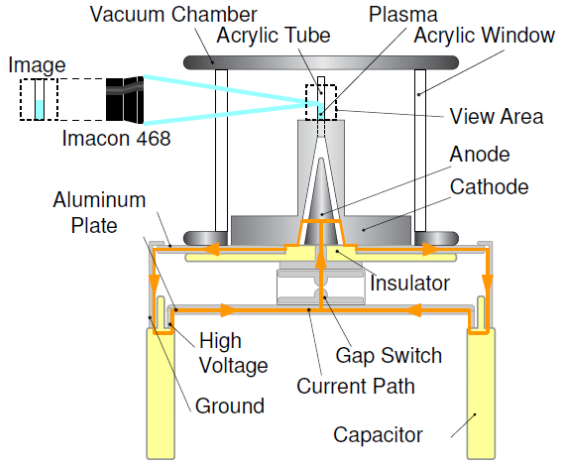

Fig.5 Experimental arrangement for shock heated high temperature hydrodynamics

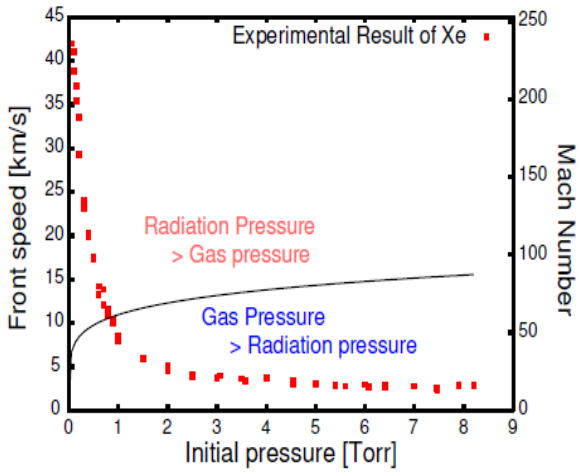

Fig.6 Observed front speed and shock Mach number versus initial filling pressure of Xe

the discharge chamber is filled with low pressure Xe gas, the shock Mach number M reached M=250, and, as shown in the figure, this value adequately exceeds the criterion for radiative shock waves.

When the front speed exceeds the criterion derived from the one dimensional simplified analysis, the streak image had an interesting structure [10].

The results indicate that structure of the shock heated region is dominated by the relaxation process including ionization relaxation in the Xe plasma and its initial condition should be provided by a radiative and/or thermal conduction process from the heated region. As our experimental configuration is one-dimensional, we can discuss these time-dependent process by the observation of plasma parameter as a function of distance from the shock front. This extremely simplify understanding of the intrinsically complicated phenomena and also means, from the comparison of experimental observation and numerical calculation, we can quantitatively discuss the effect of radiation transport on the hydrodynamics of heated gas with a strong shock wave.

BEAM DRIVEN TARGET FOR WDM SCIENCE

Beam Parameters

A schematic of the ion beam driven WDM study is shown in Fig.7. Here we consider All Ion Accelerator (AIA) based on the induction synchrotron for the beam driver [5,14]. Expected specification of the ion beam is also shown in the same figure. The beam is accelerated and bunched using the concept of induction synchrotron, to 100nsec in the final stage of the accelerator.

Behavior of beam irradiated target

The hydrodynamic behavior of the target has been calculated using a 2D hydrodynamic code, which includes the beam deposition process.

We propose a tamped and dumped target to make an uniform WDM test sample. The outer surface of an aluminum form target is coated with Au layer, which dumps the beam in the side Au layer and statically tamps the hydrodynamic motion of the Al form target. This configuration is expected to provide a quasi-statically tamped condition for the hydrodynamics of the beam heated target.

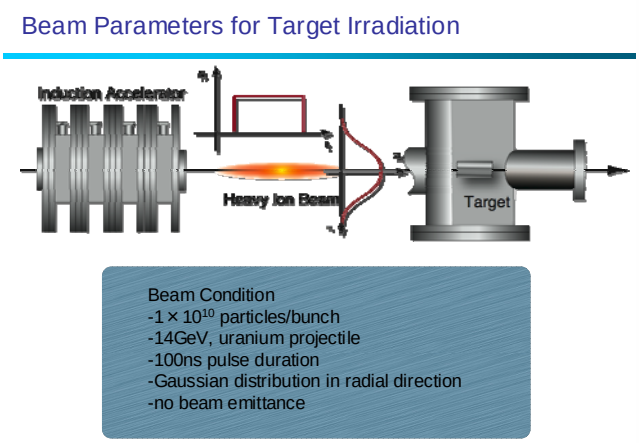

Fig.7 Schematic of the beam-driven target experiments

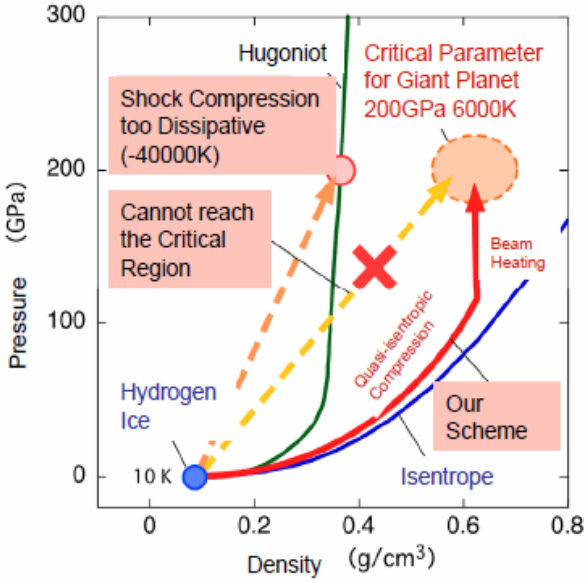

Fig.9 Expected compression trace of ion-beam heating assisted by pulse power pre-compression

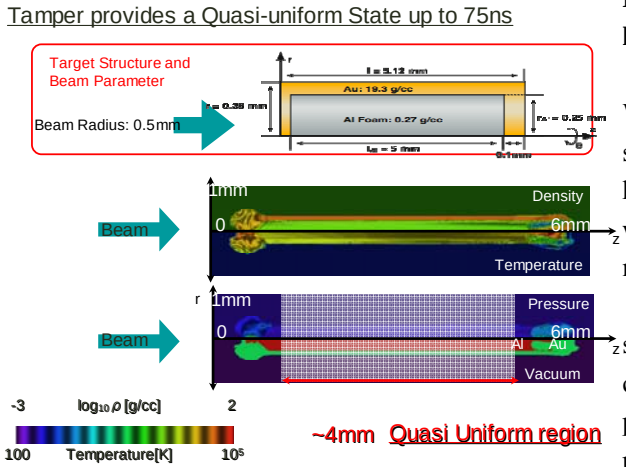

Fig.8 Behavior of dumped and tamped target for uniform WDM condition

The structure and an example of the behavior of beam irradiated target is shown in Fig.8. As shown in the figure, the density, the temperature, and the pressure of the beam heated target are uniform due to the tamper effect. As the side Au layer is practically not heated due to the beam dumping, the side Au layer works as a statically tamper. Then we can make a well defined target condition for WDM science.

We are planning to apply the ion-beam heating scheme for exploration of planetary science. As is known, accurate EOS derivation of hydrogen at a warm dense state is of critical importance for the modeling of giant planet.

In order to make the dense and high temperature state, shock wave compression has been conventionally used. However, the shock heating process is too dissipative to reach the critical parameter of hydrogen. Moreover, as EOS is implicitly included in the shock relation itself, the shock heating scheme is considered to be not advantageous for the hydrogen EOS study. By the volumetric heating of the ion-beam target, we can reach the critical condition; that is around 6000K and 200GPa, without effect of shock wave dissipation [15].

SUMMARY

Plasmas produced by compact pulse power devices are proposed for HED and/or WDM physics. Results show that plasmas made by wire explosion in water can be appropriate sources for scaling of the

equation of state and transport coefficients in a wide range of parameters of warm-dense materials. In the case of wire explosion, the coupling parameter of the plasma is estimated to be at least 2, up-to discharge time of 2 μ sec.

On the other hand, shock wave heated plasmas produced by pulse powered electro-magnetic force in a pair of conical electrodes, are demonstrated to be a suitable one-dimensional test sample for high temperature hydrodynamics involving ionization relaxation and a radiative energy transfer.

These devices can cover a dense moderate temperature region and a high temperature low density region in the density-temperature diagram for HED physics [1]. Advantages of these approaches are compactness, capability of making larger spatial and longer temporal scale plasmas, and also providing a well-defined condition, compared with those of high power laser methods.

Ion beam driven target also provides a good test sample for WDM study. A structured beam target was proposed to make a well defined condition for EOS study in warm dense region. Although intense ion beam is expensive to produce, the beam driven target is expected to cover a wide range of parameter region. In particular, the ion beam target is expected to be able to make critical WD condition of hydrogen for exploration of planetary science.

Although there are a lot of issues, new technologies and/or new field of science are expected to be realized by the new scheme of scientific tools.

ACKNOWLEDGEMENT

This work was partially supported by the Ministry of Education, Culture, Sports, Science and Technology, Grant-in-aid for Scientific Research Japan.

REFERENCES

[1] K.Horioka et. al., Nuclear Instruments and Methods, **A 577**, 298 (2007)

[2] *Frontiers in High Energy Density Physics-The X-Games of Contemporary Science*, Edited by R.Davidson et.al., National Academies Press, (2003)

[3] A.W.DeSilva and J.D.Katsourros, *Phys. Rev*., **E-57**, 5945 (1998)

[4] Y.B.Zel'dovich and Y.P.Raizer, *Physics of Shock Waves and High Temperature Hydrodynamic Phenomena*, Academic, New York, (1967)

[5] T.Sasaki, T.Kikuchi, M.Nakajima, T.Kawamura, K.Horioka, Nuclear Instruments Methods, Vol.577, 313 (2007)

[6] K.Horioka, M.Nakajika, T.Mizoguchi, T.Sasaki, *Proc. 15th High Power Particle Beams*, St-Petersberg, 7053 (2004)

[7] T.Sasaki, M.Nakajima, T.Kawamura, K.Horioka, *J. Plasma Fusion Res*., **Vol.81**, No.12, pp.965-966 (2005)

[8] T.Sasaki, Y.Tano, M.Nakajima, T.Kawamura, K.Horioka, Laser and Particle Beams, 24, 371 (2006)

[9] T.Sasaki, M.Nakajima, T.Kawamura, K.Horioka, This Proceedings, (2008)

[10] R.M.More, *Phys. Fluids*., **Vol.31**, 3059 (1988)

[11] K.Kondo, M.Nakajima, T.Kawamura, K.Horioka, *Review of Scientific Instruments*, **Vol.77**, 036104 (2006)

[12]K.Kondo, M.Nakajima, T.Kawamura, K.Horioka, Journal De Physique IV, Vol.133, 1051 (2006)

[13] S.Bouquet, R.Teussier and J.P.Chieze, *Astrophys. J., Suppl. Ser*., **Vol.127**, p.245 (2000)

[14] K.Takayama, et. al., Journal of Applied Physics, **101**, 063304 (2007)

[15] K.Horioka, et.al., Nuclear Instruments and Methods, (to be appear)

ELECTRICAL CONDUCTIVITY OF WARM DENSE TUNGSTEN

Toru Sasaki,[1] Mitsuo Nakajima,[2] Tohru Kawamura,[2] and Kazuhiko Horioka[2]

[1] *College of Science and Technology, Nihon University, Kanda Surugadai 1-8-14, Chiyoda-ku, Tokyo, 101-8308, Japan* *

[2] *Department of Energy Sciences, Tokyo Institute of Technology, Nagatsuta 4259, Midori-ku, Yokohama, 226-8502, Japan*

Electrical conductivity of warm dense tungsten was measured using an exploding wire discharge in water. Evolutions of the radius and the temperature were estimated together with the wire resistance. The conductivity was estimated based on the measurements and it was compared with conventional theoretical predictions. Results showed that the electrical conductivity is more than one order of magnitude lower than the conventional value and also indicated that the conductivity has a metal-insulator transition around $\rho \sim 0.03\rho_s$ at temperature of 5000K.

Keywords: warm dense matter, electrical conductivity, pulsed-power discharge, wire explosion

I. INTRODUCTION

Warm dense matter (WDM) physics, which is defined that the density goes from $10^{-3}\rho_s$ (ρ_s is the solid density of matter) to $10\rho_s$ and the temperature varies from 0.1 eV to 10 eV, has a potential of abundant scientific discovery for the properties of plasma at high densities and at moderate temperature, in which the Coulomb interaction energy between particles sometimes exceeds the thermal energy k_BT. We define Γ as the ion-ion coupling parameter

$$\Gamma = \frac{Z_{eff}^2 e^2}{4\pi\epsilon_0 a k_B T}, \tag{1}$$

where Z_{eff} is the effective ion charge, and $a = (4\pi n_i/3)^{-1/3}$ is the ion sphere radius. The interest in the WDM region arises because the atoms and/or ions in dense plasmas will start to behave to exhibit long- and short-range order of interactions due to the correlating effects of the atoms/ions. Also the plasmas at high density is composed of degenerated electrons, in which the thermal energy k_BT is often lower than the Fermi Energy $E_F = \hbar^2 \left(3\pi^2 n_e\right)^{2/3}/2m_e$. As the degeneracy parameter, we use

$$\theta = \frac{k_B T}{E_F} = \frac{2m_e k_B T}{\hbar^2 \left(3\pi^2 n_e\right)^{2/3}}, \tag{2}$$

where n_e is the electron density. These are index parameters how the WDM state is affected by both the coupled ions and the degenerated electrons. The WDM related problems include the formation of the giant planets and the hydrodynamics of fuel pellet of inertial confinement fusion [1–4].

*Electronic address: sasaki@phys.cst.nihon-u.ac.jp

Up to now, a number of theoretical approaches have been developed. They are quantum molecular dynamics (QMD) simulation [5–9] to evaluate electron correlation and statistical method [10–12] for estimation of ionization degree and degenerated plasma. We are also able to produce the warm dense state in laboratory by some experimental methods as the ultra short pulse laser, the heavy ion beam, and the pulsed-power discharges [5, 13–24]. We should experimentally evaluate the WDM state as a function of the thermodynamic parameters, namely density, temperature, internal energy, and pressure.

Tungsten has the highest melting temperature in metals, and its property at WD state is important to be understood not only for fundamental science but also for engineering field. For example, ablation process of the first wall and/or diverter material of magnetic fusion device largely rely on the property of warm dense tungsten.

In this paper, we focus on the electrical conductivity of tungsten in warm dense matter regime. We found that the conductivity has a minimum at the point in density about $0.03\rho_s$ and in temperature about 5000 K. The electrical conductivities are more than one order of magnitude lower than conventional conductivity scalings for tungsten.

II. EXPERIMENTAL SETUP

A schematic diagram of the experimental apparatus is shown in Fig. 1 [15, 20, 21]. Low inductance capacitors ($8 \times 0.4\mu$F) as a capacitor bank were cylindrically arranged to realize a fast wire explosion. To ensure a vaporization of wires, the capacitor bank was charged 10 kV, and it was switched by a low-inductance triggered spark gap. The evolutions of the current $I(t)$ and the voltage $V(t)$ were measured by a current monitor (PEASON: 110A) and a high voltage probe (Tektronix:

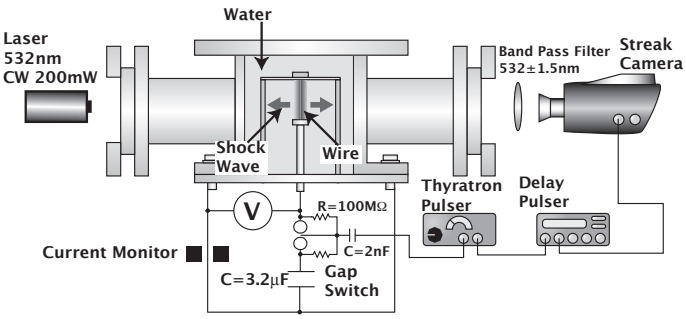

FIG. 1: Schematic diagram of the experimental apparatus.

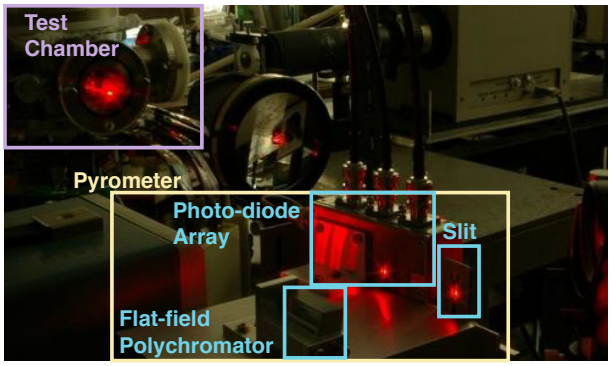

FIG. 2: Photograph of spectrometer which is composed of a polychrometor with a photo-diode array.

P6015A).

The experimentally obtained voltage was composed of resistive and inductive parts. The stray inductance L of the discharge device was estimated to be 105 nH from shunted waveforms of the current and the voltage. The evolution of wire/plasma resistance $R(t)$ is evaluated by the following equation;

$$R(t) = \frac{V(t) - LdI(t)/dt}{I(t)}, \tag{3}$$

and the evolution of input energy $E(t)$ is also estimated from the basic electrical measurements using,

$$E(t) = \int_0^t \left(V(t) - LdI(t)/dt\right) I(t) dt. \tag{4}$$

The load material of a tungsten wire has high degree of purity 99.9 %. The diameter of load material (50 - 100 μm) is less than the skin depth, which realizes uniform heating and enables us to evaluate the electrical conductivity and input energy.

For insulation of the electrode gap and tamping the wire/plasma, we filled the test chamber with water. As the wire/plasma resistance need to be much lower than the water resistance, we estimated effective resistivity of the water. From the unloaded circuit, the water resistance is estimated to be 12kΩ. This result means, the reliable wire/plasma resistance is evaluated up to order of few kΩ.

The hydrodynamic behaviors of wire/plasma radius and the shock wave in water were measured by a shadowgraph method using a fast streak camera with a laser (λ_L = 532 nm). From the time evolution of radius, we can evaluate a wire/plasma density and conductivity with the voltage and the current measurements. The wire/plasma is assumed to be homogeneous because the expansion wave in the wire/plasma transit with order of a few tens of nanoseconds. Therefore, we can measure the density and the temperature of wire/plasma by these device directly. From this assumption, the density $\rho(t)$ of the wire/plasma is obtained from

$$\rho(t) = \rho_s \left(\frac{r_0}{r_p(t)}\right)^2, \tag{5}$$

where $r_p(t)$ is the wire/plasma radius, and r_0 is the initial wire radius.

The conductivity $\sigma(t)$ is evaluated using the wire/plasma radius $r_p(t)$ and the evolution of the resistance $R(t)$ from the current and the voltage reduced by the inductive correction LdI/dt as

$$\sigma(t) = \frac{l}{\pi r_p^2(t) R(t)}, \tag{6}$$

where l is the wire/plasma length.

Broad spectra of wire/plasma emission were observed by a fast framing camera with a grating monocrometer [21]. The wire/plasma is estimated to be in a local thermodynamic equilibrium (LTE) state during the observation time. Under aforementioned assumption, we assembled a spectrometer which is composed of a polychrometor with a photo-diode (HAMAMATSU: S5971) array for the measurement of evolution of wire/plasma temperature. The wire/plasma emission in LTE obeys the Planck's formula as

$$I(\lambda, T)\, d\lambda = \frac{2hc^2}{\lambda} \frac{1}{e^{hc/k_B T\lambda} - 1} d\lambda, \tag{7}$$

where λ is the wavelength, T is the wire/plasma temperature, c is the speed of light, h is the Planck constant, and k_B is the Boltzmann constant. The polychrometor signals, which were calibrated by a xenon lamp (HAMAMATSU: L7810), detects the emission at 458 nm, 558 nm, and 658 nm.

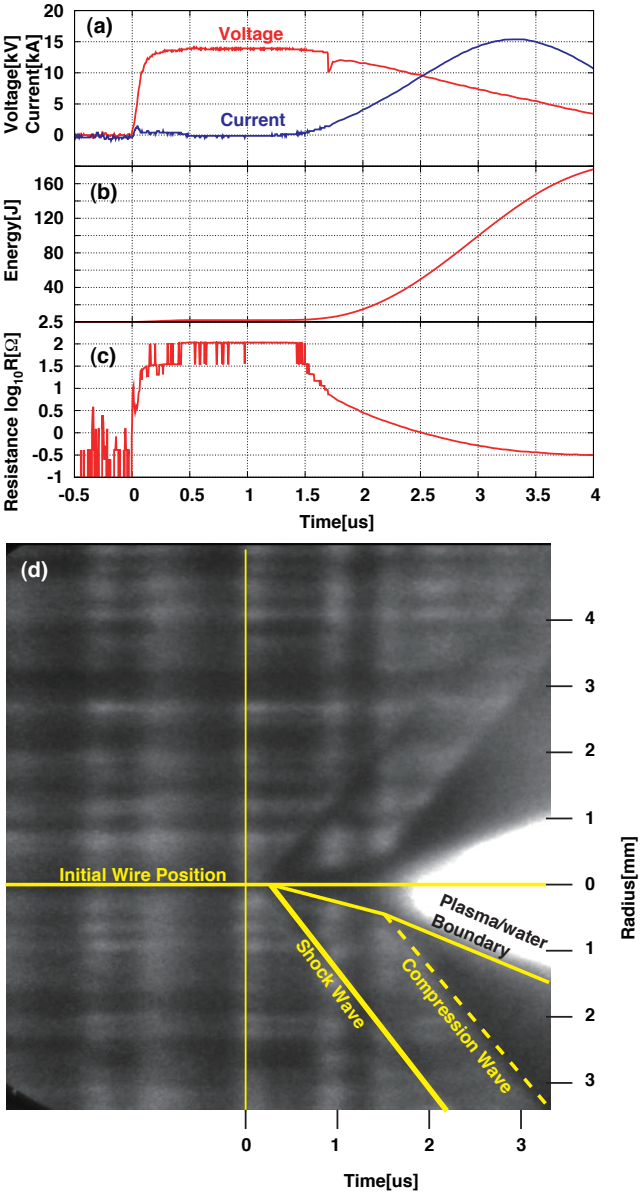

FIG. 3: Typical evolution of (a) waveforms of voltage and current, (b) input energy, (c) resistance, (d) hydrodynamic behavior of exploding wire/plasma in water, for tungsten wire discharges with 50 μm in diameter and 24.5 mm in length.

III. RESULTS AND DISCUSSIONS

Figure 3 shows typical evolutions of waveforms of voltage and current, input energy, resistance, and hydrodynamic behavior of tungsten wire with 50 μm in diameter and 24.5 mm in length. The observed waveforms, input energy, and hydrodynamic behavior in Fig. 3 can be divided three discharge phase. First phase; the required energy for evaporation is provided until 0.5 μs from the beginning of discharge. Second phase; the input energy become plateau from 0.5 μs to 1.7 μs from the beginning of discharge. Final phase; the input energy rapidly increase from 1.7μs from the beginning of discharge.

In the first phase, we can see the wire/plasma surface does not move in Fig 3 (d). Estimating the input energy (Fig. 3 (b)) from the waveforms in Fig. 3 (a) indicates that the wire/plasma was ensured the vaporization energy, which is about 5 J for tungsten wire having 24.5 mm in length and 50 μm in diameter. The resistance of the wire/plasma rapidly increased from order of 0.1 Ω to 100 Ω.

After the evaporation, that is the second phase, the energy input to wire ceased for a while, because of the arrival of rarefaction wave at the radial direction, which cool down the plasma. Furthermore, the plasma density can be decreased through the propagation of rarefaction (sound) wave; in our experimental condition, the sound wave in the plasma propagates within a few tens nanoseconds. We can see in Fig. 3 (d) the vaporization and the starting of hydrodynamic motion of wire/plasma accompanied by a shock wave in water.

In the final phase, we can see the current waveform increased again, thereby enhances the input energy. At the same time, the streak image of the wire explosion revealed the dark region which shows the propagation of 'characteristics' in water. It indicated that the hydrodynamic behavior was affected by the input energy history. Additionally, from the streak images, we can see that the shock surface and the plasma boundary behaviors are cylindrically symmetric during the observation time.

Figure 4 shows the time evolution of density, temperature, electrical conductivity, coupling parameter, and inverted degeneracy parameter of wire/plasma in water of tungsten wire discharge with 50 μm in diameter and 24.5 mm in length. The density of wire/plasma, which is obtained by eq. (5) with the wire/water surface in Fig 3 (d), is estimated to decrease to 0.001ρ_s at 3 μs from the beginning of discharge. The evolution of density is correspondent to the input energy history. The evolution of wire/plasma temperature in Fig. 3 (b) also relies on the input energy history. The temperature was estimated to increase up to 20000 K at 3 μs from the beginning of discharge. These density and temperature are ensured the WDM state up to 3 μs.

Until 0.5 μs from the beginning of discharge, the electrical conductivity in Fig. 4 (c) rapidly decreased because the wire/plasma became the active lattice valuation's at the solid and the liquid phase. After the vaporization from 0.5 μs to 1.5 μs, we can see the electrical conductivity also decreased up to 10^3 S/m caused by a few free and/or conductive electrons at the dense vapor phase. After the minimum conductivity at 1.5 μs, the wire/plasma sent up due to changing from a gas phase

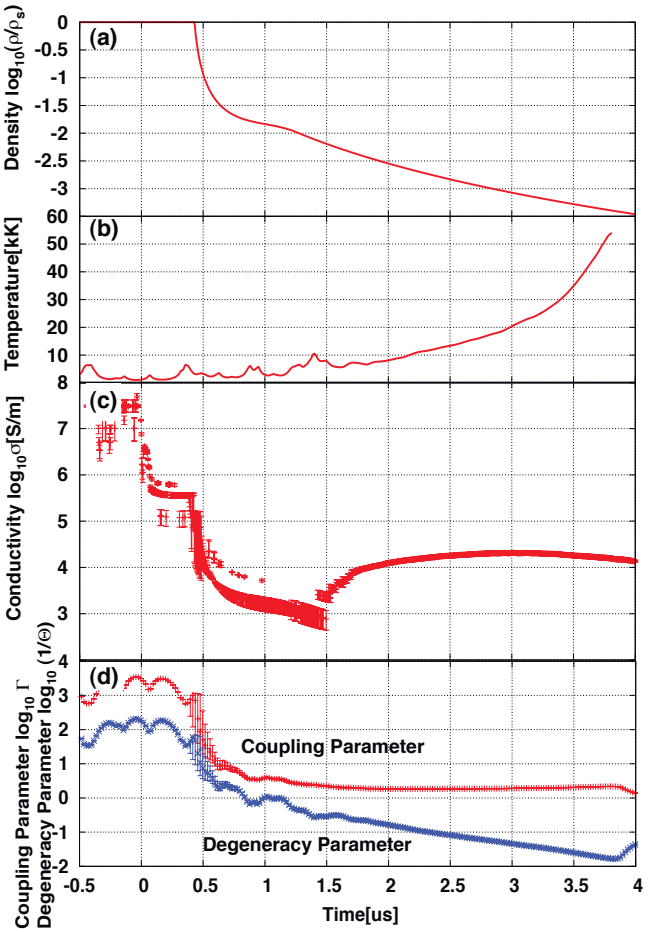

FIG. 4: Typical evolution of (a) density, (b) temperature evaluated from pyrometer, (c) conductivity, and (d) coupling parameter and inverted degeneracy parameter of wire/plasma of tungsten discharges in water with 50 μm in diameter and 24.5 mm in length.

to a plasma state. After a few microseconds from the beginning of discharge, the wire/plasma is heated rapidly at this phase, and the electrical conductivity increases from 10^3 S/m to 10^4 S/m.

We evaluate the ion-ion coupling parameter Γ and the electron degeneracy parameter θ in Fig. 4 (d). In these evaluations, the electron density is not directly estimated because the exploding wire/plasma became the black body. The electron density is assumed to follow a prediction based on the Thomas-Fermi averaged ionization model which neglects the shell structure [25]. As shown in Fig. 4 (d), the coupling parameters of the exploding plasma are estimated to be $\log_{10}\Gamma \sim 0$, that is, Γ is around 1, at the observation time. It indicates that the plasma evolves a strongly coupling state in the observation time. The degeneracy parameter monotonically decreased as a function of time. Around 2 μs, the degeneracy parameter is estimated to be $\theta \sim 0.1$, which shows the system of electrons as being in a non-degenerate, classical state [26]. The comparison of the electrical conductivity and the degeneracy parameter indicated that the transition of electrical transport processes changes around 1.5 μs from the beginning of discharge.

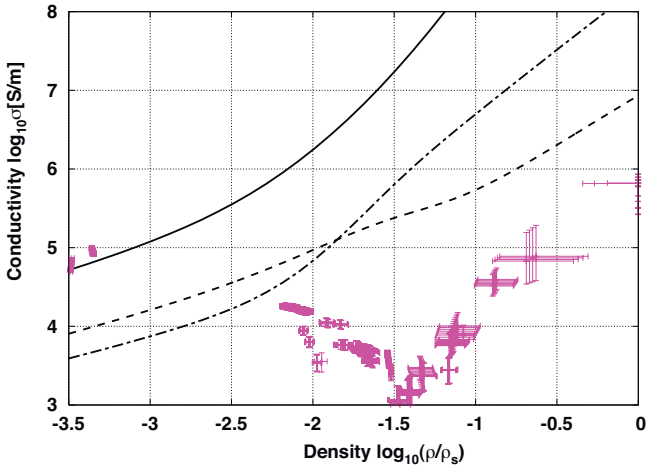

FIG. 5: Electrical conductivity of tungsten as a function of density at 5000 ±10 %. The solid line indicates the Spitzer conductivity model , the dashed line reveals the Ichimaru conductivity model, and the dash dotted line denotes the Lee-More conductivity model .

Figure 5 shows the electrical conductivity of tungsten wire as a function of density at temperature of 5000 K ± 10 %. Theoretical conductivities based on the models of Spitzer, Lee-More, and Ichimaru at 5000 K are also shown in Fig. 5. The electron density of these theoretical models are also evaluated by the Thomas-Fermi model [25]. These results cover a wide density range for a material, from a liquid metal having highly degenerated electrons to a plasma that approaches to ideal plasma conditions. As shown in Fig. 5 , the Spitzer's theory is clearly inappropriate in the WDM regime. The comparison also exhibits that the conductivity models of Lee-More and Ichimaru are in good agreement in the region of $\log_{10}(\rho/\rho_s) < -2$.

The tungsten conductivity clearly show an inflection point around $\log_{10}(\rho/\rho_s) \sim -1.5$ as can be seen in Fig. 5. At the high density regime of $\log_{10}(\rho/\rho_s) > -1.5$, the electrical conductivity is considered to be affected by the lattice vibration and the stretched lattice distance. At the low density regime of $\log_{10}(\rho/\rho_s) < -1.5$, the electrical conductivity is considered to increase by enhancing the electron density. It indicates that the electrical conductivity has the inflection point around the density of $\log_{10}(\rho/\rho_s) \sim -1.5$, that is $\rho \sim 0.03\rho_s$, at temperature of 5000 K.

IV. CONCLUSIONS

We investigated the conductivity for tungsten to study the physics of matter in warm dense region. The conductivities were evaluated from basic electrical measurements together with a streak camera and a spectroscopic method. The results indicated that the tungsten makes the metal-nonmetal transition around $\log_{10}(\rho/\rho_s) = -1.5$ at temperature of 5000 K. We compared the experimentally obtained electrical conductivity in a warm dense state to theoretical models. Although, the qualitative behavior of conductivities is similar, the experimentally observed conductivities were more than one order of magnitude lower than the theoretical values. These results indicate that more detailed analyses are needed at dense low temperature region.

We are planning to evaluate both the relaxation time and the effective ionization degree based on optical conductance measurements together with the Drude fomula. In addition, we are also going to evaluate the state of matter based on 'semi-empirical' scaling based on the experimental observation and the numerical calculation.

[1] R. C. Davidson, ed., *Frontiers in High Eneregy Density Physics* (NATIONAL ACADEMIES, 2003).

[2] S. Atzeni and J. Meyer-ter-Vehn, *The Physics of Inertial Fusion: Beam Plasma Interaction, Hydrodynamics, Hot Dense Matter* (Oxford University Press, USA, 2004).

[3] S. Ichimaru, H. Iyetomi, and S. Tanaka, Physics Reports **149**, 91 (1987).

[4] J. Lindl, Physics of Plasma **2**, 3933 (1995).

[5] P. Renaudin, C. Blancard, G. Faussurier, and P. Noiret, Physical Review Letters **88**, 215001 (2002).

[6] J. Clerouin, P. Renaudin, Y. Laudernet, P. Noiret, and M. P. Desjarlais, Physical Review B **71**, 064203 (2005).

[7] M. W. C. Dharma-wardana, Physical Review E **73**, 036401 (2006).

[8] S. Mazevet, M. P. Desjarlais, L. A. Collins, J. D. Kress, and N. H. Magee, Physical Review E **71**, 016409 (2005).

[9] D. O. Gericke, M. S. Murillo, and M. Schlanges, Physical Review E **65**, 036418 (2002).

[10] M. P. Desjarlais, Contributions to Plasma Physics **41**, 267 (2001).

[11] D.-K. Kim and I. Kim, Physical Review E **68**, 056410 (2003).

[12] S. Kuhlbrodt, B. Holst, and R. Redmer, Contributions to Plasma Physics **45**, 73 (2005).

[13] I. Krisch and H. J. Kunze, Physical Review E **58**, 6557 (1998).

[14] S. Saleem, J. Haun, and H. J. Kunze, Physical Review E **64**, 056403 (2001).

[15] T. Sasaki, M. Nakajima, T. Kawamura, and K. Horioka, Journal of Plasma Fusion Research **81**, 965 (2005).

[16] H. Yoneda, H. Morikami, K. Ueda, and R. M. More, Physical Review Letters **91**, 075004 (2003).

[17] A. W. DeSilva and J. D. Katsouros, Physical Review E **57**, 5945 (1997).

[18] S. H. Glenzer, G. Gregori, F. J. Rogers, D. H. Froula, S. W. Pollaine, R. S. Wallace, and O. L. Landen, Physics of Plasmas **10**, 2433 (2003).

[19] S. H. Glenzer, O. L. Landen, P. Neumayer, R. W. Lee, K. Widmann, S. W. Pollaine, and R. J. Wallace, Physical Review Letters **98**, 065002 (2007).

[20] T. Sasaki, Y. Yano, M. Nakajima, T. Kawamura, and K. Horioka, Laser and Particle Beams **24**, 371 (2006).

[21] T. Sasaki, Y. Yano, M. Nakajima, T. Kawamura, and K. Horioka, Journal of Physics: Conference Series **112**, 042026 (2008).

[22] A. Grinenko, D. O. Gericke, S. H. Glenzer, and J. Vorberger, Phys. Rev. Lett. p. 194801 (2008).

[23] T. Sasaki, T. Kikuchi, M. Nakajima, T. Kawamra, and K. Horioka, Journal of Physics: Conference Series **112**, 042027 (2008).

[24] N. A. Tahir, D. H. H. Hoffmann, A. Kozyreva, A. Tauschwitz, A. Shutov, J. A. Maruhn, P. Spiller, U. Neuner, J. Jacoby, M. Roth, et al., Physical Review E **63**, 016402 (2001).

[25] R. M. More, *Atomic Physics in Inretial Confinement Fusion Part I & Part II* (UCRL-84991, 1981).

[26] S. Ichimaru, *Statistical Plasma Physics II: Condensed Plasmas* (Westview Press, 2004).

STUDY ON TARGET STRUCTURE FOR DIRECT-INDIRECT HYBRID IMPLOSION IN HEAVY ION INERTIAL CONFINEMANT FUSION

Y. Iizuka[1], T. Kikuchi[1], S. Kawata[1] and A.I. Ogoyski[2]

[1]*Utsunomiya University, Utsunomiya, Japan*
[2]*Technical University of Varna, Varna, Bulgaria*

ABSTRACT

In order to realize an effective implosion, beam illumination non-uniformity on a fuel target must be suppressed less than a few %. In this study a direct-indirect hybrid implosion mode is discussed in heavy ion beam inertial confinement fusion (HIF) in order to release sufficient fusion energy in a robust manner. In the direct-indirect hybrid mode target, a low density foam layer is inserted, and the radiation energy is confined in the foam layer. In the foam layer the radiation transport is expected to smooth the HIB illumination non-uniformity in the lateral direction. In this study, we study the influences of the foam thickness and the inner Al density on the implosion uniformity. Two-dimensional fluid simulations demonstrate that the hybrid target contributes to the HIB non-uniformity smoothing and releases a sufficient fusion energy output in HIF.

I. Introduction

In inertial confinement fusion (ICF) driven by heavy ion beams (HIBs), the following critically important issues intensively studied: ion source, accelerator physics for high current beam, beam bunching, HIB transport in a reactor, HIB target interaction, stopping power, high-energy density matter physics, and so on.[1)-8)] There are two implosion schemes for ICF, that is, direct-[3),5)] and indirect-driven designs. Each design has some advantages and disadvantages. The direct-driven scheme has a simple structure of the fuel pellet, although the scheme may be sensitive for the illumination non-uniformity of HIBs. On the other hand, the indirect-driven scheme may be robust against the illumination non-uniformity with the lower number of the HIBs. However, the fuel pellet structure is complicated.

In ICF driven by HIBs, after impinging of the HIB particles onto the fuel target, the pusher layer is ablated by the thermal expansion due to the HIB deposition energy. Then the pusher layer pushes the DT fuel to the central direction. The DT fuel us compressed and must achieve a high-density high-temperature state after the void close. During the DT compression, the ablation front must be uniform to realized an effective implosion, and a fuel burning. However, the limited-HIB-number illumination may induce the non-uniform ablation front and the non-uniform target implosion in the realistic cases. In this study, a direct-indirect hybrid mode is proposed and discussed in ICF driven by HIBs, in order to release sufficient fusion output energy in a robust manner. In order to calculate a fuel target implosion more realistically, we couple a hydrodynamics code with a HIB illumination code[9)], and analyze the target implosion.

The target energy gain required for energy production in ICF can be evaluated by considering a reactor energy balance as shown in Fig. 1. The driver pulses deliver an energy E_d to the target, which releases a fusion energy E_{fus}. The energy gain is $G = E_{fus} / E_d$. The fusion energy is first converted into thermal energy at a blanket in a reactor chamber and then converted into electricity by a standard thermal cycle with an efficiency η_{th}. A fraction f of the electric energy is recirculated to a driver system, which converts it into beam energy with an efficiency η_d. The energy balance for this cycle can be written $f\eta_d\eta_{th}G = 1$. Taking $\eta_{th} = 40\%$ and requiring that the recirculated fraction of electrical energy be smaller than 1/4, we find the condition $G\eta_{th} > 10$. For a driver efficiency in the range of $\eta_d = 10 - 33\%$, the condition leads to a target gain of $G = 30 - 100$ required for power production. Especially, the required fusion gain is about 30 for HIB ICF (HIF), because the HIB driver efficiency is about $\eta_d = 30\%$.

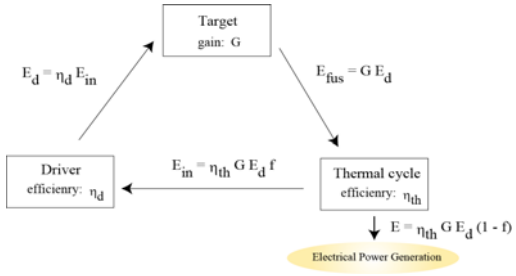

Figure 1 Energy balance in a HIF reactor system

Ⅱ. Direct-indirect hybrid mode

In order to study the non-uniformity smoothing effect by the radiation transport effect on a pellet implosion, the target hydrodynamics code is coupled with the HIB illumination code.[9] Figure 2 (a) shows the fuel target without foam layer. The confined radiation energy may smooth the HIB illumination non-uniformity. Therefore, we employ a foam layer to increase the confined radiation energy at the low density region (see Fig.2 (b)). We call this target a direct-indirect hybrid target in this paper. The outer Pb layer thickness is 0.03mm and the outer Al layer thickness is 0.47mm. The Pb mass density is 11.3 g/cm^3. The Al mass density is 2.69 g/cm^3. The mass density of the foam layer is 0.01% of the Al solid density. The external radius is 4.0mm.

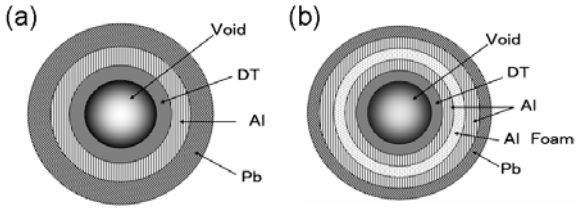

Figure 2 HIF fuel targets (a) without the foam layer, (b) with the foam layer.

The HIB pulse consist of a foot pulse and a main pulse as shown in the Fig.3. In this case, we employ Pb^+ ion HIBs with the mean particle energy of 8GeV. We employ the 32-HIBs illumination system.[10)-12)] The total energy is 4.0MJ. The beam particle density distribution is in the Gaussian. The longitudinal temperature of HIB ions is 100 MeV with the Maxwell distribution.

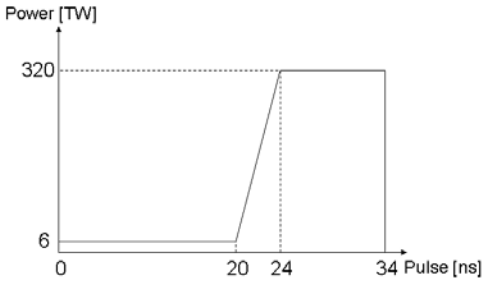

Figure 3 The HIB pulse consist of the low power part (foot pulse) and the high power one (main pulse).

We evaluate the beam illumination non-uniformity at the target. In HIF the Bragg peak deposition area plays the most important role for a target implosion. Therefore, we employ the total relative root-mean-square (RMS) as follows:

$$\sigma = \sum_{i=1}^{N_1} w_i \sigma_i$$

$$\sigma_i = \frac{1}{\langle F_i \rangle} \sqrt{\frac{1}{N_i} \sum_{j=1}^{N_i} \left(F_{ij} - \langle F_{ij} \rangle\right)^2}$$

$$w_i = \frac{\sum_{i-1}^{N_i} F_{i,j}}{\sum_{i-1}^{N_1} \sum_{j=1}^{N_j} F_{i,j}}$$

Here, σ is the implosion non-uniformity and σ_i is the non-uniformity on the i-th. w_i is the weight function. $F_{i,j}$ is the physical quantity (radiation temperature, ion temperature, density and pressure) in each mesh. $\langle F_{ij} \rangle$ is the mean physical quantity. N is the total mesh number. In our study, the physical model employed is based on a three-temperature (an ion, an electron and a radiation temperatures) fluid model. In calculations of the implosion, the equation of state is evaluated by using a fitting formula of the SESAME Library[13] based on the Thomas-Fermi model.

In this section, we employ the 32-HIBs illumination system.[10)-12)] To see the radiation transport effect on the implosion non-uniformity smoothing, we compare the results for the case with the radiation transport (ON) and without the radiation transport (OFF) for the target shown in Fig.1 (a). Figure 4 presents the time dependence of the RMS non-uniformity of the radiation temperature at the ablation front in the case of the radiation transport ON and OFF. In Fig.4 we see that the implosion non-uniformity at the ablation front becomes small

effectively by the main pulse in the case of the radiation transport ON. During the main pulse, the implosion non-uniformity can be smoothed by the radiation transport effect.

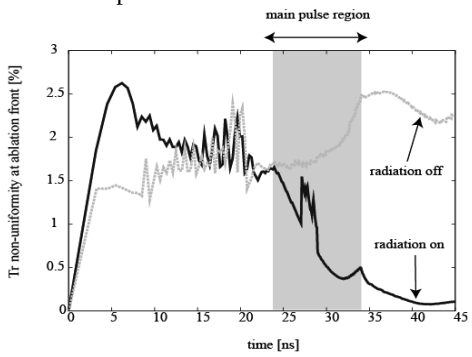

Figure 4 The histories of the RMS non-uniformity of the radiation temperature at the ablation front in the case of the radiation transport ON and OFF.

Figure 5 presents the time dependence of the confined radiation energy at the low density region. The peak conversion efficiencies of the HIB total energy ton the radiation energy are ~4.5% in the case of the 0.5mm foam and ~1.5% in the case without the foam. From these results, we find that the implosion mode in the case with the foam may be a hybrid of direct driven and indirect driven modes.

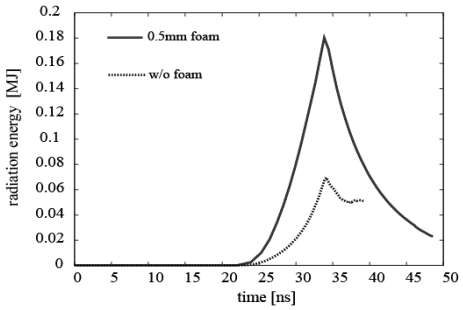

Figure 5 Time dependence of the confined radiation energy at the low density region in the case of 0.5mm foam and without the foam.

Ⅲ. Effect of foam thickness

In the foam layer the radiation is expected to smooth the HIB illumination non-uniformity in the lateral direction. In this section, we use the direct-indirect hybrid target (see Fig. 2 (b)). In order to study the influence of the foam thickness on the implosion, the foam thickness is changed between 0.6mm to 1.0mm. The Al foam density is 0.01% of the solid density. Figure 6 shows the gain versus the foam thickness. Figure 6 presents that there is the optimum foam thickness.

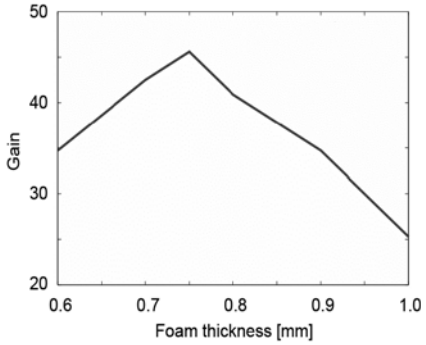

Figure 6 The pellet gain vs the foam thickness

Figure 7 (a) shows the radiation temperature non-uniformity and the ion temperature non-uniformity in the Al layer versus the foam thickness at the void closure time. Figure 7 (b) shows the implosion efficiency versus the foam thickness. Figures 7 (a) and (b) show that the implosion non-uniformity and the implosion efficiency decrease with the increase in the foam thickness. When the foam thickness becomes too thick, a sufficient implosion pressure can not be obtained. Therefore, the pellet gain becomes small in the case of the thick foam.

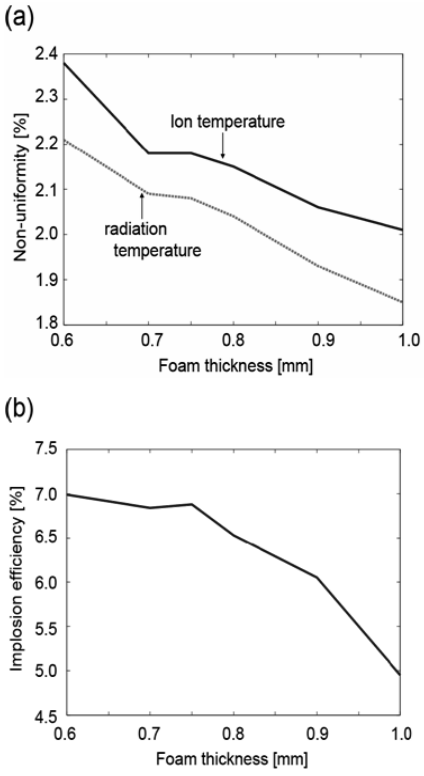

Figure 7. The foam thickness versus (a) the radiation temperature non-uniformity and the ion temperature non-uniformity at the void closure time and (b) the implosion efficiency.

Ⅳ. Effect of inner Al density

This section presents the effect of the inner Al density on the hybrid target implosion. In Fig. 8 the target consists of five layers of a solid Pb, a solid Al, a foam Al, an inner Al and DT. In order to study the inner Al density influence on the implosion, the inner Al density varies in four cases as shown in Fig. 8.

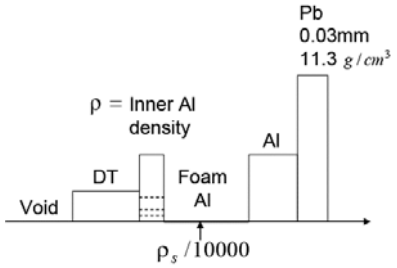

Figure 8 The target structure.

The inner Al density varies among 2.69 g/cm^3 ($\rho = \rho_s$ (solid density)), 10% of the Al solid density ($\rho = \rho_s/10$), 1% of the Al solid density ($\rho = \rho_s/100$) and 0.1% of the Al solid density ($\rho = \rho_s/1000$). The inner Al has the roles of the DT fuel pusher and the prevention of the fuel pre-heating. The foam Al density is 0.01% of the solid density. We also employ the 32-HIBs illumination system.[10)-12)] Figure 9 shows the gain versus the foam thickness for the various inner Al densities ρ . Figure 9 shows that there is the optimum density for the inner Al layer and the target is robust against the change in the foam Al thickness.

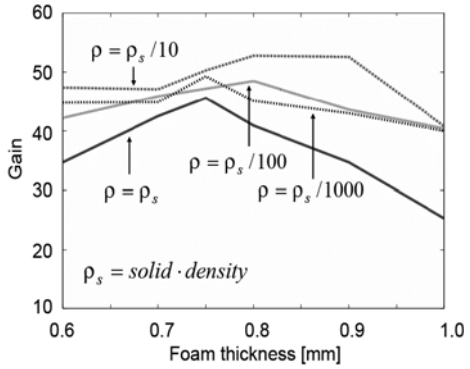

Figure 9 The pellet gain versus the foam thickness for the various inner Al densities ρ .

In the case of $\rho = \rho_s/10$ a high gain is obtained and the target is robust against the change in the foam Al thickness. Figures 10 show the non-uniformities in the Al layer versus the foam thickness at the void closure time: (a) the pressure non-uniformity and (b) the density non-uniformity. The inner Al density has influence on the implosion non-uniformity. When the inner Al density becomes lower, the implosion non-uniformity decreases.

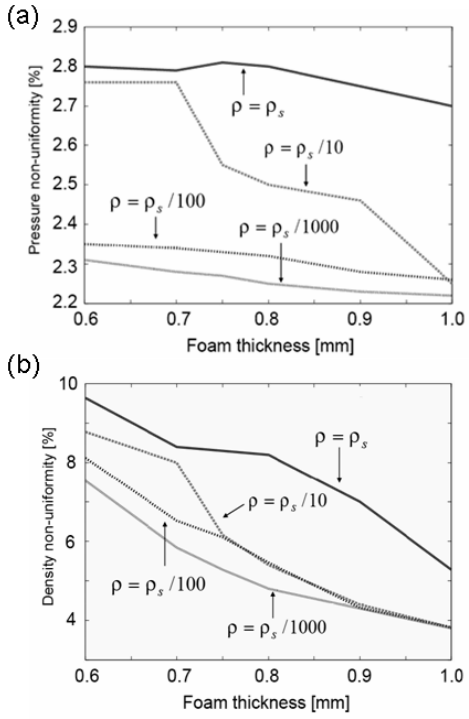

Figure 10 The non-uniformities in the Al layer at the void closure time: (a) the pressure non-uniformity and (b) the density non-uniformity for the various inner Al densities ρ .

Figure 11 shows the isentrope parameter α at the void closure time: $\alpha = p(\rho_{DT}, T)/p_{\deg}(\rho_{DT})$, where $p_{\deg}(\rho_{DT}) = A_{\deg}\rho_{DT}^{5/3}$, ρ_{DT} is the average DT density and $A_{\deg} = 2.17 \times 10^{12} (erg/g)/(g/cm^3)^{2/3}$. In ICF, α should be kept small as possible.[14)] In Fig. 11, when the inner Al density is kept high, ($\rho = \rho_s$ or d $\rho = \rho_s/10$), α is kept small successfully. However, when the inner Al density becomes lower ($\rho = \rho_s/100$ or $\rho = \rho_s/1000$), the pre-heating effect becomes significant (see Fig. 11) and the pellet gain becomes low compared with that for

$\rho = \rho_s / 10$ as shown in Fig. 9. These results indicate that the inner Al density is an important parameter to obtain a sufficient fusion energy output.

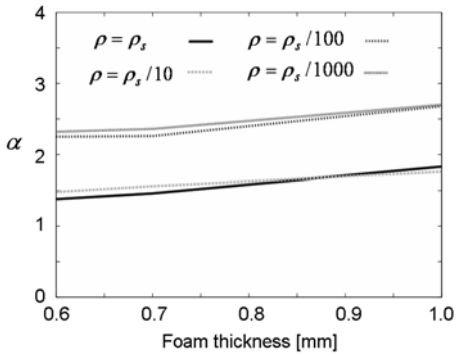

Figure 11 The pellet gain versus the foam thickness for the various inner Al densities ρ .

Ⅴ. Conclusions

In this paper, we discussed the target implosion non-uniformity smoothing in a direct-indirect hybrid target by using a low density foam layer. The direct driven fuel target implosion was weak against the beam non-uniformity. However, in the low density foam region, the radiation energy is confined and then the implosion non-uniformity is smoothed. Therefore, we employ the foam layer for the fuel target in order to realize a uniform implosion. We studied the influences of the foam thickness and the inner Al density on the implosion in the direct-indirect hybrid target. From our calculation results, the change in the foam thickness has an influence on the implosion. When the foam thickness becomes thick, the implosion non-uniformity decreases. However, the implosion efficiency is not sufficient for the thick foam. Therefore there is the optimum foam thickness on the implosion. The foam thickness is the important parameter to release the sufficient fusion energy. We also study the effect of the inner Al density on the implosion. In our calculation results, when the inner Al density becomes lower, the implosion non-uniformity decreases. However, in this case of the lower foam inner Al density the fuel pre-heating cannot be prevented. Therefore, the inner Al density is the important parameter to obtain a sufficient fusion energy output. Our results present that in HIF the direct-indirect hybrid implosion mode is realized by employing the foam layer in the spherical target.

Acknowledgments

This work was partly supported by the JSPS (Japan Society for the Promotion of Science) and MEXT (Ministry of Education, Culture, Sports, Science and Technology). We would also like to present our thanks to colleagues in the Japan and US HIF VNL research group for their fruitful discussions on this subject.

References

1) J. D. Lindl, R. W. Mcrory, and M. Campbell, Phys. Today **45,** 32 (1992).
2) W. J. Hogan, R. Bangerter, and G.L. Kulcinski, Phys. Today **45,** 42 (1992).
3) M. Tabak and D. Callahan-Miller, Phys. Plasmas **5,** 1895 (1998).
4) M. Tabak and D. Callahan-Miller, Nucl. Instrum. Methods in Phys. Res A. **415,** 7 (1998).
5) D. A. Callahan, Appl. Phys. Lett. **67,** L3254 (1995).
6) T. Someya, S. Kawata, T. Nakamura, A. I. Ogoyki, K. Shimizu, and J. Sasaki, Fusion Science and Tech. **43**, 282 (2003).
7) W. M. Sharp, D. A. Callahan, M. Tabak, S. S. Yu, et al., Fusion Science and Tech. **43**, 393 (2003).
8) J. Sasaki, T. Nakamura, Y. Uchida, T. Someya, et al., Jpn. J. Appl. Phys. **40,** L968 (2001).
9) A. I. Ogoyki, T. Someya and S. Kawata, Comp. Phys. Comm. **157**, 160 (2004).
10) T. Someya, S. Kawata, T. Kikuchi, A. I. Ogoyski, Nucl. Instrum. Methods, Phys. Res. A **544**, 406 (2005).
11) A. I. ogoyski, T. Someya, T. Sasaki, S. Kawata, Phys. Lett. A **315**, 372 (2003).
12) T. Someya, A. I. Ogoyski, S. Kawata, T. Sasaki, Phys. Rev. ST Accel. Beam **7**, 04470 (2004).
13) A. R. Bell, Rutherford Lab. Report. RL-80-091 (1981).
14) S. Atzeni, J. Meyer-ter-vehn, *the physics of inertial fusion* (Clarendon Press, Oxford, 2004), p. 52.

DEBRIS FORMATION IN A Z-PINCH DISCHARGE

Keiichi Takasugi and Akiko Maeda[+]
Institute of Quantum Science, Nihon University, Tokyo 101-8308, Japan
[+]*College of Science and Technology, Nihon University, Tokyo 101-8308, Japan*

The measurements on the debris were conducted in a z-pinch discharge with tin electrode. Many of the debris come flying from interelectrode. The debris is a collection of melted tin particles with 1–100 μm in size. It was confirmed that the debris is scattered nonuniformly with the collapse of the pinch.

1 Introduction

Gas-puff z-pinch is an efficient system for energy conversion [3], and high temperature and high density plasma is achieved easily. The system has been used as soft x-ray and EUV light source. As the z-pinch is a high current discharge with electrodes, the electrode material disperses and adheres to the chamber wall, the viewing windows, and the diagnostic instruments. Mitigation of the dispersing material (debris) is the most important subject in the development of EUV light source for the next generation semiconductor lithography[1, 2].

In a past research, a cloud structure of x-ray radiograph has been observed around the hot spots in z-pinch plasma[3]. X-ray spectroscopy showed that K_α line of the metal was emitted from the structure. It has been thought that the structure is made of the neutral atoms, which were originated from the electrode[4]. We think that the cloud structure is the debris. The purpose of this research is to clarify the generation mechanism of the debris, and to understand its behavior.

Measurement of the source of the debris was made by using a pinhole at first. Next the debris was observed by a scanning electron microscope (SEM), and the material was analyzed by an energy dispersive x-ray spectroscopy (EDX). Then the dynamic behavior of the debris was observed by using glass plates.

2 Experimental Setup

The experiment was conducted on the SHOTGUN z-pinch device at Nihon University (Fig. 1). The energy storage section of the device consists of 30 kV 24 μF capacitor bank, and the maximum discharge current is 300 kA. Charged voltage of the bank was 25 kV (7.5 kJ) in this experiment. The isolated gas distribution can be formed between the electrodes by a high-speed gas valve and an annular Laval nozzle mounted on the anode. The anode was made of graphite. The cathode was made of stainless steel, and several tin sheets were attached on the surface of it. The distance between the electrodes was 3 cm. Argon gas was used in this experiment, and the plenum pressure of the gas valve was 5 atm.

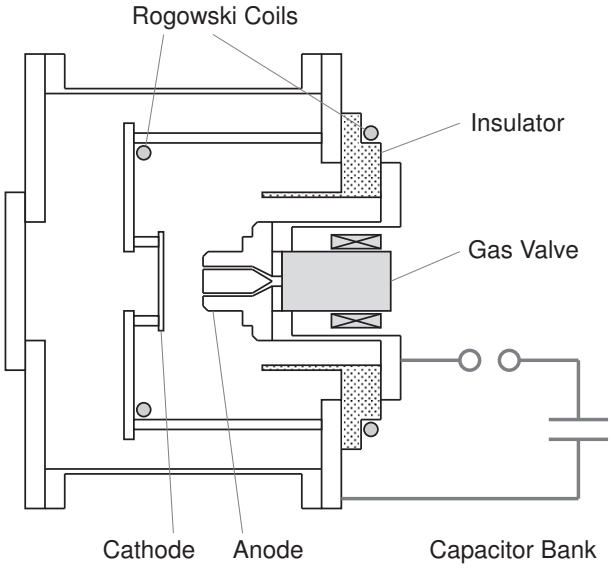

Fig. 1: Schematic diagram of the SHOTGUN z-pinch device.

Figure 2 shows the schematic arrangement of the pinhole camera for the observation of debris source. The debris emitted by the electrical discharge piles up on the film by passing through the pinhole. The pinhole image shows

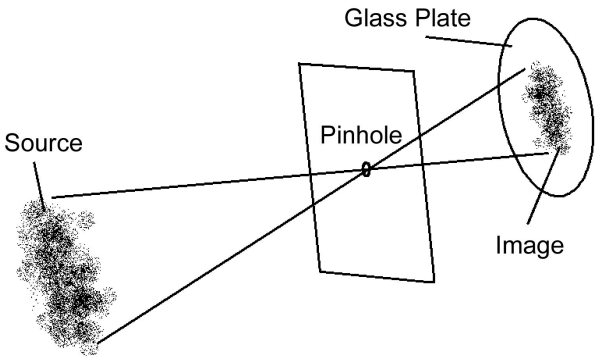

Fig. 2: Schematic arrangement of the pinhole camera for the observation of debris source.

spatial distribution of the source of the debris, if it flies straight. The distance between the device center and the pinhole was 212 mm, and the distance between the pinhole and the film was 50 mm. A glass plate was used for collecting the debris, and the amount of the debris was evaluated by the darkness of the image. The diameter of the pinhole was 3 mm.

3 Size of The Debris Source

The pinhole camera was exposed over 40 shots of discharges. Figure 3 is the debris collected by the glass plate. The debris has extended dimly. The extension is about 10 mm on the glass plate from the density trace of the debris. The size of the debris source is estimated to be about 30 mm from the size and the location of the pinhole, if the debris comes straight from the center of the device. The size just corresponds to the interelectrode distance. Therefore, it can be thought that the observed debris has mainly dispersed from the interelectrode.

4 Observation Using SEM

The debris has been collected in the device by an aluminum sample stand of 15 mm in the diameter. Figure 4 is the sample stand after 150 shots of discharges. The color of the stand was changed from the color of aluminum to something like yellow or purple, and the change in the color was not the same.

The surface of the sample stand was observed with the SEM (HITACHI S-2150). Figure 5 is the secondary electron image of the sample stand. The scales shown in the photographs are (a) 400 μm and (b) 40 μm, respectively. Melted lumps of metal like droplets of solder on the desk were found everywhere in the view. The sizes of the lumps were asunder from about 1 to 100 μm. This observation shows that the debris particles dispersed while melting. The surface roughness indicates that the big particle was hardened on the small particles.

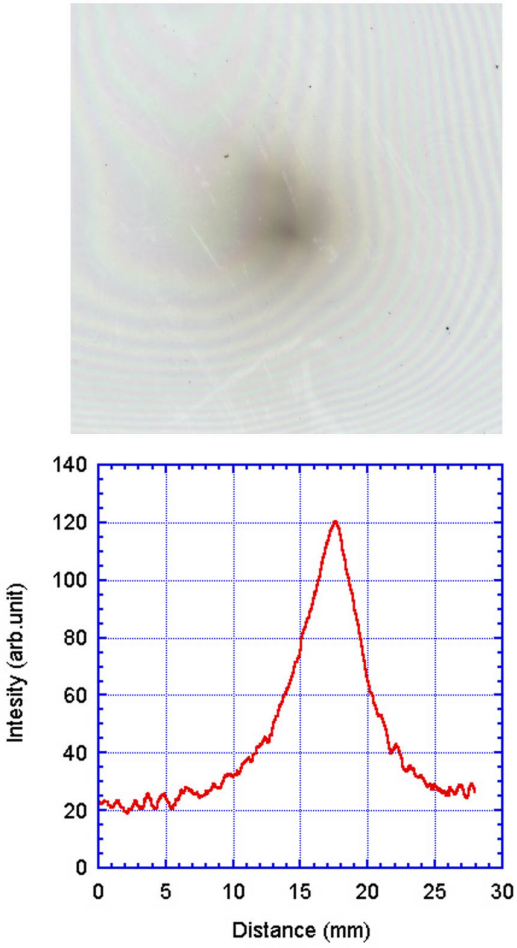

Fig. 3: Collected debris on the glass plate and its density trace. The extension is about 10 mm on the glass plate.

The square region shown in Fig. 5(b) was analyzed with the EDX (HORIBA EMAX7000). Figure 6 shows the energy spectrum and the analysis result of obtained x-rays. A horizontal axis shows the x-ray energy and the vertical axis shows strength of x-rays. It has been understood that the element in the region was almost tin (Sn), and iron (Fe) and carbon (C) were slightly contained.

In concluding the observations, it has been understood that the tin electrode was melted, and the droplets of metal dispersed and adhered to the surrounding objects.

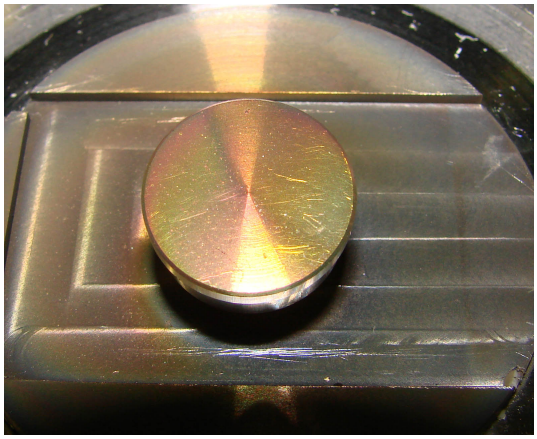

Fig. 4: The debris collected by the aluminum SEM stand. The surface color was changed to yellow or purple.

5 Observation with Glass Plates

In order to examine the appearance of the debris around the electrodes, glass plates were put in the device. The size of each glass plate was 26×76 mm. The plates were set up on eight return rods that fixed the cathode (Fig. 7). The rods were numbered from 1 to 8 counterclockwise toward the anode.

After 30 shots of discharges, the appearance of the debris collected by the glass plates is shown in Fig. 8. The number of the glass plate corresponds to the number of the rod of Figure 7. The debris of the plate 1 adhered thoroughly. There was a lot of debris of the plate 2 on the side of the plate 1. The debris of the plates 3 and 7 was comparatively little. It was attached to the whole of the plate 4, and it has been biased to the anode side for the plate 5. It was attached to spots in the plates 6 and 8.

The debris was sure to adhere to eight glass plates almost uniform, if it dispersed from the source in the straight line. This result shows that the direction where the debris dispersed was not uniform, and that there was a space structure. The structure seems to have m=2 dependence in the azimuthal direction. Therefore, it is thought that the motion of the plasma was related to the dispersion of the debris, and that it was scattered on surroundings with the collapse of the plasma.

Moreover, the debris slightly adhered from the other side of the glass plate to the whole like being remarkable in the plates 3 and 7 where the debris was few. This debris has come from

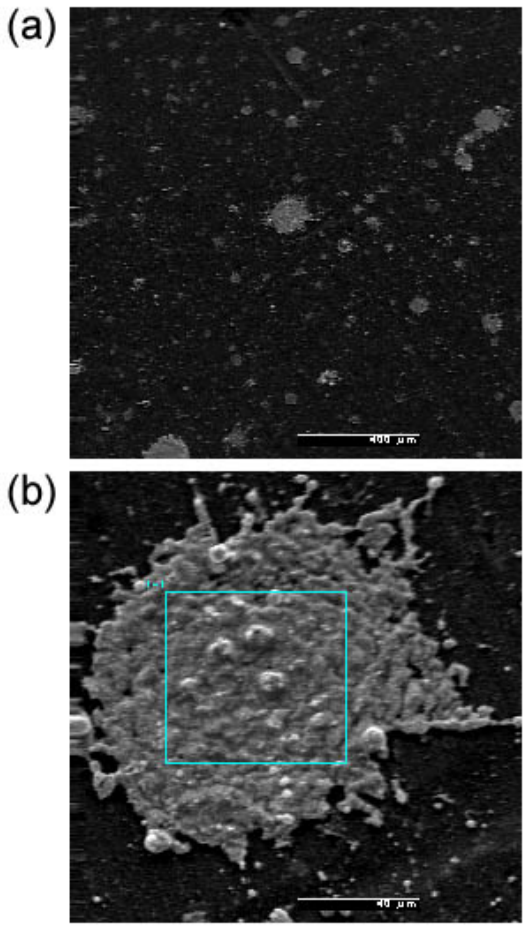

Fig. 5: Debris particles observed using the SEM. The scales shown in the photographs are (a) 400 μm and (b) 40 μm.

the chamber wall, and it was thought to be generated by the collision of the collapsing plasma with the wall.

6 Summary and Discussion

The experiment of understanding the generation of the debris was conducted in the z-pinch discharge with tin electrode. It was confirmed by the measurement of the pinhole camera that the size of the main source of the debris was about 30 mm. That is, the main source was neither the surface of the electrode, nor the chamber wall, and interelectrode. It has been understood from the observation with SEM that the debris was made up of tin particles of 1–100 μm in size, and that they dispersed while melting. It has been understood from the observation using glass plates located near the electrodes that the dispersion of the debris was not uniform, and that it was influenced by the motion

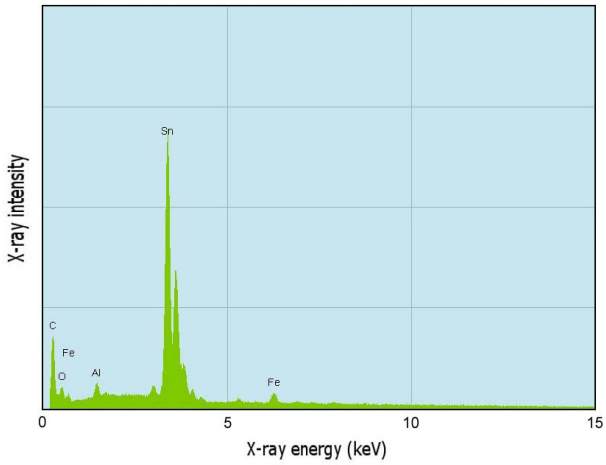

Fig. 6: Analysis of the square region of Fig. 5(b) using the EDX. The element was almost tin (Sn).

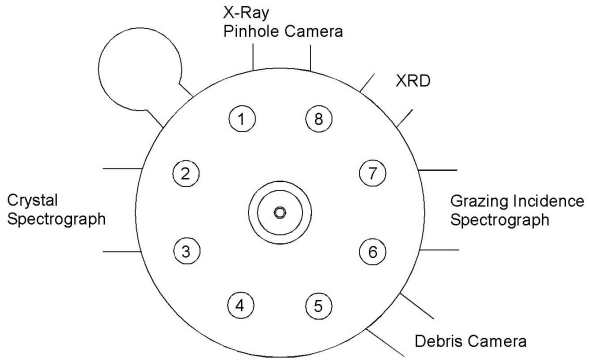

Fig. 7: Location of glass plates for the measurement of the debris distribution. They were numbered from 1 to 8.

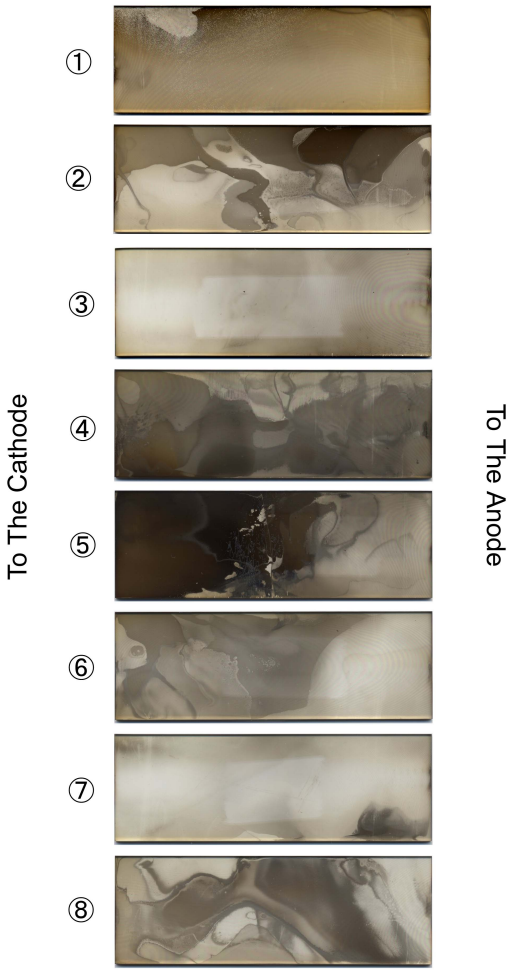

Fig. 8: Spatial distribution of debris collected by the glass plates.

of the plasma.

The droplets of debris particles are imagined to be charged in the contact with the plasma. If the particles are charged, it is possible for them to be influenced by the electromagnetic field around the plasma and to move with it. It can be understood for the debris to disperse nonuniformly to the surroundings, when the plasma collapses due to the instability. Moreover, it has been understood that a slight amount of debris comes flying from the chamber wall.

References

[1] E.V. López, B.E. Jurczyk, M.A. Jaworski, M.J. Neumann and D.N. Ruzic, Microelectronic Engineering **77**, 95 (2005).

[2] S. Fujioka, H. Nishimura, K. Nishihara, M. Murakami, Y-G Kang, Q. Gu, K. Nagai, T. Norimatsu, N. Miyanaga, Y. Izawa, K. Mima, Y. Shimada, A. Sunahara, and H. Furukawa, Appl. Phys. Lett. **87**, 241503 (2005).

[3] K. Takasugi, A. Takeuchi, H. Takada and T. Miyamoto, Jpn. J. Appl. Phys. **31**, 1874 (1992).

[4] K. Takasugi, S. Narisawa and H. Akiyama, AIP Conf. Proc. **651**, 131 (2002).

DENSE PLASMA FOCUS DEVICE FOR HYDROGEN-BORON FUEL FUSION

H.R.Yousefi, Z.P.Wang, Y.Nishino, H.Ito, K.Masugata

Department of Electric and Electronic System Engineering, University of Toyama, Toyama 930–8555, Japan

ABSTRACT

We will use hydrogen-boron fuel (p-^{11}B) instead of usual fuel D-D and D-T in dense plasma system, like plasma focus device. Hydrogen-boron fuel requires high ion energies or temperatures for fusion reactions. Significant burn only starts at one billion degrees or 100keV and the highest rate of burn is at 600keV.Recent result indicate that we can reach to this temperate by plasma focus device.

Fusion energy is one of a number of clean energy options including solar, wind, and geothermal. However, controlled fusion has a unique property. It operates with plasma – the fourth state of matter. Most of the universe, including our Sun, consists of plasma (ionized gas). To date many billions of dollars have been spent on fusion power development in the world. Plasma physics has now evolved into a mature science. In 1968 we were a factor of 100,000 short of the conditions necessary to achieve break even with the easiest fuel cycle (deuterium/tritium – DT).This goal has now been achieved. The $15 billion International Thermonuclear Experimental Reactor (ITER) is being constructed in France to reach conditions for net power generation using DT fuel. Deuterium-tritium (D-T), which produce most of their energy in the form of neutrons, require a standard thermal cycle, in which the neutrons are used to boil water, and the resulting steam drives a large turbine and generator. Thus, fusion with D-T fuels could not significantly reduce the capital costs of electric power generation even if the fusion reactor that produces the neutrons were cost-free. Energy waste and radioactive waste can be avoided by choosing a better fuel.Aneutronic fusion is any form of fusion power that produces 98% of their energy in the form of charged particles instead of neutrons. This means that energy could be converted directly into electricity by various techniques. Successful aneutronic fusion would greatly reduce problems associated with neutron radiation such as ionizing damage, neutron activation, and requirements for biological shielding, remote handling, and safety issues. Recent results indicate that among of all candidate aneutronic reactions, hydrogen-boron (p–^{11}B) is most favorable. Hydrogen-boron fuel requires high ion energies or temperatures for fusion reactions. Significant burn only starts at one billion degrees or 100keV and the highest rate of burn is at 600keV.this can be achieved in plasma "hot spots" or plasmoids.Recently Sandia National Laboratories reported [1] an ion temperature T_i of over 200 keV (2×10^9 degrees), by Z-pinch machine and also Texas A&M University reported an ion energy over 100keV with peak current 1.4 MA in a dense plasma focus device. The p-^{11}B reaction produces only helium, hence radioactivity is eliminated as a primary design factor; and fusion has no possibility of a "nuclear runaway." The boron fusion fuel supply is abundant and ubiquitous.

Many electrical generation techniques can be used with a boron fusion system. Since boron fusion releases its energy as charged particles, the possibility of direct energy conversion to electricity at 80-90% efficiency exists. This development would effectively remove the thermal pollution problem experienced by existing power plants. Since the energy can be released as electromagnetic waves portable fuel and chemical production are options. It also opens the

possibility for space travel propulsion, which is currently being researched.

However, there are serious obstacles to a Z-Pinch being used as a practical fusion reactor. For one thing, the giga-gauss fields needed for generating practical amounts of fusion energy are not achievable with the Z-Pinch unless it can be used to form plasmoids. Second, the Z-Pinch destroys the electrodes with each shot, so rapid pulsed operation is precluded.Therfore; it seems that just dense plasma focus has this capability to reach to this high magnetic field and temperature in the hot spots or plasmoids and it's also repeatable.

However, we should emphasis that in the p–^{11}B reaction, bremsstrahlung radiation is a major channel of energy loss. The problem of bremsstrahlung emission is amplified in our case because of the high temperatures achieved by the p-^{11}B dense plasma focus (DPF) pinch (~ MeV), and the radiation's Z^2 dependence. The above two major challenge must be overcome to achieve the goal, therefore our plan is base on the obtaining ion energies well above 100keV and minimizing losses by bremsstrahlung x-ray. In very high magnetic fields, on the order of a megatesla, a quantum mechanical effect is theorised to suppress the transfer of energy from the ions to the electrons. According to one calculation, the bremsstrahlung losses could be reduced to half the fusion power or less.

For this goal we are planning to simulate the plasmoid formation in dense plasma focus to investigate that what condition is optimal to achieve the require temperature, magnetic field and density for this fusion.

References

[1] M. G. Haines, P. D. LePell, C. A. Coverdale, B. Jones, C. Deeney, and J. P. Apruzese, PHYSICAL REVIEW LETTERS **96,** 075003 (2006)

FABRICATION AND CHARACTERIZATION OF SILICON CARBIDE USING ELECTRON BEAM BY PLASMA FOCUS DEVICE

Z.P. Wang*, H.R. Yousefi, Y. Nishino, H. Ito, K. Masugata

Department of Electric and Electronic system Engineering, University of Toyama, 3190 Gofuku, Toyama 930-8555, Japan

ABSTRACT

Silicon carbide (SiC) was synthesized by a 20 kJ Mather-type dense plasma focus device. The preparation method and characterization data are described for SiC grown on the silicon (100) substrate. X-ray diffractometer (XRD), Fourier Transform Infrared Spectroscopy (FTIR), Field-Emission Scanning Electron Microscopy (FE-SEM) and Nano-indentor were employed for the characterization of three samples at different axial positions of 50mm, 90mm and 130mm, respectively. Polycrystalline 3C－SiC were found at the position of 90mm and 130mm by the study of the XRD and FTIR spectra. Porous structure on the silicon carbide surface at the position of 90mm has been found by SEM analyses. Nano-indentor indicates the mechanical hardness at the position of 130mm is higher than that at the position of 90mm.

I. Introduction:

SiC is a promising material for Si substitution in microelectronics industry, especially in high-power, highfrequency and high-temperature devices due to its wide band gap and high breakdown field [1]. Compare with Si (operating temperature ≤ 250℃), the properties of SiC's makes it an excellent material for devices operating at high temperatures(600℃ and higher) [2]. Moreover, it has been demonstrated that both surface and bulk leakage in SiC devices can be reduced to much lower levels that could ever be achieved by silicon [3].The energy gap of silicon is relatively narrow, which means that either injection or generation of minority carriers leads to observable leakage current of any silicon-based switch biased in off mode. Therefore, it is silicon carbide that emerges as a unique semiconductor with electronically passivated surface and a wide energy gap, enabling low-leakage switches that cannot be achieved in silicon. There are many technical challenges, but perhaps the most obvious one is the very high annealing temperatures needed to achieve selective doping by ion implantation. Because of this, the demonstrated MOSFETs on SiC are not self-aligned (the gate electrode is deposited after the doping and has to be aligned to the source/drain region). This is not a suitable

structure for complex integrated circuits. Instead of full competition with silicon technology, there is an alternative option for SiC development: integration of SiC devices on silicon wafers [4]. In recent years, several methods have been developed to synthesize SiC micro and nano-structures, including chemical vapour depositions, ion beam assisted deposition, gas source molecular beam epitaxy using hydrocarbon gases such as acetylene, ethylene and dymethylgermane, supersonic jets of Si(CH3)4 and Si3H8, ion beam mixing and ion implantation [5–9]. The formation of a SiC layer in the conventional methods takes place via carbonization reaction between supplied gases and Si atoms which proceeds onto the surface of a Si substrate. In this case the Si atoms diffuse and reach the top of the SiC growth surface from the substrate. The diffusion of Si atoms from the substrate results in defect formation at the Si–SiC interface [7]. To overcome the defect formation by the diffusion of Si atoms, the use of energetic carbon ion irradiation is thought to be effective for carbonization reaction [10].

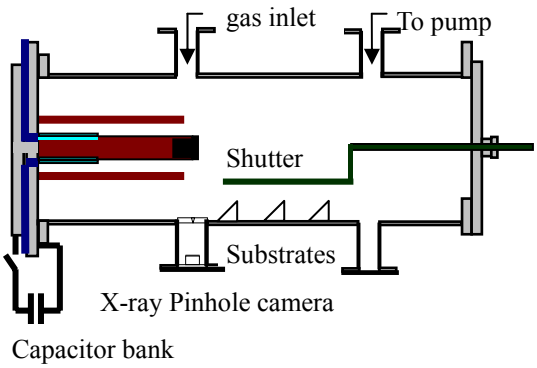

Fig. 1 Schematic experimental arrangement of PF system for SiC film deposition

The dense plasma focus (DPF) is well known as a compact and an efficient pulsed source of x -rays [12], neutrons [11], relativistic electrons and energetic ion beams [12, 13]. Plasma focus, when used as a pulsed plasma device for thin film deposition, has some special features with respect to other methods that include high deposition rate, energetic deposition process which assist the film formation and possible film deposition under a reactive background gas pressure. The current sheath dynamics in plasma focus allows the formation of high temperature(1 — 2keV) and high-density(~10^{25}—10^{26} m^{-3}) plasma column at the end of radial collapse phase [14]. The plasma column then disintegrated due to plasma instabilities, which generate energetic ions and relativistic electrons. The plasma jet and energetic electrons are responsible for the ablation of the anode material and the ablated material is deposited on the substrate. Recently, the plasma focus device has been used successfully for the deposition of various thin films [15–20]. In the present work, we report the deposition of SiC films on Si (100) substrate under the appropriate conditions by ablation of the graphite target and silicon substrate with the help of pulse electron beam using multiple shots of the DPF device. In this case, energetic carbon ions penetrate directly into the Si subsurface to form SiC layers by direct carbonization reaction without requiring Si atom diffusion. Structural, Optical, morphological and mechanical properties of deposited films are characterized by X-ray diffractometer (XRD), Fourier Transform Infrared Spectroscopy (FTIR), Field-Emission Scanning Electron Microscopy (FE-SEM) and indentation hardness tester.

II. Experimental Procedure

Experiments were performed on a 20kJ, Mather-type DPF device. The arrangement of the experiment set-up is shown schematically in Fig.1. The plasma focus (PF) device basically consists of a squirrel cage electrode assembly kept inside a vacuum chamber, a capacitor bank with spark gap switch and high voltage charger. The PF device is powered by a capacitor bank of 44.8 μF, 30 kV. At 30 kV operating voltage the capacitor bank delivers a maximum current of 600 kA with 1.7 μs quarter period. A rogowski coil and biased ion collectors are used to measure the current density and ion energy respectively.

Commercially available one sided mirror like polish Si (1 0 0) substrate was cut into square shape biscuits of 15mm×15mm. High purity graphite was inserted into the hollow type anode as a target and cover the surface of anode at the same time which effectively avoid the impurity from anode depositing onto the substrates. Three substrates are cleaned ultrasonically in acetone and immediately mounted into the chamber at angular position and different axial positions with respect to the anode axis respectively, r= 100mm Z=50, 90, 130 mm. Generally after each fresh loading of samples for thin-film deposition, it takes some DPF shots to condition the plasma focus device for optimized efficiency [21].

At the same time, the first several shots could bombard and clean the contaminations that adhere on the lining chamber to. In order to avoid the samples exposing to weak focusing, a shutter is used to cover the surface of substrates before proper focusing was obtained. Subsequently (After PF system reaches the optimum condition) we fire ten times for SiC formation. Before each fire, chamber was first evacuated up to 4×10^{-5} mbar and then introduced H_2 subsequently as working gas at the optimum pressure of 3mbar. The work of optimization of our PF device at various working gas pressure has been done by monitoring the rogowski coil current and ion current density.

When the pulse trigger is switched on, the discharge starts over the insulator surface and then the plasma sheath comes off and is accelerated axially by the magnetic field auto-generated by the current (Lorentz force). After the current sheath runs over the upper end of the central electrode (anode), the plasma is compressed in a small region (the focus or pinch). According to the plasma instabilities, the pinch column collapse and beams of ions (proton in our case) and electron were generated. In this experiment, we take the advantages of relativistic electrons emitted from plasma focus to ablate the graphite target and forming the carbon ablation plasma. The ionic, atomic, and molecular carbon species in the ablation plasma offered good C^+ source for SiC formation. It is important to mention over here that the energetic protons would reach the substrates at first before the carbon ions. Actually, short ion pulses of high-energy density can cause very rapid heating of the surface region depending on the nature of the surface layer and the energy density of the incident ions which may cause the ablation of silicon substrate forming the momentary silicon plasma at the substrate surface. This leads to the

cleaning of the substrate surface before the deposition of SiC films [21]. The energetic protons from the next focus shot will also influence the SiC film deposited in previous shots. X-ray pinhole camera was used to photograph the pinch column. The as-deposited samples were later investigated by X-ray diffractometer (XRD), Fourier Transform Infrared Spectroscopy (FTIR), Field-Emission Scanning Electron Microscopy (SEM) and Nano-indentor.

III. Results and Discussion

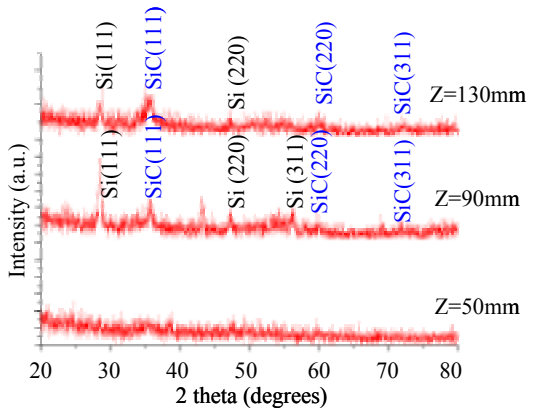

Fig2. XRD spectra for samples deposited at different positions.

1. XRD

XRD patterns were measured using an X-ray diffractometer over the range of 2θ=20—80°. Fig.2 shows the XRD patterns of as-deposited samples at different axial positions of Z=50, 90, 130 mm away from the anode. No obvious peak was found at the position of Z=50mm. In opposite, polycrystalline Si and SiC peaks were found both at the position of Z=90 and 130mm. XRD peaks which observed at 2θ = 28.4, 47.3 and 56.1° attribute to (111), (220) and (311) respectively, of Si. The presences of polycrystalline Si peaks indicate that Si substrate changed from monocrystalline to polycrystalline after ion irradiation. In addition, more peaks were found at the position of Z=90mm indicates that more energetic species were deposited here. Three XRD peaks were observed at 2θ = 35.6, 60.0 and 71.7°, corresponding to (111), (220) and (311), respectively, of 3C-SiC. Average crystallite sizes can be estimated from Scherrer's formula (Srivastava and Avasthi 1986),

$t=0.9\lambda/\beta\cos\theta$

where t is the crystallite size as measured perpendicular to the reflecting plane, λ is the wavelength of X-ray radiation, β is full width at half maximum (FWHM) of XRD peak, θ is Bragg angle. The FWHM of the SiC (111) peak at the position of Z= 90mm is smaller than that at the position of Z= 130mm. Consequently, according to the Scherrer's formula, the average crystallite size of the sample at the position of Z= 90mm is larger than that at the position of Z= 130mm. Average crystallite size is an important parameter which will influence the properties of SiC films and needs to be optimized by changing

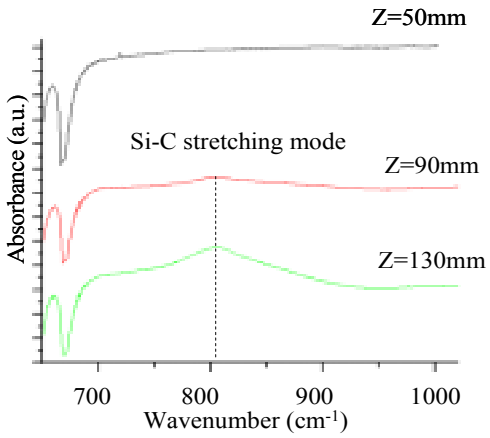

Fig.3 FTIR spectra for samples deposited at different positions.

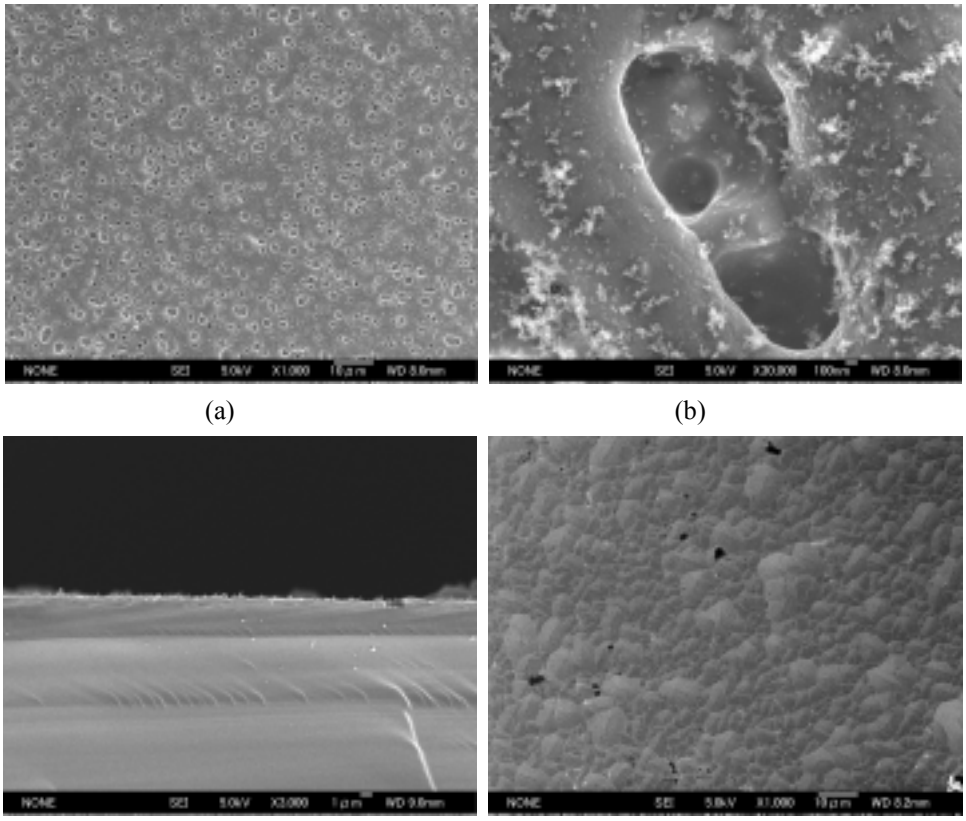

(a) (b)

(c) (d)

Fig.4 SEM micrographs of SiC film deposited at different position: (a) Z=90mm in plan view; (b) Feature graph of pore at Z=90mm; (c) Z= 90mm in cross section; (d) Z=130mm in plan view.

experiment condition in the future work.

2. FTIR absorption spectra

FTIR analysis provided valuable information on the composition of the deposited films. FTIR spectra of the samples at different positions were shown in Fig. 3. The dominant band appearing at around 800 cm^{-1} in the film at the position of Z=90, 130mm corresponds to the stretching mode of Si–C vibration. Again, we confirm from the FTIR spectra that there is no SiC formed at the position of Z=50mm which agree with the XRD results.

3. SEM

Fig. 4 (a) provides a qualitative overview of the film morphology at the position of Z= 90mm. When viewed from the top, the film structure was found to be porous morphology. At the same time, feature of the pore was displayed in Fig. 4 (b). From which, we can estimate the diameter of the pores that is around 400nm. The thickness of the deposited layer can also be obtained from cross-sectional SEM micrograph. It is shown that a thin surface layer of ~3μm is thermally affected by a growth of the upper subsurface layer of around 2μm, as shown in Fig. 4 (c). The deposited layer is speculated to be composed of mix phase

of SiC and amorphous carbon. The porous structure could also be seen from cross-section. Due to many excellent performances, such as high permeability, and high specific surface areas, porous materials have found numerous applications, including filters, catalyst supports, sensors, separations, and tissue engineering [3, 4]. The porous SiC ceramics combine the properties of porous materials with those of SiC, which is considered to have plenty of potential applications. However, mechanical properties suffer greatly from porosity. This point will be illustrated later on in the hardness results. Fig. 4 (c) shows the surface morphology of the sample at the position of Z=130mm. Comparing with the exposed sample at the position of Z= 90mm, significant difference is that no porous structure was found at this position. According to the results of ion emission dip reported by S.R. Mohanty etc. [22], that the ion flux at the position of Z= 90mm (relative bigger angular position) is higher than that at the position of Z= 130mm(relative smaller angular position). It is speculated that high ion flux (more energetic species bombarded the surface of substrate) may cause the porous structure formed.

Table 1. Hardness of exposed samples at Z=90 and 130mm.

Sample position (mm)	Morphology	Hardness (Gpa)
Z=90	Porous	12.29
Z=130	No Porous	15.1

4. Hardness

Table 1.shows hardness of the exposed samples at Z=90, 130mm. Since no SiC peak was found at Z=50mm from the XRD and FTIR, we didn't measure the hardness for this sample. The hardness at Z= 90mm is lower than Z= 130mm. Our results make a good match with Hall-Petch behavior (with crystallite size over 100nm), which gives out that the hard materials always increase in strength of crystalline with reduced crystallite size. Crystallite size has been calculated from the XRD spectra, on the other hand, as predicted by SEM, mechanical properties suffer greatly from porosity which is consistent with our hardness results.

VI. Conclusion

SiC was fabricated on Si (100) substrates using a middle energy PF device operating in Hydrogen gas under room temperature. XRD results show that polycrystalline 3C-SiC were formed at the position of Z=90, 130mm. Porous surface morphology was found at Z=90mm whilst specimen at Z=130mm was observed without porous surface morphology. High ion flux seems to be the reason of this porous structure formation. Hardness results showed very well agreement with XRD and SEM results. A study of ion flux measurement and optimization of shot number is underway. Future studies will investigate the effect of various experiment conditions (substrate temperature, working gas and anode material)

References:

1) J.C. Zolper, M. Skowronsky, Advances in silicon carbide electronics, MRS Bull. 30 (2005) 273.

2) Magunus Willander, Milan Friesel, Qamar-ul Wahab, Boris Straumal, Journal of Material Science: Materials In Electronics 17 (2006) 1– 25
3) S. Dimitrijev, H.B. Harrison, P. Tanner, K.Y. Cheong, J. Han, Properties of nitrided oxides on SiC, in: W.J. Choyke, H. Matsunami, G. Pensl (Eds.), Silicon Carbide: Recent Major Advances, Springer, Berlin, 2004, pp. 373–386.
4) S. Dimitrijev / Microelectronic Engineering 83 (2006) 123–125
5) R. A. Caruso, J. H. Schattka, Adv. Mater. 2005, 12, 1921.
6) Y. J. Wang, F. Caruso, Adv. Funct. Mater. 2004, 14, 1012.
7) M. Law, L. E. Greene; J. C. Johnson, R. Saykally; P. D. Yang, Nat. Mater. 2005, 4, 455.
8) Iijima, S. Nature 1991, 354, 56.
9) Hussain S, Ahmad S, Sharif M, Sadiq M, Waheed A and Zakaullah M 2006 *Phys. Lett.* A 349 236–44
10) J. Phys. D: Appl. Phys. 40 (2007) 127–131
11) Zakaullah M, Waheed A, Ahmad S, Zeb S and Hussain S 2003 *Plasma Sources Sci. Technol.* 12 443–8
12) Takao K, Honda T, Kitamura I and Masugata K 2003 *Plasma Sources Sci. Technol.* 12 407–11
13) Soto L 2005 *Plasma Phys. Control. Fusion* 47 A361–81
14) L.Y. Soh, P. Lee, X. Shuyan, S. Lee, R.S. Rawat, IEEE Trans. Plasma Sci. 32 (2004) 448.
15) C.R. Kant, M.P. Srivastava, R.S. Rawat, Phys. Lett. A 226 (1997) 212.
16) C.R. Kant, M.P. Srivastava, R.S. Rawat, Phys. Lett. A 239 (1998) 109.
17) R.S. Rawat, P. Lee, T. White, L. Ying, S. Lee, Surf. Coat. Tech. 138 (2001) 159.
18) R.S. Rawat, W.M. Chew, P. Lee, T. White, S. Lee, Surf. Coat. Tech. 173 (2003) 276.
19) R. Gupta, M.P. Srivastava, V.R. Balakrishnan, R. Kodama, M.C. Peterson, J. Phys. D: Appl. Phy. 37 (2004) 1091.
20) H. Zhang, Y. Jiang, S. Yang, Z. Lin, K. Feng, Thin Solid Films 349 (1999) 162.
21) L.Y. Soh, P.Lee, X. Shuyan, S, Lee, and R.S. Rawat, IEEE Transactions on Plasma Science, Vol. 32, No. 2, April 2004
22) S. R. MOHANT *et al.* Jpn. J. Appl. Phys., Vol. 46, No. 5A (2007)

FUNDAMENTAL CHARACTERISTICS OF COILGUN

S. Furuya and Y. Uehara

Gunma University, 4-2 Aramaki, Maebashi, 371-8510, Japan

ABSTRACT

The coilgun accelerates a projectile by the magnetic force produced from a current-carrying coil. We have examined the fundamental characteristics of coilgun directly energized by commercial power supply. Some simple calculations were also performed.

I. Introduction

The coilgun accelerates a projectile by the magnetic force produced from a current-carrying coil and the various applications of it are possible. Figure 1 illustrates the principle of coilgun. As a current flows through a coil, magnetic field is generated. If there is a magnetic material near the coil, it is magnetized and attracted to the coil. The projectile is accelerated to the center of coil. If the current is interrupted before the projectile arrives at the center of coil, the projectile is launched from the opposite end of coil.

The advantages of coilgun are as follows: The projectile is launched contactless, so the lifetime of the apparatus is long. No sound is produced when the projectile is launched. On the other hand, low energy conversion efficiency is the disadvantage of coilgun. Therefore, the coilgun is useful for moving a heavy load slowly, although large scale experiments to pursue high velocity have been carried out.[1)]

In general the coilgun is energized by capacitors or flywheels. With a view to applying for a low-velocity impact testing machine, we have examined the fundamental characteristics of coilgun directly energized by commercial power supply.

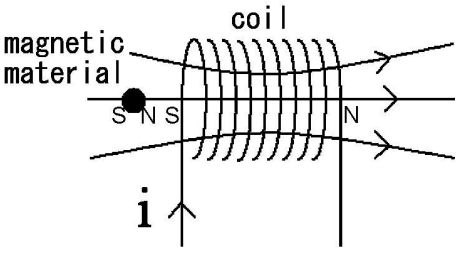

Figure 1 Principle of coilgun

II. Experimental Setup

Figure 2 shows the electrical circuit of coilgun. The circuit is driven by a triac(TG35C60, 600V, 35A). Figure 3 shows the photograph of experimental setup. As shown in the figure, the apparatus is very simple.

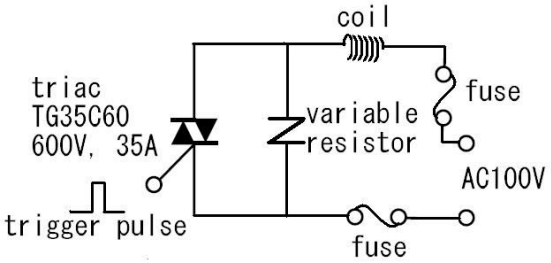

Figure 2 Electrical circuit of coilgun

Figure 3 Photograph of experimental setup

Table 1　Parameters of three coils

	outer and inner diameter of acrylic pipe (mm)	coil length (mm)	measured resistance (Ω)	measured inductance (μH)
Coil4	5×3	100	1.4	3
Coil5	10×7	50	1.3	21
Coil6	20×16	25	1.4	46

Three coils are prepared in this experiment. The details of coils are shown in Table 1. Figure 4 shows the photograph of coils. The length of acrylic pipe is 200mm and the diameter of wire is 0.3mm.

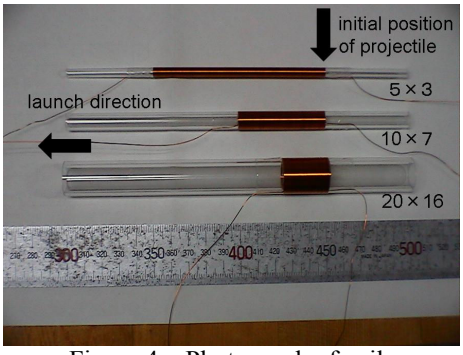

Figure 4　Photograph of coils

Figure 5 shows the voltage waveforms across the coil. Peak current is estimated to be approximately 55A by dividing the peak voltage by the measured resistance.

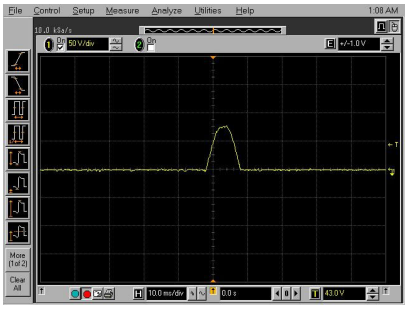

(a) positive half-wave

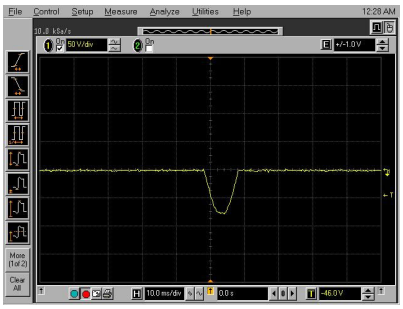

(b) negative half-wave

Figure 5　Voltage waveform across the coil

III. Experimental Results

Two sets of experiments were carried out. First, the same projectile was launched using three coils. Then the velocity of projectile was measured. Second, three projectiles were launched using the same coil.

First, M3 stud bolt, whose length is 8mm and mass is 0.27g, was launched using three coils; Coil4, Coil5 and Coil6. Figure 6 shows the results of measured flying distance. The coil was set 690mm high above the floor. The each data is the average of five shots. 'S' in the figure means that the direction of magnetic field is the same as that of launching and 'O' vice versa. The influence on the direction cannot be seen. Assuming the horizontal incidence, the velocity of projectile at the exit of acrylic pipe is calculated from the flying distance and height. Figure 7 shows the calculation results. The velocity is approximately 3m/s.

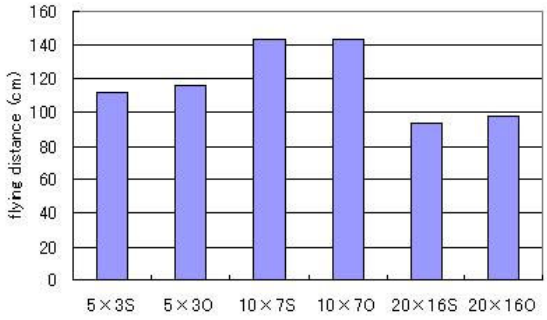

Figure 6　Flying distance of first experiment

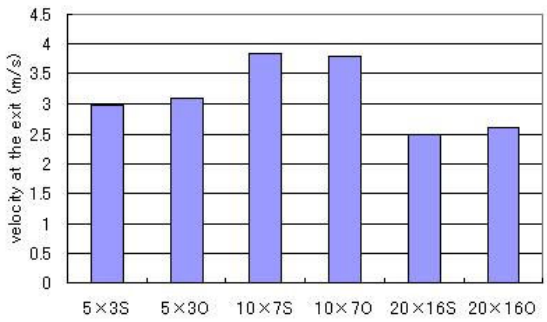

Figure 7　Velocity of first experiment

Second, three projectiles were launched using Coil6. Three projectiles are M3,M6 and M12 steel stud bolts and their length are same, 30mm. The mass are 1.25g, 4.93g and 19.8g, respectively. The each data is also the average of five shots. Figure 8 shows the flying distances. They are almost same regardless of projectile. Figure 9 shows the velocity of projectile. The velocity is approximately 3m/s. Therefore, the energy conversion efficiency is best when the projectile is M12 bolt. The efficiency is estimated to be 0.4%.

To increase the velocity of projectile we plan to apply a few half-wave voltage to the coil.

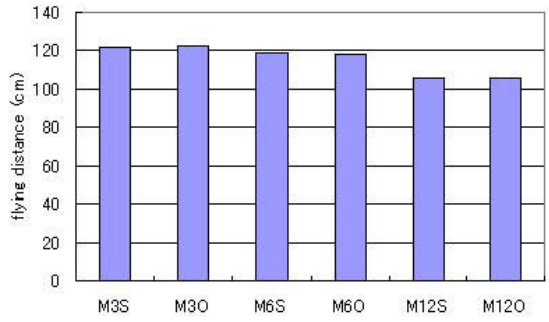

Figure 8 Flying distance of second experiment

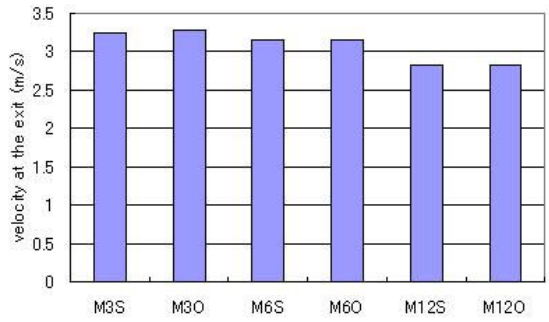

Figure 9 Velocity of second experiment

IV. Simulation

To simulate the behavior of projectile some simple calculations were performed. The force applied to the magnetic material per unit area f is

$$f = \frac{B^2}{2}\left(\frac{1}{\mu_0} - \frac{1}{\mu_S \mu_0}\right)$$

Magnetic flux density B is

$$B = k\mu_S \mu_0 H, H = nI, I = \sqrt{2} I_{rms} \sin \omega t$$

where k is Nagaoka coefficient. The motion equation to be solved is

$$m\frac{dv}{dt} = Af$$

where A is the cross section of projectile. Figure 10 shows the example of simulation result. The coil is Coil4 and the projectile is the same as that of first experiment. We assume that μ_S of the steel stud bolt is 1.05. Accurate simulation should be done in the future.

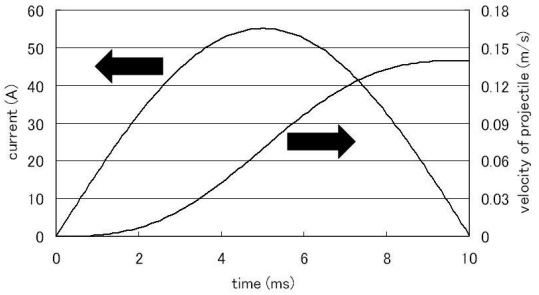

Figure 10 Example of simulation result

V. Summary

We have successfully launched the projectile from the coilgun directly energized by commercial power supply.

References

1) R. J. Kaye, “Operational requirements and issues for coilgun electromagnetic launchers”, IEEE Transactions on Magnetics **41**, 194-199 (2005).

DEVELOPMENT OF HIGH CURRENT PULSED ALUMINUM ION BEAM WITH ION SOURCE OF VACUUM ARC PLASMA GUN

K. Fujikawa, H. Miyake, H. Ito and K. Masugata

Dep. of Electrical and Electronic Engineering, University of Toyama, 3190 Gofuku, Toyama 930-8555, Japan

Abstract

Intense pulsed heavy ion beam is expected to be applied to materials processing including surface modification and the ion implantation. For those applications, it is very important to generate high-purity ion beams with various ion species. A magnetically insulated ion diode with an active ion source of a vacuum arc plasma gun has been developed in order to generate pulsed metallic ion beams. When the ion diode was operated at diode voltage $\approx$ 200 kV, diode current $\approx$ 15 kA and pulse duration $\approx$ 100 ns, the ion beam with an ion current density of $>$ 200 A/cm^2 was obtained at 50 mm downstream from the anode. From Thomson parabola spectrometer measurement, the ion beam consists of aluminum ions (Al^+, Al^{2+} and Al^{3+}) of energy 60-300 keV and the proton impurities of energy 60-150 keV. The purity of the beam was estimated to be 89 %.

1 Introduction

High-intensity pulsed heavy ion beam (PHIB) technology has been developed over the last two decades primarily for nuclear fusion and high energy density physics research [1,2]. One of most interesting topics is the application of pulsed heavy ion beam as a tool for material processing including the surface modification, thin film deposition and ion implantation [3-9]. Especially for the ion implantation process to semiconductor materials for the next generation including silicon carbide and diamond, the pulsed heavy ion beam technique has received extensive attention as a new ion implantation technology named "pulsed ion beam implantation", since the ion implantation and the surface heat treatment or the surface annealing can be completed in the same time [10].

The pulsed ion beams usually are generated in conventional magnetically insulated ion diodes (MID) with transverse magnetic field in the acceleration gap to suppress the electron flow and enhance the ion flow. The purity of the pulsed ion beam, however, is usually deteriorated by absorbed matter on the anode (flashboard) surface and residual gas molecules in the diode chamber, since the surface flashover ion source is used for the ion source of the MID. For example, the pulsed heavy ion beam produced in a point pinch ion diode contains many kinds of ions including protons, multiply ionized carbons, and organic ions [11,12]. In addition, the producible ion species are limited to the material of electrode (anode). Therefore, the conventional pulsed ion diode is not suitable for the application of the pulsed heavy ion beam to the ion implantation. It is very important for the ion implantation to develop the accelerator technology to generate high-purity ion beams with various ion species.

We have developed a new type of B_y type MID with an active ion source of a gas puff plasma gun

in order to produce the pulsed heavy ion beam with acceptable purity for the implantation process of semiconductors and the surface modification of materials. The ion diode was successfully operated at a diode voltage of 200 kV, a diode current of about 2.0 kA and a pulse duration of 150 ns [full width at half maximum (FWHM)] and the nitrogen ion beam with an ion current density of about 13 A/cm^2 and the purity of the beam of about 85 % has been obtained at 55 mm downstream from the anode [13]. The ion current density, however, is not intense enough to apply the pulsed heavy ion beam to the ion implantation process. As the next stage, in order to enhance the ion current density a coaxial type Marx generator with a voltage of 200 kV and a current of 15 kA was developed as the pulsed power generator of the ion diode and installed in the MID. As a result, when the ion diode was operated at a diode voltage of about 190 kV, a diode current of about 15 kA, and a pulse duration of 100 ns (FWHM), the nitrogen ion beam with an ion current density of 54 A/cm^2 and a pulse duration of 90 ns was obtained at 50 mm downstream from the anode. From measurements with Thomson parabola spectrometer, we found that the ion beam consisted of N^+ and N^{2+} beam with energy of 100-300 keV and impurity of proton with energy of 90-190 keV. The purity of the nitrogen beam was estimated to be 94 % [14].

For pulsed gaseous ion beams we have developed the magnetically insulated ion diode using the gas puff plasma gun as the ion source, but there has been an increasing demand for pulsed metallic ion beams for pulsed ion beam implantation and surface modification. Metal vapor vacuum ion source is suitable for the production of high-current metallic ion beams [15,16]. In order to generate a variety of metallic ion beam we have developed the magnetically insulated ion diode with an active ion source of the vacuum arc plasma gun. In this article, we present the evaluation of the properties of the pulsed ion beam including ion current density, the ion species and the energy spectrum by Thomson parabola spectrometer, spatial distribution of ion current density.

2 Experimental Setup

A schematic configuration of the intense pulsed heavy ion diode system is illustrated in Fig.1. The system consists of a high voltage pulsed power generator, a vacuum arc plasma gun, a B_y type magnetically insulated ion acceleration gap (diode), and a stainless-steel vacuum chamber with a diffusion pump package. The Marx generator with the stored energy of 240 J at a charging voltage 50 kV is used as the pulsed power generator of the ion diode. The output parameter of the Marx generator is voltage 200 kV, current 15 kA and pulse duration 100 ns(FWHM), which is applied to the anode of the ion diode. The vacuum chamber is evacuated to 5×10^{-3} Pa.

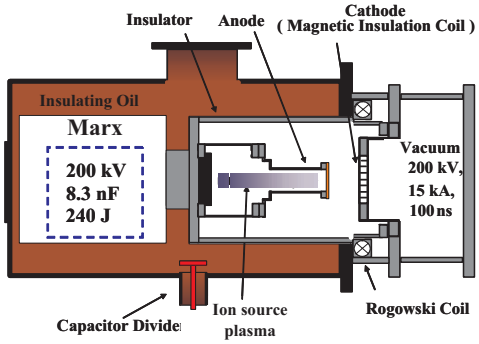

Fig.1 Schematic of the Ion Diode System.

Figure 2 shows the detail of the ion diode. The diode consists of a cylindrical anode of 115 mm length by 60 mm diameter and a cathode of grid structure. The acceleration gap length ($d_{\mathrm{A-K}}$) is adjusted to 10 mm. The top of the anode is a stainless-steel plate, in which a hole of 15 mm diameter is drilled at the central area of the anode in order to allow the source plasma to inject into the acceleration gap. The cathode has a grid structure to pass through the accelerated ions. The cathode also acts as a multi-turn magnetic field coil in order to generate a transverse magnetic field in the acceleration gap to insulate the electron flow and enhance the ion flow. Thus, as shown in Fig.2, the cathode (coil) has a shape like 8-character and is made of phosphor bronze strip

of 10 mm width and 1 mm thickness. The coil is powered by a capacitor bank of 250 μF and charging voltage 3 kV. By applying a pulse current of 10 kA with rise-time 50 μs, a uniform magnetic field of 0.7 T is produced in the acceleration gap.

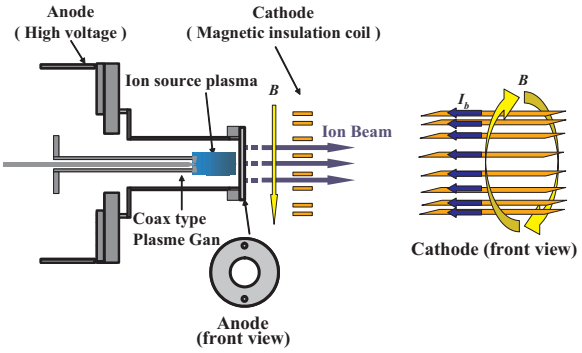

Fig.2 Cross-sectional view of B_y type MID.

A vacuum arc plasma gun is employed as the ion source of MID. The metallic plasma is produced by an ionization of cathode materials evaporated from cathodic spots of the vacuum arc discharge. Thus, high amounts of metallic ions can be achieved. Figure 3 shows the experimental setup to evaluate the characteristics of the plasma gun. As shown in Fig.3, the plasma gun has a pair of coaxial aluminum electrodes, i.e., an inner electrode of 200 mm length by 6 mm outer diameter and an outer electrode of 10 mm inner diameter. On the top of outer electrode the gap length is reduced to 1 mm. A capacitor bank of 3.3 μF for the plasma gun is charged up to 30 kV. The capacitor bank is connected anode to cathode and the discharge is triggered by applying 15 kV spark between the trigger electrode and the cathode. The ion current density of the plasma (J_i) produced by the plasma gun was evaluated by a biased ion collector placed on the central axis at $z = 50$ mm downstream from the top of the plasma gun where the anode is placed in the acceleration experiment.

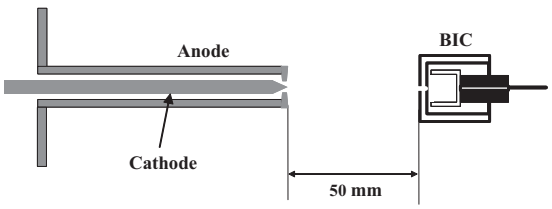

Fig.3 Experimental setup of vacuum arc ion source.

Figure 4 shows the typical waveforms of the discharge current (I_p) and the ion current density (J_i). As seen in Fig.4, the discharge current I_p has a sinusoidal waveform of peak current 12 kA and quarter cycle 6 μs. The ion beam with a peak current density J_i=158 A/cm^2 and a pulse duration of 2.5 μs is observed at about $\tau_\mathrm{p} = 7.5$ μs after the rise of I_p. This result suggests that it takes 7.5 μs for the ion beam produced in the plasma gun to reach the acceleration gap. Assuming that the plasma is produced at the rise of I_p, the delay time between I_p and J_i gives the drift velocity of 6.7×10^3 m/s, which corresponds to the ion energy of 6 eV.

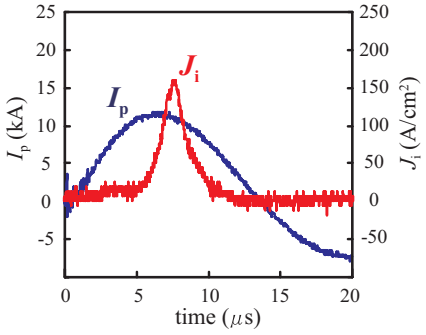

Fig.4 Typical waveforms of discharge current I_p and ion current density J_i of the plasma gun.

The diode voltage (V_d) and diode current (I_d) are measured by the capacitive voltage divider and Rogowski coil, respectively. The values of diode voltage and diode current are calculated by the ratio factor of the voltage divider 136000 and the coefficient of the Rogowski coil 27 kA/V. A biased ion collector (BIC) is used for the measurement of the ion current density.

3 Experimental Results

Figure 5 shows the typical waveforms of the diode voltage (V_d), the diode current (I_d) and the ion current density of the accelerated ion beam (J_i). Here, the Marx generator was charged up to 50 kV and fired at a delay time of τ_d=7.5 μs after the rise of the discharge current of the plasma gun. The ion-beam current density J_i is measured by the BIC placed at $z = 50$ mm downstream from the surface of the anode on the central axis. As seen in the Fig.5(a), V_d rises in 50 ns and

has a peak of 220 kV, whereas I_d rises with V_d and has a peak of 12 kA at t = 75 ns. It can be clearly seen from Fig.5(b) that the ion beam of the ion current density J_i = 230 A/cm^2 and pulse duration 40 ns(FWHM) is obtained at 45 ns after the peak of V_d.

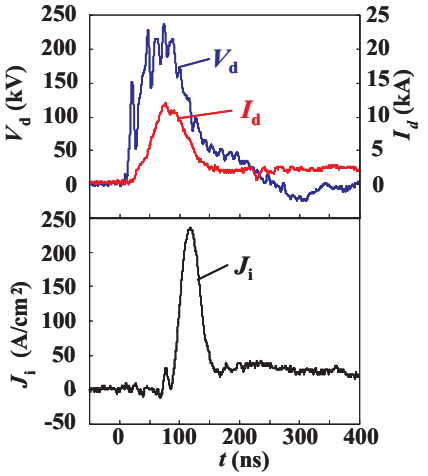

Fig.5 Typical waveforms of (a) diode voltage V_d, diode current I_d and (b) ion-beam current density J_i.

In order to evaluate the energy of the pulsed ion beam by a time of flight method (TOF), two BIC's are placed at 50 and 150 mm downstream from the surface of the anode, respectively. Figure 6 shows the experimental result of TOF. As shown in Fig.6, the TOF delay time between two BIC signals is 96 ns, which gives the velocity of 1.07×10^6 m/s. Assuming that the ion beam consists of singly ionized aluminum ion, the velocity corresponds to the ion energy of 161 keV. The

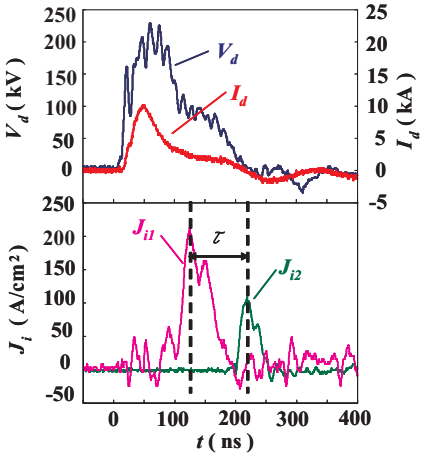

Fig.6 Experimental result of the time of flight measurement of ion energy. J_{i1} and J_{i2} are the ion current densit observed at z = 50 mm and z = 150 mm, respectively.

ion energy estimated by TOF is smaller than the peak of the diode voltage V_d. Considering the velocity of the ion beam and the distance between the acceleration gap and BIC, the ion beam corresponding the peak of J_i seems to be accelerated around the peak of V_d.

A Thomson parabola spectrometer (TPS) was employed for the evaluation of the ion species and the energy spectrum of the ion beam [12,17]. Figure 7 shows the schematics of TPS used in the experiment. The TPS is constructed of a 1st pinhole, a 2nd pinhole, a magnetic deflector, an electric deflector and an ion detecting plate of CR-39. The spot size (d) of the beam on the detector is given by

$$d = (D_1 + D_2)(L_2/L_1) + D_2$$

where D_1 and D_2 are the diameters of the 1st and the 2nd pinholes, respectively, L_1 the distance between two pinholes, and L_2 the distance between the 2nd pinhole and the detector. In our experiment, we have chosen $D_1 = D_2 = 0.3$ mm, L_1 = 20 mm and L_2 = 60 mm, hence, giving d = 2.1 mm. The deflecting magnetic field of 0.8 T and the electric field of 0.6 MV/m are applied in the vertical direction. Thus, ions are deflected in the vertical direction and the horizontal direction by the electric field and the magnetic field, respectively.

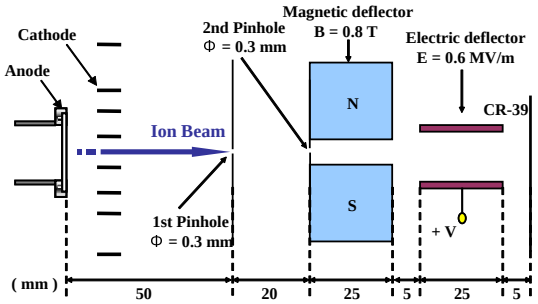

Fig.7 Schematic of Thomson parabola spectrometer.

The typical track pattern on CR-39 obtained by TPS measurement is displayed in Fig.8. The measurements by TPS were done for five ion beam shots. It is clearly seen from Fig.8 that the ion beam consists of Al^+, Al^{2+} and Al^{3+} beam with an energy of 100-300 keV and impurity of proton

with an energy of 110-170 keV. We can evaluate the ion number ratio on each ion species by counting the track number, since each ion track on CR-39 is produced by an irradiation of single ion. The energy range and the number ratio of each ion species evaluated from the track pattern are summarized in Table 1. We see from the table that 11 % of impurity ions of protons are included in the beam, hence the purity of the beam is evaluated to be 89 %. It is clearly seen from these results that the pulsed aluminum ion beam is successfully obtained by the magnetically insulated ion diode with an active ion source of the vacuum arc plasma gun.

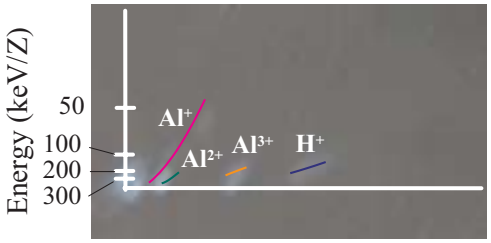

Fig.8 Typical ion track pattern on CR-39 obtained by TPS.

Table.1 Energy and number ratio of each ion species evaluated by TPS.

Ion species	Energy (keV)	Number ratio (%)
Al^{+}	60-230	89
Al^{2+}	260-400	
Al^{3+}	130-220	
H^{+}	90-130	11

Figure 9(a) shows the dependence of the ion beam current density of the ion diode (J_i) on the shot number. The experimental parameters are the same as those mentioned previously in this article. As seen in Fig.9(a), the accelerated ion-beam current density J_i is poorly reproducible and ranges from 0 to 260 A/cm^2. The average value of J_i in 60 shot is calculated to be 108 A/cm^2. In order to find out the reason of the shot-to-shot fluctuation of J_i, the reproducibility of the ion current density of the vacuum arc plasma gun (J_{si}) was evaluated. The experimental results are displayed in Fig.9(b). It is clearly seen from Fig.9(b) that there is a lot of scatter in the ion current density of the plasma gun and the reproducibility of J_{si} is very poor. The ion current density J_{si} ranges from 20 to 300 A/cm^2 and the average value of J_{si} in 40 shot is calculated to be 174 A/cm^2. Although the reproducibility of the ion beam depends on many factors including the pulse power systems, we believe that the poor reproducibility of the accelerated ion-beam current denstiy is caused by the shot-to-shot fluctuation of the plasma source produced in the vacuum arc plasma gun.

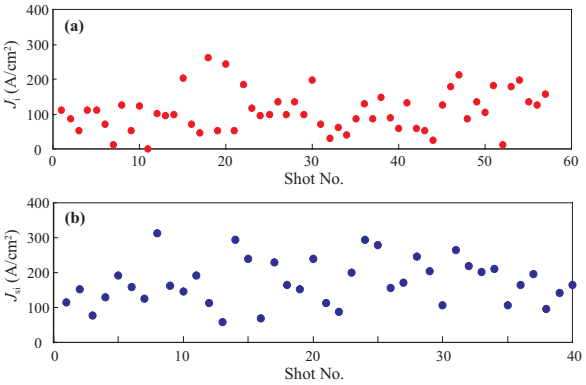

Fig.9 Dependence of (a) accelerated ion-beam current density J_i and (b) ion current density of source plasma J_{si} on shot No.

In order to evaluate the spatial uniformity of the aluminum ion beam current density, we used five BIC's arrayed at positions shown in Fig.10. With five BIC's, we obtained the azimuthal distribution of the ion-beam current density on planes perpendicular to the central axis. The experimental results are displayed in Fig.11(a). Here, each data point in Fig.11(a) is an average of five ion beam shots. The average values of J_i measured by BIC1, BIC2, BIC3, BIC4 and BIC5 are 81.5, 54.5, 154.4, 19.4 and 15.3 A/cm^2, respectively. Although the ion-beam current density J_i at each position has a lot of scatter, we believe that the ion-beam current density on the side of BIC3 is much larger than that on the opposite

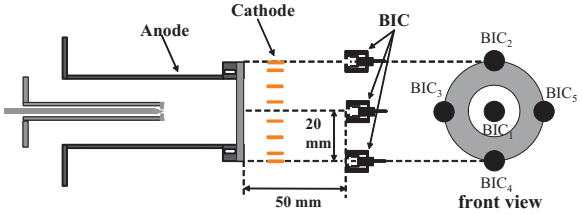

Fig.10 Experimental setup for measurement of radial distribution of ion-beam current density.

side (BIC5). This fluctuation is caused by the poor reproducibility of the ion beam.

Fig.11(b) shows the damage pattern of the ion beam recorded on the thermo-sensitive paper to measure the cross-sectional distribution of the ion-beam current density. Here, thermo-sensitive paper was placed at $z = 50$ mm downstream from the anode. It is evident from Fig.11(b) that the ion beam tends to shift to the direction of $E \times B$ drift. Positions of each BIC are shown in the figure as the reference. The azimuthal distribution of the ion beam is in fairly good agreement with the result observed in Fig.11(a)

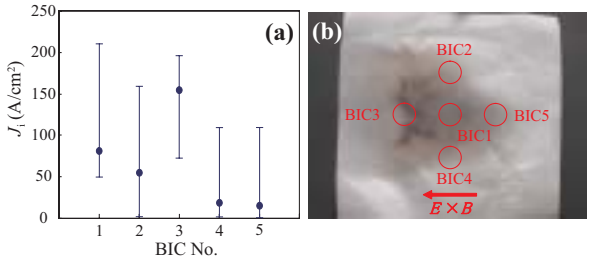

Fig.11 (a) Spatial distribution of ion current density.(b) Damage pattern of ion beam recorded on thermo-sensitive paper.

4 Summary

We have developed the magnetically insulated ion diode with an ion source of a vacuum arc plasma gun in order to generate the pulsed metallic ion beam. When the ion diode was operated at a diode voltage of about 220 kV, a diode current of about 12 kA and a pulse duration of 100 ns (FWHM), the aluminum ion beam with an ion current density of 230 A/cm^2 and a pulse duration of 40 ns was obtained at 50 mm downstream from the anode. From the evaluation of the energy and ion species of the ion beam by Thomson parabola spectrometer, we found that the ion beam consisted of Al^+, Al^{2+} and Al^{3+} ions with energy of 60-400 keV and impurity of proton with energy of 90-130 keV. The purity of the aluminum ion beam was estimated to be 89 %. It is possible to generate a wide variety of pulsed ion beam by using two types of plasma gun as the ion source, i.e., a gas puff plasma gun and a vacuum arc plasma gun. However, there seems to be some room for making improvements including the purity and the shot-to-shot reproducibility of the ion beam to apply the pulsed heavy ion beam to the ion implantation.

Acknowledgement

This work is supported in part by the Grant-in-Aid for Scientific Research from the Ministry of Education, Science, Sports and Culture, Japan. One of authors (H.I) is supported by Research for Promoting Technological Seeds from Japan Science and Technology Agency.

References

[1] J.P. VanDevender and D.L. Cook, Science **232**, 831 (1986).

[2] S. Kawata, K. Horiaka, M. Murakami, *et al.*, Nucl. Instrum. & Methods in Phys. Res. A **577**, 21 (2007).

[3] A. D. Pogrebnjak, G. E. Remnev, I. B. Kurakin, A. E. Ligachev, Nucl. Instrum. & Methods in Phys. Res. B **36**, 286 (1989).

[4] K.Yatsui, Laser Particle Beam **7**, 733 (1989).

[5] H.A. Davis, G.E. Remnev, R.W. Stinnett and K. Yatsui, Mater. Res. Bull. **21**, 58 (1996).

[6] D. J. Rej, *et al.*, Nucl. Instrum. & Methods in Phys. Res. B **127/128**, 987 (1997).

[7] H. Akamatsu, Y. Tanihara, T. Ikeda, K. Azuma, E. Fujiwara and M. Yatsuzuka, Jpn. J. Appl. Phys. **40**, 1083 (2001).

[8] B. X. Han, H. T. Zhang, W. J. Zhao, S. Yan, X. Y. Le, W. Xiang, T. M. Wang and G. E. Remnev, Suf. Coat. Technol. **158/159**, 482 (2002).

[9] C.A. Meli, K.S. Grabowski, D.D. Hinshelwood, S.J. Stephanakis, D.J. Rej and W.J. Waganaar, J. Vac. Sci. Technol. **A13**, 1182 (1995).

[10] K. Masugata, *et al.*, Proc. 25th Int. Power Modulator Sympsoium, 2002 (Hollywood, CA, USA, 2002) pp.552-555.

[11] Y. Hashimoto, M. Yatsuzuka, and S. Nobuhara, Jpn. J. Appl. Phys. **32**, 4838 (1993).

[12] K. Masugata, H. Okuda, K. Yatsui and T. Tazima, J. Appl. Phys. **80**, 4813 (1996).

[13] K. Masugata, R. Tejima, M. Higashiyama, J. Kawai, I. Kitamura, H. Tanoue and K. Arai, Plasma Device and Operations **13**, 57 (2005).

[14] K. Masugata, H. Ito, H. Miyake and L. Wang, Proc. 2007 IEEE Pulsed Power and Plasma Science Conference, (Albuquerque, NM, USA, 2007), pp.835-838.

[15] I. Brown, Rev. Sci. Instrum. **65**, 3061 (1994).

[16] H. Reich P. Spadtke and E.M. Oks, Rev. Sci. Instrum. **71**, 707 (2000).

[17] M. J. Rhee, Rev. Sci. Instrum. **55**, 1229 (1984).

PHOSPHATIDYLSERINE TRANSLOCATION INDUCED BY INTENSE BURST RADIO FREQUENCY ELECTRIC FIELDS

Naoyuki Nomura, Ryoichi Hayashi, Masahiko Yano, Kazunori Mitsutake, Sunao Katsuki and Hidenori Akiyama

Graduate School of Science and Technology, Kumamoto University
39-1 Kurokami 2-chome, Kumamoto City, Kumamoto 860-8555, Japan

ABSTRACT

This paper describes phosphatidylserine (PS) translocation in HeLa cells induced by intense burst of sinusoidal electric field (IBSEF). 200 kV/m, 50 MHz IBSEF with a burst duration of 0.2, 2 or 5 ms was applied to HeLa cells. The apoptotic activity was detected by a double staining method using annexin V-FITC and propidium iodide. The experiment shows the 2 or 5 ms long IBSEF, which gives both thermal and non-thermal effects, induced the PS externalization immediately after the exposure, while 0.2 ms long IBSEF, which is supposed to be a non-thermal exposure, induced the PS externalization gradually in time of hours, which is different from that induced by an electric pulse with a duration of nanoseconds.

I. Introduction

In the last decade biological effects of wide and narrow band electrical pulses have been intensively investigated. It is known that pulsed electric fields (PEFs) with a pulse duration exceeding 1 μs cause an increase in the permeability of cell membrane, i.e. electroporation. As the duration and the rise time of PEF are decreased to nanoseconds range, the cell response changes. Recent studies have confirmed theoretical predictions that ultra-short, high-field electric pulses can induce intracellular responses such as eosinophil sparklers[1)], calcium bursts[2,3)], apoptosis related reactions[3-5)] in the absence of membrane permeabilization and other effects associated with electroporation. Although nanoelectropulsed cells are not porated by conventional measure, membrane phospholipid scrambling is consistently observed, indicating that nanosecond pulsed electric fields can modify the organization of the plasma membrane. Some cell types recover from the disturbance[6)]. In others the distress display of phosphatidylserine (PS) on the external face of the cell persists and additional signs of nanoelectropulse-induced apoptosis appear[7)]. PS externalization–the translocation of PS from its normal position on the cytoplasmic face of the plasma membrane to the exterior of the cell – has been extensively studied, as a diagnostic sign of apoptosis[8,9)] and as a component of other physiological processes associated with cell senescence and phagocytic removal[10)]. The ability to activate this signal remotely, with non-ionizing, non-thermal (high power, but low total energy), non-invasive electric pulses may be useful in both research and clinical settings. Because PS translocation is an early event in nanoelectropulse-induced apoptosis[11)], and because considerable progress has been made toward characterization of the biophysics and physiology of this phenomenon[12)], an investigation of pulse induced PS externalization should illuminate proposed mechanisms for PS transbilayer migration and provide at the same time information about the responses of cells to nanosecond pulsed electric fields. The PS translocation is immediately associated with the application of the pulse and that it is a field-driven

event, with no more than a few milliseconds intervening between the arrival of the pulse edge and the appearance of PS molecules on the external face of the cell.

We have proposed the use of Intense Burst Sinusoidal Electric Field (IBSEF)[13] as a narrow frequency band electric field instead of rectangular pulses of which the frequency spectrum is rather broad. The IBSEF enables to give a well-defined electric field in terms of frequency, amplitude and exposure time to biological targets. In our previous work we have experimentally demonstrated that non-thermal 50 MHz IBSEF with a moderate amplitude of the order of 100 kV/m and a burst duration of 0.1 ms causes the denaturalization of intracellular DNA for Chinese hamster ovary cells. The frequency of 50 MHz is sufficiently high for the electric field to penetrate through the cell membrane. Our interests are now focused on the mechanisms of the DNA denaturalization by the intracellular electric field in addition to the possibility of the apoptosis induction by using IBSEF for the purpose of cancer therapy. This paper describes the phosphatidylserine (PS) translocation, which is one of the indications of apoptosis, on HeLa cells (human womb neck cancer cells) exposed to the IBSEF.

II. Field Distribution under Alternating Voltage

Intense and short duration electric fields of both wide and narrow band frequency spectra are capable of giving unique effects to mammalian/eukaryotic cells since the biological systems are complex of the dielectric materials including organelles, lipid bilayers, various kinds of macromolecules with three dimensional structure and small molecules. Each of them is likely to have a peculiar dielectric response to alternating current (AC) external electric fields. In particular, the biological membrane works as an insulating dielectric film, which insulates the interior from the environments. FIG. 1 contains a simplified model of spherical mammalian cells, which consists of cell and nuclear membranes, cytoplasm and nucleus. Other organelles and floating molecules are excluded for simplification. This model is appropriate to discuss how much field strength takes place inside the cell. A 10 μm diameter isolated cell is suspended in the saline solution between parallel electrodes of which the separation is 20 μm. Electrical and dimensional parameters of the cell are cited from (6). Because of the limited spatial resolution, the membranes are set to be 4 times as thick as the actual value (7 nm). The voltage of 4 V corresponds to the average electric field of 200 kV/m. The field calculations are based on the finite element method for various frequencies and are summarized in FIG. 1. Electric fields were probed at cell membrane, cytoplasm, nuclear membrane and nucleoplasm. In the low frequency range below hundreds kHz, most of the voltage applied between the electrodes comes across the cell membrane since the cell membrane interrupts the conduction current. At frequency around 10 MHz the field penetrates into the cell and becomes maximum level at the nuclear membrane. The voltages across the membranes become less with increasing frequency in the range above 10 MHz. Above 100 MHz, the distribution of the electric field is determined by the dielectric constants, resulting in the larger error of the calculation due to the use of thicker membrane. FIG. 1 indicates that we can introduce the electric field into the interior of the cell by choosing the frequency to be more than 10 MHz. Since the intracellular electric field can be a stress which biological cells usually do not experienced, the new biological reactions are expected to happen.

III. Materials and Methods

A. Cell lines and culture conditions

HeLa cells (ATCC CCL2) were cultured with alpha modified eagle minimum essential medium (αMEM, Gibco) at 37°C in a humidified, 5% carbon dioxide atmosphere[14]. The cells are incubated routinely every two days before the cell culturing condition becomes 90% confluent. The cultured cells are washed twice using phosphate buffered saline (PBS), trypsinized by 10% trypsin / ethylenediaminetetraacetic acid (EDTA) solution, and resuspended 10^6 cells/ml with αMEM.

Table 1 Electrical properties of Mammalian Cell [14].

Parameters	Values
Electrode separation	20 μm
Voltage amplitude	4 V
Cell diameter	10 μm
Nuclear diameter	6 μm
Suspending medium	$\varepsilon_r = 80$, $\sigma = 1.38$ S/m
Cell membrane*	thickness = 30 nm, $\varepsilon_r = 25$, $\sigma = 2.0 \times 10^{-6}$ S/m
Nuclear membrane*	thickness = 40 nm, $\varepsilon_r = 41$, $\sigma = 3.0 \times 10^{-3}$ S/m
Cytoplasm	$\varepsilon_r = 60$, $\sigma = 0.48$ S/m
Nucleoplasm	$\varepsilon_r = 120$, $\sigma = 0.95$ S/m

* Because of the limited spatial resolution, the membranes are set to be 30 nm, which is approximately 4 times as thick as actual value (7 nm).

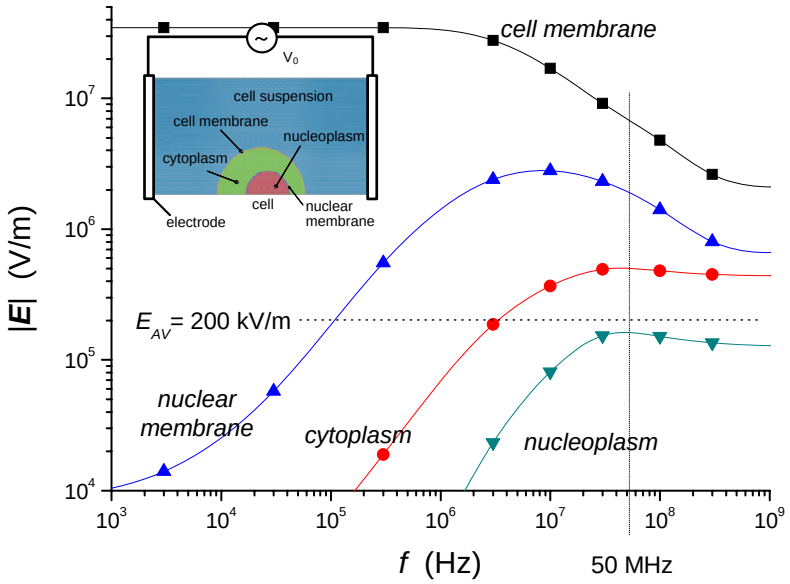

FIG. 1 Electric field distribution inside and outside biological cell membrane under alternating electric fields as a function of frequency. The average field strength is 200 kV/m.

B. Pulse generator and pulse exposures

The IBSEF exposure system, as shown in FIG. 2, consists of a signal generator (E4428C, Agilent Technologies) to provide a sinusoidal wave, a pulse generator (DG535, Stanford Research Systems) to determine the pulse duration, and an amplifier (Model 2072, EMPower RF System). The generator is connected to an exposure chamber via a 50 Ω resistive coaxial cable. The cell consists of two parallel square platinum plates as electrodes, of which the separation and cross section are 1 mm and 16 mm^2, resistively, forming an approximately 50 Ω resistive load. The capacitance of the electrodes was estimated to be 5 pF. The temperature increase of the suspending medium due to ohmic heating is approximately 1°C for the application of one pulse of 200 kV/m, 200 μs IBSEF. The voltage between the electrodes was monitored by a 500 MHz voltage probe (Tektronics, P6139A) at each shot. The suspension including HeLa cells was poured into the exposure chamber and was exposed to 200 kV/m, 50

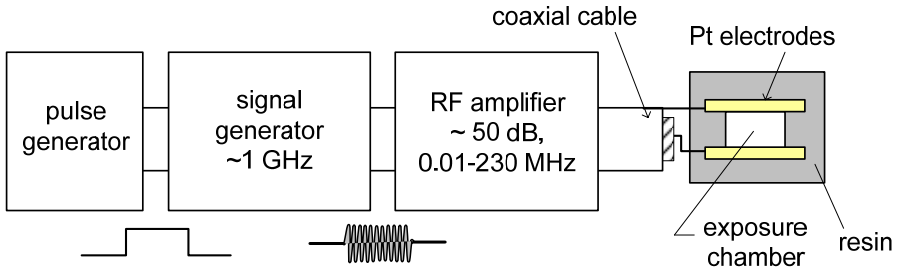

FIG. 2 Schematic diagram of the IBSEF exposure system.

MHz IBSEF with a specified burst duration. The frequency of 50 MHz enables to reduce the voltage across plasma membrane and to introduce an intense electric field to interior of the cell. The electric field of 200 kV/m is sufficiently large to cause the intracellular effect[13]. All experiments except for the incubation were conducted at room temperature (25 °C).

C. Time-lapse microscopy

The proliferation activity of the IBSEF exposed cells was observed using a time-lapse microscopy (DMI6000B, Leica) with an incubation chamber (Tokai Hit) on the stage. The IBSEF exposed suspension was scattered onto one of the partitioned culture plates in the incubation chamber. The chamber was kept at 37°C in a humidified, 5% carbon dioxide atmosphere. In order that HeLa cells adhere to the bottom, the observation was conducted at 5 hours after the IBSEF exposure. The system takes microscopic snapshots at several points simultaneously every 15 minutes for 77 hours.

D. Apoptosis detection

Phosphatidylserine (PS) is a phospholipids nutrient usually hidden in the inner-leaflet cell membranes. In an early phase of apoptosis, the PS transports to the outer-leaflet of the plasma membrane. Labeling the PS by Annexin-V-FITC enables to visualize cells in the early-to-mid phase of apoptotic cells. Propidium Iodide (PI), a fluorescent dye which is permeable to the cell, was used simultaneously to detect dead cells. The IBSEF exposed cells were incubated. At 0 (actually 15 minutes), 2 or 5 hours after the exposure, the cells were stained with both annexin V-FITC and PI (both from WAKO) simultaneously, which fluorescence in 526 nm and 650, respectively, and afterwards were observed using a fluorescent microscopy (DMI6000B, Leica).

IV. Results

A. Time-lapse microscopy

FIG. 3 shows the microscopic snapshots of the IBSEF exposed HeLa cells cultured in the incubation chamber for approximately 60 hours. FIGs. 3(a), 3(b) and 3(c) show control, 0.2 and 5 ms long IBSEF exposed cells, respectively. HeLa cells are adhesive and are likely to attach to the glass surface of the culture dish. From the sequential observation of the images, we identify the dead cells, which have not moved for a long time. In the control sample the cells are almost confluent even some are still actively in the division phase. The number of cells exposed to the IBSEF is much less than the control, and some are dead. We counted the living cells in the snapshot images and summarized the time-lapse observations in FIG. 4. It is noted that the cell number is shown in log scale. It is natural that the number of cells increases exponentially in the nutrition rich culture condition, so we can assume the growth rate of cell number as

$$N = A\exp(Bt) \qquad (1)$$

where A is a constant depending on the initial condition, and B is the cell growth rate, which is indicated by the slope of the growth curve. The time to double the cell number, so called the doubling time, can be obtained by $\ln 2/B$. The constant B and the doubling time are obtained by fitting equation (1) to the growth curve. In the control sample, the growth curve is a little saturated around t = 50 hours. This is

because the culture plate is nearly confluent. The growth rate and the doubling time together with the exposure condition are summarized in Table 2. The temperature increase in the medium is calculated by the energy deposition. However, the temperature increase should be spontaneous in time of ms range and much smaller than the values in Table 2 because of heat conduction to the electrode. The growth rate is evaluated in the time range $0 < t < 55$ hours since the rates tend to be changed during the observation. The larger energy deposition is likely to suppress strongly the proliferation activity of the cells. For the samples exposed to IBSEF, their growth rates are likely to increase after several tens of hours, indicating that surviving cells appear to be recovering. The recovery time tends to be longer for larger energy deposition to the cells, and to be associated with the doubling time. These data imply that surviving cells, which are inactivated, might recover after they conduct their cell divisions. With the burst durations of 2 and 5 ms the IBSEF exposure is accompanied by a significant temperature increase for biological matter. We cannot distinguish the effect of electric field from the thermal effect in this experiment.

B. Phosphatidylserine translocation

50 MHz, 200 kV/m IBSEFs with various burst durations between 0.2 and 5 ms were applied to HeLa cells. Cells were stained with both annexin V-FITC and PI a certain time after the IBSEF application, and observed by a fluorescent microscope. Results of the double staining method were classified into three cases; (1) negative to both annexin V and PI, indicating living cells, (2) positive to annexin V and negative to PI, indicating cells in the early phase of apoptosis, and (3) positive to both annexin V and PI, indicating dead cells. FIG. 3 shows the microscopic images with bright field and fluorescence from either annexin V or PI for the negative control and for 0.2 ms long IBSEF application. FIG. 3 shows several cells with fluorescence from annexin V, while no PI fluorescent was observed. The percentage of the cells in the apoptotic process and the dead cells were evaluated by a cell counting. FIG. 4 shows a summary of the observation, cell percentage for the case (2) and the case (3) as a function of post cultivation time after the IBSEF application. Each datum includes approximately 300 cells. The controlled cells did not show apoptosis or death during the observation. In the case of the 5 ms long IBSEF application, which is accompanied by an instantaneous temperature increase of the medium by approximately 20°C, approximately 40% of the cells showed the apoptosis immediately after the IBSEF application. After 5 hours the apoptosis ratio was decreased thus immediately activated apoptotic cells were dead. On the other hand, the application of 0.2 ms long IBSEF with a slight temperature increase of less than 1°C did not cause the PS externalization just after the exposure, while the percentage of the apoptotic cells was gradually increased to be approximately 15% after 5 hours. The delayed occurrence or the PS externalization implies that the non-thermal IBSEF does not directly cause the PS externalization, or apoptosis reaction, but is likely to trigger the biological process related to the PS externalization.

V. Discussion

According to the experiments of nanosecond rectangular pulsing to mammalian cells (Schoenbach et al. used 60 ns, 5 MV/m pulses[2,10] and Vernier et al. used 30 ns, 2.5 MV/m pulses[3]), intense nano-electrical pulsing induces nano-pore formation, resulting in the PS translocation due to the lateral molecular diffusion through the nano-pore. This PS translocation occurs immediately after the pulsing within a few seconds. External electrical pulses directly stimulate the cell membrane in this case. For the case of the fast rising pulse we can calculate the voltage across the plasma membrane, when a square wave pulse with voltage of $V_a = Ed$ is applied, where d is the distance between the two electrodes (FIG. 1), and E is the average electric field in the medium. Starting from the resting voltage V_r, which is of the order of 70 mV for many cells, the voltage across the plasma membrane increases with time until the end of the voltage pulse, and reaches a value of V_M +/- V_r at the poles given by [2]

$$V_M = fE(D/2)\{1-\exp(-t/\tau_C)\} \qquad (2)$$

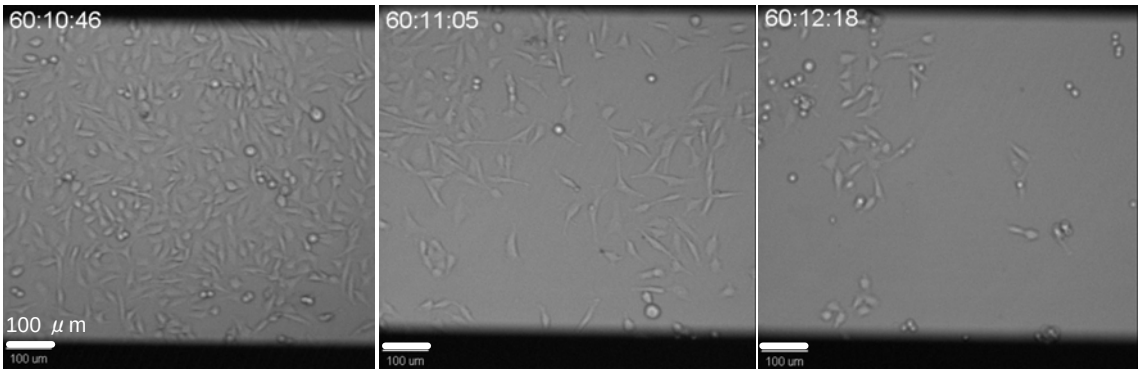

(a) control (b) 0.2 ms long IBSEF (c) 5 ms long IBSEF

FIG. 3 Microscopic snapshots of HeLa cells approximately 55 hours after the IBSEF exposure. The number in each image shows the time from the beginning of the observation (hours:minutes:seconds).

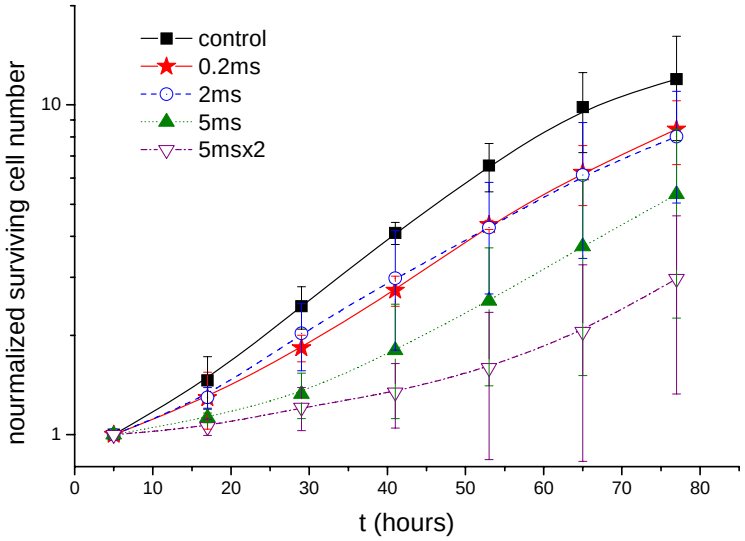

FIG. 4 Growth curves of HeLa cells exposed to 200 kV/m, 50 MHz IBSEF with application of various burst durations (one pulse of 0.2, 2, 5 ms and two pulses of 5 ms). The IBSEFs were applied at $t = 0$. The each observation starts at 5 hours after the IBSEF exposure. The cell numbers are normalized to that at 5 hours after the exposure. Each curve is the average of 5 independent trials.

Table 2 Summary of the time-lapse observation of HeLa cells exposed to the IBSEF.

Shot condition		Energy expenditure (mJ/16 μl)	Temperature increase (°C)	Growth rate B (hour^{-1})*	Doubling time (hours)*
E_{av}, f	duration × number				
	Control	-	-	0.041	17
200 kV/m 50 MHz	0.2 ms	59	0.88	0.030	23
	2 ms	590	8.8	0.028	25
	5 ms	1500	22	0.021	33
	5 ms × 2	1500 × 2	22	0.011	63

* Evaluated for the time until 50 hours.

where f is a geometry factor (1.5 for spherical cells), and D is the diameter of the cell. τ_C is the charging time constant for the plasma membrane, which is 75 ns for 10 μm diameter spherical cell floated in the 100 Ωcm resistive medium. Nanosecond rectangular pulses are extremely short duration but its frequency spectrum is broad and the electric field is in the MV/m range, resulting in the trans-membrane voltage exceeding 100 MV/m. This extremely high field forms the nano-pores, which allows only small molecules to pass thorough the pore. Molecular dynamic simulation[9] indicates that the extremely high electric field of 0.5 V/nm forms the nano-pore within only 3 nanoseconds. However, the IBSEF with moderate electric fields of 200 kV/m causes the electric field of the order of 10 MV/m on the plasma membrane, which is 1/10 for the nano-pulse application. On the other hand, high frequency alternative fields of more than 10 MHz enable to cause the intracellular electric field, which is the same level as the external electric field. This 0.2 ms lasting alternating electric field might give a stress to the cell. In the case of the 0.2 ms long IBSEF application, the PS externalization occurs gradually after the exposure, which is induced by nano-pulsing. The effect of IBSEF seems to be different from that of the nano-pulsing, and rather similar to the apoptosis process caused by conventional stimuli, such as exposure to UV, radiation, heat or chemicals.

Acknowledgement

This work has been supported by the 21 Century COE program "Pulsed Power Science and its Applications".

References

1) K.H. Schoenbach, S.J. Beebe, E.S. Buescher, J. Bioelectromagnetics 22, p.440 (2001)
2) K.H. Schoenbach, et al, IEEE Trans. Dielectr. Electr. Insulat. Vol. 14, No. 5; pp.1088-1109 (2007)
3) P.T. Vernier, Y. Sunc, L. Marcua, C.M. Craft, M.A. Gundersen, Federation of European Biochemical Societies Letters 572, pp.103-108 (2004)
4) Y. Sun, P.T. Vernier, M. Behrend, L. Marcu, M.A. Gundersen, IEEE Trans. Nanobioscience, Vol. 4, No. 4, pp.277-283 (2005)
5) P.T. Vernier, A. Li, L. Marcu, C.M. Craft, M.A. Gundersen, IEEE Trans. Dielectr. Electr. Insulat. Vol. 10, No. 5; pp.795-809 (2003)
6) P.T. Vernier, Y. Sun, L. Marcu, C.M. Craft, M.A. Gundersen, Biophys. J. Vol. 86, pp.4040–4048 (2004)
7) I. Ermorina, Y. Polevaya, Y. Feldman, B. Ginzburg, M. Schlesinger, IEEE Trans. Dielectr. Electr. Insulat. Vol. 8, No. 2, pp.253-261 (2001)
8) D.A. Stewart, Jr., T.R. Gowrishankar, J.C. Weaver, IEEE Trans. Plasma Science, Vol. 32, p.1696 (2004).
9) Q. Hu, S. Viswanadham, R.P. Joshi, K.H. Schoenbach, S.J. Beebe, P.F. Blackmore, Phys. Rev. E71, 031914 (2005)
10) W. Frey, J.A. White, R.O. Price, P.F. Blackmore, R.P. Joshi, R. Nuccitelli, S.J. Beebe, K.H. Schoenbach, J.F. Kolb, Biophys. J. Vol. 90, p.3608 (2006)
11) A.G. Pakhomov, A. Phinney, J. Ashmore, K. Walker III, J. Kolb, S. Kono, K.H. Schoenbach, M.R. Murphy, IEEE Trans. Plasma Science Vol. 32, p.1579 (2004).
12) J.C. Weaver, IEEE Trans. Dielectr. Electr. Insulat. Vol. 10, No. 5, pp. 754-768 (2003)
13) S. Katsuki, N. Nomura, H. Koga, H. Akiyama, I. Uchida S.-I. Abe, IEEE Trans. Dielectr. Electr. Insulat. Vol. 14, No. 3, pp. 663-669 (2007)
14) H. He, D.C. Chang, Y.K. Lee, Bioelectrochem., Vol. 70, Iss. 2, pp.363-368 (2007)

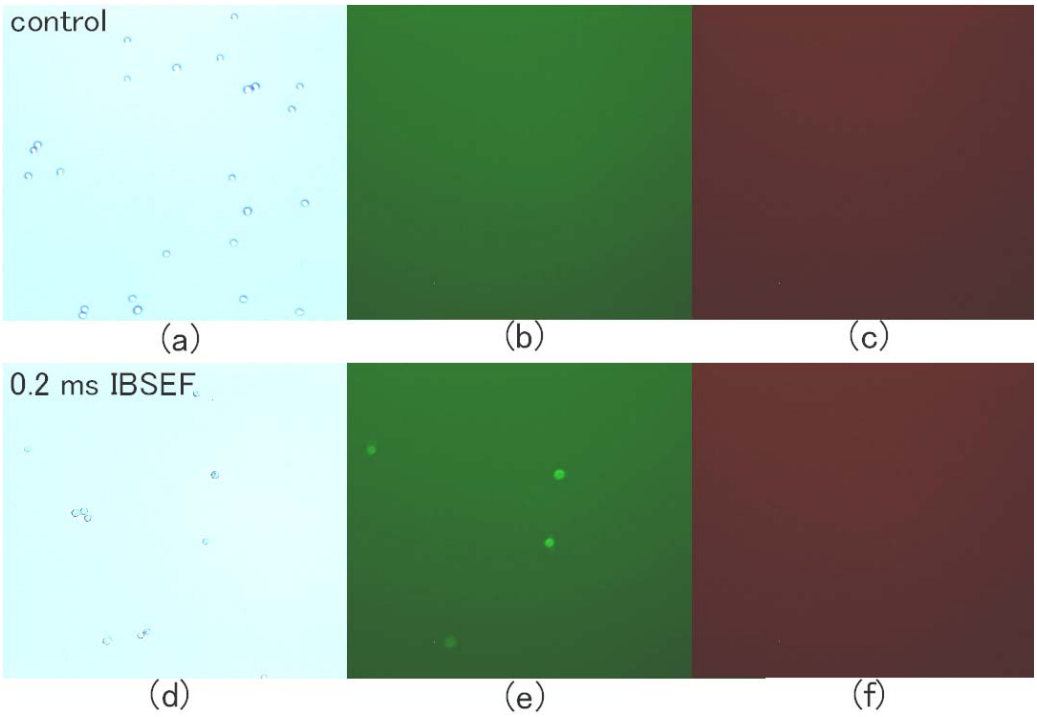

FIG. 5 Microscopic view of HeLa cells. (a) and (d) are bright field images. (b) and (e) are fluorescent images from annexin V-FITC. (c) and (f) are fluorescent images from propidium iodide. A set of (a)-(c) shows control cells, and set of (d)-(f) shows cells 5 hours after the exposure to 0.2 ms long IBSEF.

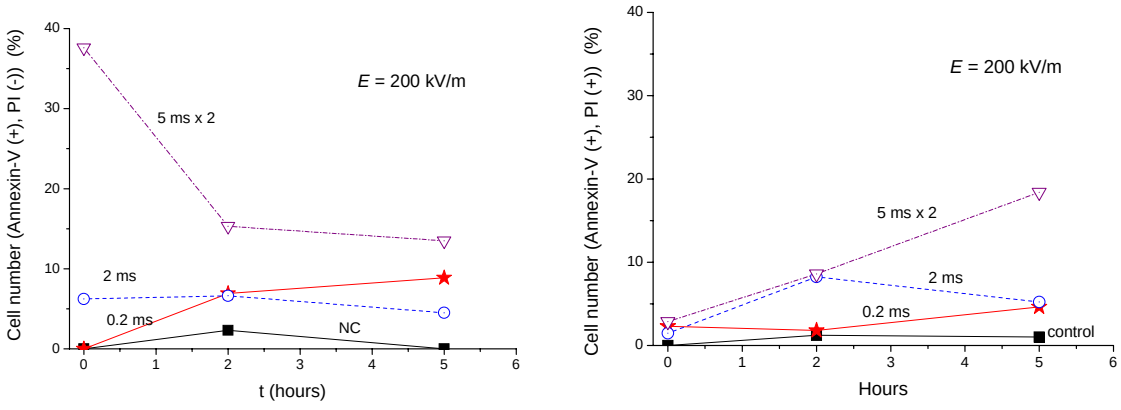

(a) (b)

FIG. 6 Temporal variations of the percentages of the apoptotic cells (a) and dead cells (b) numbers for negative control and for the exposure to 200 kV/m, 50 MHz IBSEF with various burst duration (0.2, 2 and 5 ms ×2). Each datum represents approximately 300 cells.

DEPOSITION OF DIAMOND-LIKE-CARBON FILM BY ATMOSPHERIC PRESSURE TRANSIENT GLOW MICRODISCHARGE USING FAST HIGH-VOLTAGE PULSE TRAIN GENERATOR

S. Ibuka, K. Harada, J. Kikuchi, K. Igarashi and S. Ishii

Tokyo Institute of Technology, 2-12-1-S3-9, O-okayama, Meguro-ku, Tokyo, 152-8550, Japan

ABSTRACT

Utilizing atmospheric pressure transient glow micro plasmas, diamond-like-carbon (DLC) film deposition was examined. To obtain stable high-power glow discharge, we developed novel driving technique of the transient glow microdischarge with miniature gas flow powered by high-voltage pulse train. It was obtained by using the burst pulse generator with a nonlinear transmission line (NLTL), which consisted of chip monolithic ceramic capacitors as a nonlinear element. Repetitive burst pulses with an output voltage of 2.2kV and a pulse width of 40 ns were generated. The equivalent frequency of the pulse train was 12.5 MHz. A stabilization effect of the highly repetitive operation on the discharge made it possible to deposit the DLC film on a stainless steel plate cathode under atmospheric pressure condition with the deposition rate of up to 1.5μm/min. The characterization of the DLC film was also carried out using SEM observation, Raman spectroscopic analysis and hardness measurement with a nanoindentor.

I. Introduction

Atmospheric pressure glow discharges (APGDs) attract growing attention in variety of plasma applications. Especially, plasma processing, such as a plasma etching and a deposition, requires the APGD processes because of their high processing rate and inexpensive apparatus. For those applications, generation of the high-power glow plasma is necessary to obtain enough particle density. However, a probability of a glow-to-arc transition increases drastically with injection power.

To obtain stable high-power APGDs, a key issue is the suppression of a glow-to-arc transition. In recent years, a utilization of microplasmas is a promising candidate in various techniques to suppress the glow-to-arc transition. The smallness of the microplasmas obstructs the growth of the spatial instability. In addition, the large specific surface area of the microplasma promotes the cooling of the excess heat that leads to the grow-to-arc transition.

We reported the direct current APGDs between microgap electrodes with fast miniature gas flow.[1)] The electrical power, however, injected into the plasma is too small to realize plasma deposition process. To obtain high-power stable APGDs, utilization of a transient glow discharge is suitable. It is usually obtained in short duration before the glow-to-arc transition occurs. In order to generate the transient glow discharge, high voltage pulse with extremely short duration is required. In the case of the microgap under the atmospheric pressure condition, the pulse duration is typically below 100ns.[2)] However, it is not easy to obtain such an extremely short pulse voltage using the conventional power semiconductor devices.

To obtain such a high voltage pulses with short durations, we devised to utilize a nonlinear transmission line (NLTL). The NLTL consists of linear inductors and nonlinear capacitors, of which capacitance changes depending on the applied voltage. In the NLTL, a short duration voltage pulse propagates as a nonlinear wave and changes its temporal shape into a solitary wave with shortening the pulse width and growing the amplitude. For a longer duration input pulse, it split in several pulses with short duration and serves as a burst pulse generator.

In this study, we examine the feasibility of the transient glow microdischarge to realize the DLC film deposition under atmospheric pressure condition.

II. High-Voltage Pulse Train Generator

A. Basic theory of pulse train generation

In the previous study, we reported that the transient glow discharge in the microgaps requires extremely short voltage pulses with the duration of several tens of nano seconds.[2] Although the recent progress in the power semiconductor switching devices enable us to obtain such fast switching characteristics, large switching losses obstruct highly repetitive operation. In general, the highly repetitive operation can enhance the stability of the APGDs.[3] A residence time of flowing gas in the microgap electrode is short, because its flow velocity is high and the size of microplasmas is small. It is estimated to be 1.2-6.0μs between the electrodes with a separation of 100-500μm and a flow rate of 100sccm. To obtain the stabilization effect of the APGDs, the repetition frequency above 1MHz is required. This requirement exceeds the specification of the commercially available power semiconductor devices even with fast switching capabilities.

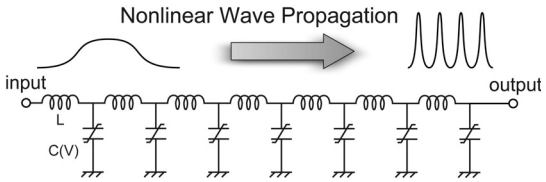

Figure 1 Basic principle of the pulse train generation.

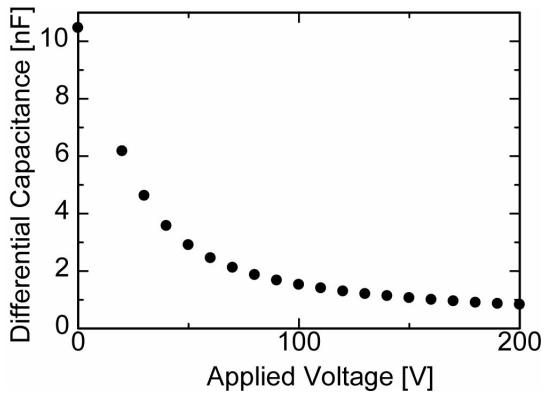

Figure 2 C-V characteristics of the chip monolithic ceramic capacitors.

In this study, we developed a fast high-voltage pulse train driving technique to overcome this problem. Figure 1 illustrates a basic principle of the technique. A relatively long rectangular pulse was generated by a pulse forming circuit using power semiconductor switching devices. The rectangular pulse entered into a burst pulse generating circuit composed of a nonlinear transmission line (NLTL). It consisted of linear inductors and nonlinear capacitors, of which capacitance decreased with increasing the applied voltage as shown in Figure 2. In the NLTL, voltage pulses with a short pulse width propagate as a nonlinear wave and changes its temporal shape into a solitary wave shortening its pulse width and growing the amplitude. When the rectangular pulse with a longer pulse width entered into the NLTL, it split in several pulses with short duration and it worked as a burst high-voltage pulse generator.[4),5)] The pulse duration and the interval of the individual pulse are adjustable by choosing circuit parameters of the NLTL. The regulation of the average injection power was possible by simply adjusting the repetition frequency of the initial rectangular pulse. The NLTL is composed of only passive circuit elements. Therefore, the highly repetitive operation with high energy efficiency will be achieved.

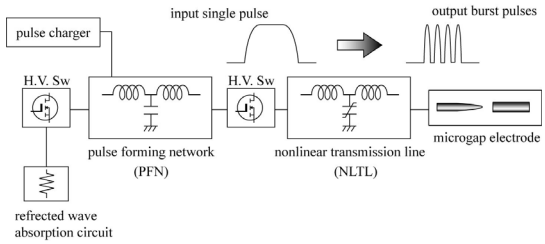

Figure 3 Block diagram of the burst pulse generator.

B. Configuration of pulse train generator

Figure 3 shows a block diagram of the pulse generator with the NLTL and the pulse forming circuit. In the previous study, we used a pulse forming line (PFL) using 3C-2V coaxial cables to obtain high-voltage short pulses.[2] Although the PFL has feature to generate fast rectangular high-voltage pulses, the size of the pulse generator circuit is large because of the coaxial cables whose length determines the pulse duration. The size of the generator is an important factor to realize the industrial applications of the microplasma in various fields. Therefore, we utilized a pulse forming network (PFN) to generate the initial rectangular voltage pulse. The PFN, which consisted of an LC ladder circuit and high-voltage switching devices, was fabricated in compact size and generated high voltage pulses with the pulse width of 90-1000ns. To achieve highly repetitive operation up to 2kHz and the output voltage to be high enough to drive discharges in the microgap electrode, four fast high-voltage IGBT devices (SiCAD BUP313, rated

voltage:1.2kV) were connected in series as a switching device. The stacked semiconductor switch was safely operated up to 3kV.

The NLTL was composed of air-core inductors and nonlinear capacitors with the voltage characteristics shown in Figure 2. Unfortunately, the nonlinear capacitors are not commercially available; we used chip monolithic ceramic capacitors (Figure 4) as nonlinear elements. Owing to laminating structures of thin ferroelectric ceramics layers, the

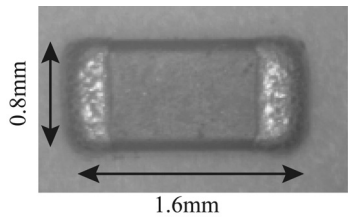

Figure 4 Photograph of the chip monolithic ceramic capacitor.

breakdown voltage is high and strong nonlinear characteristics are obtained. In addition, the surface mount type configuration eliminates the residual inductance of the capacitor. Since the rated voltage of the capacitor was too low to build the high-voltage pulse generator, we connected ten capacitors in series fabricating on a printed circuit board. The stacked capacitor array was operated up to 2.2kV.

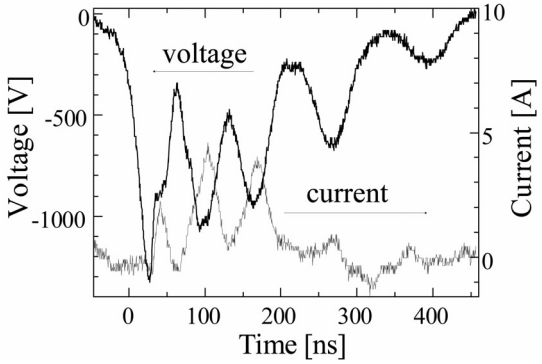

Figure 5 Typical voltage and current waveform of the pulse train generator.

Usually, the impedance of the discharge plasma decreases to 10-20Ω. It is difficult to obtain impedance matching completely between the generator and the plasma load. Therefore, we devised a reflected wave absorption circuit to eliminate the effect of the impedance mismatching.[2] The energy transfer efficiency of the pulse generator, however, is not high because the half of the stored energy in the PFN is consumed in the resistor of the reflected wave absorption circuit.

Figure 5 is a typical voltage and current waveforms of the burst pulse generator. The initial rectangular pulse with 300ns duration generated by the PFN becomes the pulse train of three large solitary waves having 40ns pulse width in FWHM and followed by two small ripples. The interval of each solitary wave is 80ns. The equivalent frequency is 12.5MHz. It is noted that the circuit parameters of the NLTL and the PFN should be adjusted as appropriate value to minimize the energy loss caused by the ripple generation.

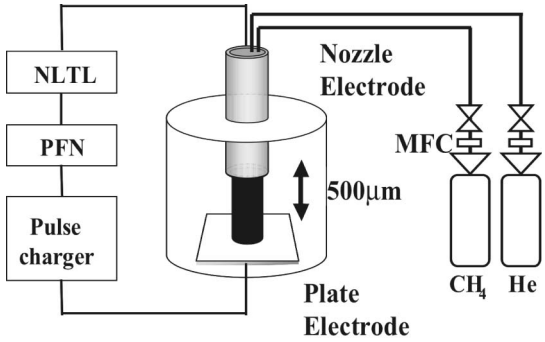

Figure 6 Experimental apparatus for DLC film deposition.

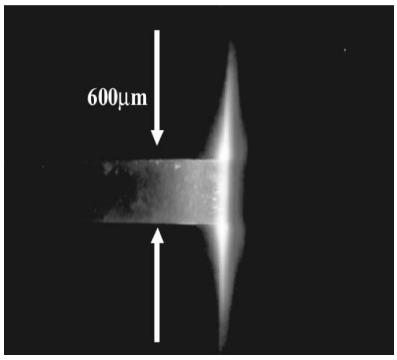

Figure 7 CCD photograph of the stable

III. Experimental Setup for Diamond Like Carbon Deposition

The experimental apparatus for the DLC film deposition is shown schematically in Figure 6. Microgap electrode system consisted of a thin nozzle anode and a SUS plate cathode was placed in a small chamber. Methane gas diluted with helium was fed through the nozzle cathode as discharge gas. The

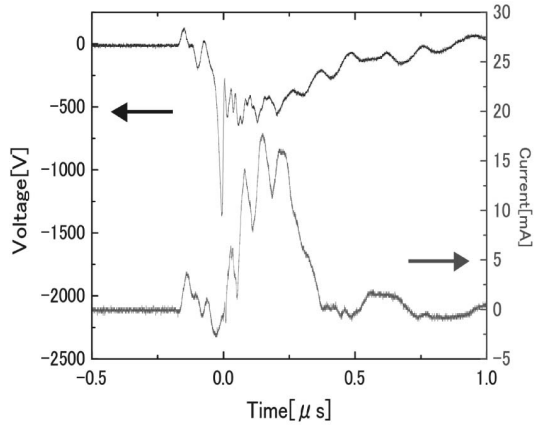

Figure 8 The voltage and the current waveform of the stable transient microdischarge.

flow rate of the methane and the helium are 200~1400sccm and 1~8sccm respectively. The high voltage pulse train generator was connected to the electrodes. The voltage and the current waveforms were monitored by a digital oscilloscope to confirm the generation of the stable transient glow microdischarge.

Figure 7 shows the CCD photograph of the stable transient glow microdischarge. In this case, the outer diameter of the nozzle anode is 600μm. A large bright area uniformly expands on the surface of the cathode plate in spite of the small anode area. Figure 8 show the voltage and the current waveforms corresponding to figure 7. The high sustaining voltage of the discharge illustrates the generation of the stable transient glow discharge. From figure 8, the injected energy into the microplasma is calculated as 1.58mJ/pulse. The generation of the high-power transient glow microdischarge was successfully confirmed.

IV. Results and Discussions

A. DLC film deposition

Figure 9 shows a microscope image of the SUS cathode surface after discharge. A donut shape deposit is obtained clearly. The donut shape corresponds with the shape of the nozzle anode (6mm o.d / 3mm i.d). It should be noted that, no deposit could be obtained with low-power dc driven APGDs although the same discharge gas and the electrodes were applied.

Figure 10 shows a typical Raman spectrum of the deposit. The pair of bands around 1360cm^{-1} and 1580cm^{-1}, respectively designated the D-band and G-band are obvious in the spectrum. A broad shape

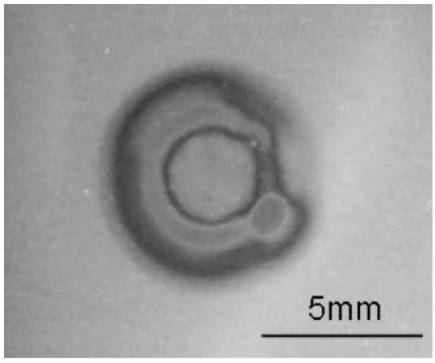

Figure 9 Microscope image of the deposit.

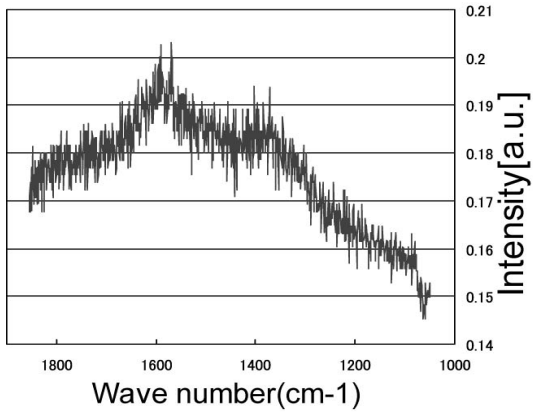

Figure 10 Typical Raman Spectrum of the deposit

of the D-band and the G-band is characteristic of the DLC film. These results suggest the successful generation of the DLC film.

B. Effect of the Anode Shape

As shown in figure 9, the shape of the deposit is affected by the anode configuration. It can be considered that the DLC deposition process requires strong electric field near the cathode substrate. From the viewpoint of industrial applications, uniform shape of the DLC deposition is desirable. To obtain uniform electric field, we developed mesh type anode as shown in figure 11.

The DLC deposition was examined with several mesh type anodes with various inner diameters. Figure 12 shows the photographs of the discharges and DLC films for each case. The flow rates of the discharge gases were unchanged for all cases (helium: 1400sccm, methane: 3sccm). The inner diameter of the anode has small effect on the

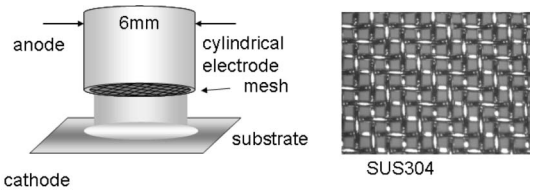

Figure 11 Schematic of the mesh type anode.

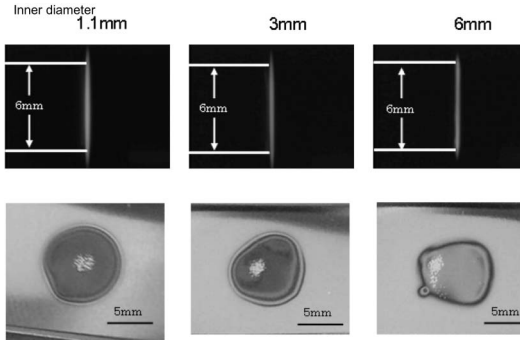

Figure 12 DLC deposition with mesh type anode.

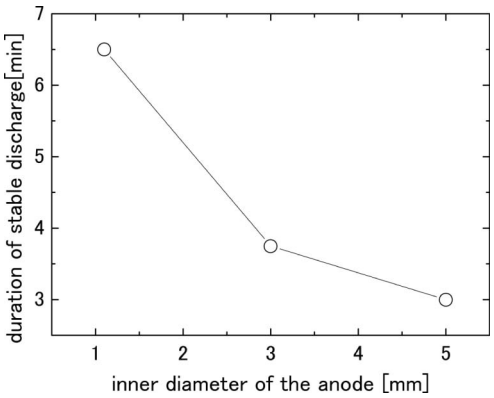

Figure 13 Duration of the stable discharge.

uniformity of the DLC film. However, the stability of the discharge is significantly affected by the inner diameter of the anode. Figure 13 shows the duration of the stabilized discharge for each case. At the beginning of the discharge, the transient glow microdischarge is stabilized easily. However, as the growth of the DLC deposition, the discharge tends to be unstable since the DLC has highly insulative property. In order to obtain stable discharge for long duration, the uniformity of deposit and intense stabilization effect of the discharge are required. As shown in figure 13, small inner diameter of the anode is favorable to obtain the stable discharge.

C. Cooling Effect of the Gas Flow

A temperature of the substrate is important

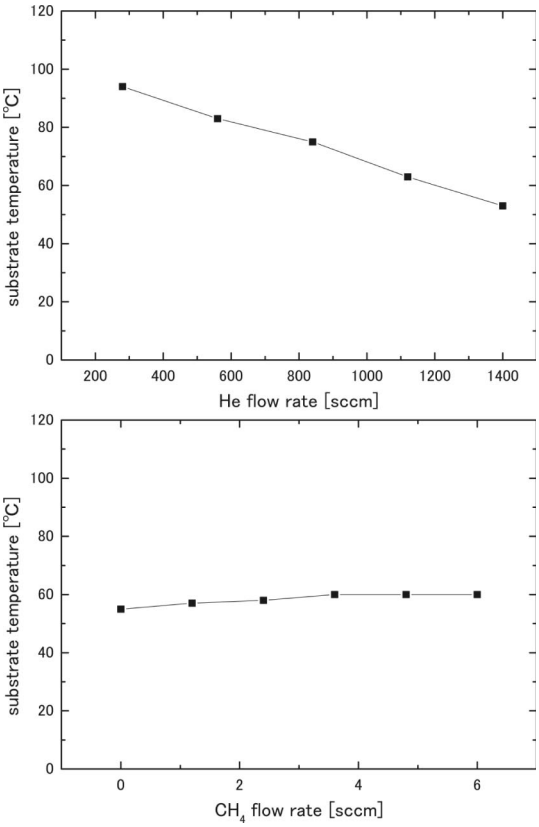

Figure 14 Substrate temperature.

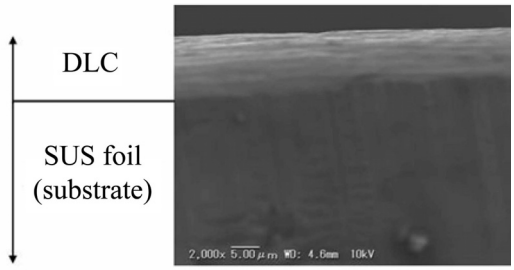

Figure 15 Cross sectional SEM image of the DLC film.

parameter in the DLC deposition process. The temperature measurement of the backside of the SUS cathode was carried out with a thermocouple varying the flow rate of the helium and the methane. The experimental results are illustrated in figure 14. The flow rate of the helium has remarkable influence on the substrate temperature although methane flow rate has no effect. This cooling effect of the helium can be considered as one of the reason of the discharge stabilization effect.

D. Characterization of the DLC Film

To estimate a deposition rate of the DLC, a thickness of the deposit was measured by SEM

observation. Figure 15 shows the cross sectional SEM image of the DLC film. In this case, a SUS foil was used as a substrate to make cutting the substrate easy. The deposition duration was 6.5min and the gas flow rate was 1400sccm for helium and 3sccm for methane. According to the SEM image of figure 15, the thickness of the DLC film is measured as 10μm. Therefore the deposition rate is calculated as 1.5μm/min.

A hardness measurement of the DLC film was also carried out using the nanoindentor. The Vickers hardness of the DLC film was estimated as HV489.

V. Summary

Utilizing fast high-voltage pulse train generator with the NLTL, the atmospheric pressure high-power transient glow microdischarge was successfully obtained. The pulse train driving technique suppresses the glow-to-arc transition and realizes high-power injection to the microplasma. To investigate the feasibility of the transient glow microdischarge to industrial applications, the DLC film deposition process was examined experimentally. Using methane and helium mixture as discharge gas, the uniform deposit with thickness of 10μm was obtained on the cathode surface in 6.5min under atmospheric pressure condition. According to the Raman spectroscopic analysis, the deposit was identified as the DLC. The Vickers hardness of the DLC film was estimated as HV489 by the nanoindentor measurement.

References

1) T. Yokoyama, S. Hamada, S. Ibuka, K. Yasuoka, and S. Ishii, "Atmospheric dc discharges with miniature gas flow as microplasma generation method," J. Phys. D: Appl. Phys., **38**, pp. 1684-1689, (2005)
2) S. Ibuka, R. Mikami, F. Furuya, K. Ogura, K. Yasuoka, and S. Ishii, "Generation of Atmospheric Pressure Transient Glow Discharge in Microgap Electrode with Nanosecond Pulsed Voltage," IEEJ Trans. on Fundamental Materials, **127**, pp. 411-416, (2007)
3) S Kanazawa, M Kogoma, T Moriwaki and S Okazaki, "Stable glow plasma at atmospheric pressure," J. Phys. D: Appl. Phys., **21**, pp. 838-840, (1988)
4) Colin Richard Wilson, Miles M. Turner, and Paul W. Smith ,"Pulse Sharpening in a Uniform LC Ladder Network Containing Nonlinear Ferroelectric Capacitors," IEEE Trans. Electron Devices, **38** , pp. 767-771 (1991)
5) S. Ibuka, K. Abe, T. Miyazawa, A. Ishii and S. Ishii ,"Fast High-Voltage Pulse Generator with Nonlinear Transmission Line for High Repetition Rate Operation," IEEE Trans. Plasma Science, **25**, pp. 266-271 (1997)

Characterization of pulsed arc discharge between micro-gap in liquid

M. Kanemaru*, R. Saiki, T. Hashimoto, S. Ibuka, S. Ishii

Department of Electrical and Electronic Engineering, Tokyo Institute of Technology
2-12-1, O-okayama, Meguro-ku, Tokyo, Japan

ABSTRACT

The evolution of pulsed arc discharges between the micro-gap with a copper wire and a tungsten plate electrode in liquid was examined for the application to the electrical discharge machining (EDM). Discharge process in EDMs was related to the physics of the pulsed micro-arc discharges in liquid. Spatial and temporal macroscopic behavior of the discharges was observed using a fast ICCD camera and shadowgraph technique. We examined the development of the discharge powered by a capacitor and the micro-arc channel in water using the EDM power supply in water. The machining crater with the diameter of 120μm and the depth of 10μm was obtained.

(key words : pulsed micro-arc, copper wire, electrical discharge machining, liquid)

Ⅰ. Introduction

A variety of methods to generate microplasmas have been proposed and examined experimentally. Technical investigation on working gases, electrode structures, and input power enable us to generate glow microdischarges at atmospheric pressure [1-3]. They are commonly used for applications. On the other hand, micro-arc discharges, for which the current density is higher and the gas temperature is almost equal to the electron temperature, are paid less attention so far. Some examples of the micro-arc with the gap spacing of 10-1000 μm are micro-joining technique in welding equipment and metal-wire bonding technique for manufacturing of semiconductor devices [4].

The pulsed micro-arc discharge in liquid involves complex physical phenomena such as heating of electrode surface, streamer formation, creation initial electrons, and electron transfer between metal and liquid. Characteristics of the micro-arc discharges in liquid are different from those of conventional arc discharges. They are expected to be highly reactive in comparison with that in gas, because they are composed of species generated from metals and liquids.

Electric discharge machinings (EDMs) use the pulsed micro-arc discharges between micro gaps in liquids [5]. The EDM was developed by Russian scientists Boris and Natalya Lazarenko in 1943. Even after 65 years from the development of EDMs as erosion processes, the machining mechanism in the small gap in liquid is not yet fully understood [6]. The technical aspects of machining speed and accuracy, and smoothness of the workpiece surface have been mostly achieved with improvements by employing robotics, automatization, process control and high-performance power supply. In this paper,

we characterize pulsed micro-arc discharges in liquid and examine the eroding processes in the EDM process.

Ⅱ. Experimental apparatus

A schematic of the experimental setup for the micro-arc discharge with a copper wire electrode in liquid, which has a similarity to the electrical discharge machining, is depicted in Fig.1. The copper wire of 100μm in diameter was placed above a tungsten plate electrode of 1×1cm in water. The gap length was 5-250μm. To obtain a reference surface position for the adjustment of gap length, the electrical contact between the copper wire and the tungsten plate was confirmed by detecting a short-circuiting current, which was limited to less than 2-4 microamperes using a low-voltage dc power supply. The wire electrode system was mounted on a piezoelectric stage with the minimum displacement of 20nm, which was adjusted by a stepping motor.

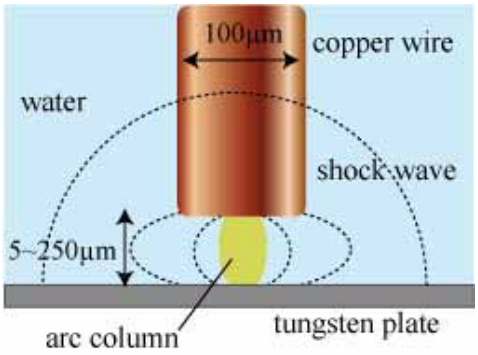

Fig. 1 Experimental setup.

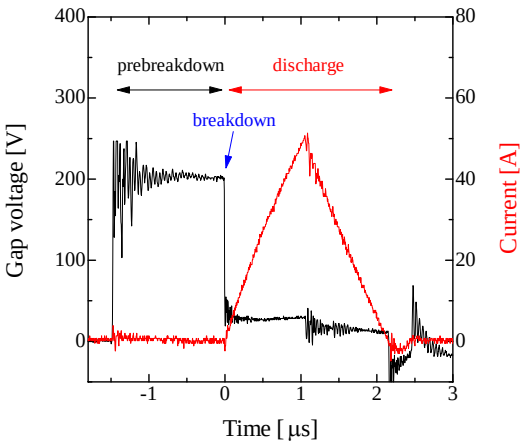

Fig. 2 Gap voltage and current waveforms using EDM power supply.

Fig. 2 shows the current-voltage waveforms of the discharge powered by an EDM power supply, in which the discharge currents are controlled to have a triangular waveform. There is a time lag between the electrical breakdown and the rise of pulsed voltage. During this period, the discharge develops from the wire electrode to the counter metal electrode. After that, an arc column is formed and expands in radial direction due to joule heating.

A fast high-voltage pulse was applied to the micro gap to examine the breakdown processes in liquid. The pulsed voltage was generated by discharging a capacitor of 200pF charged to 7kV with a stored energy of 4.9mJ. Temporal development of the breakdown was observed using a laser shadowgraph method, in which the second-harmonic wavelength of 532nm of a Nd:YAG laser with a pulsewidth of 6ns was used. The visible light emission during the discharge powered by the EDM power supply was observed with a PIN photodiode and a fast ICCD camera. The crater on the surface of tungsten electrode created by the micro-arc discharge was observed using a scanning electron microscope (SEM).

Ⅲ. Results and discussion

1. Electrical breakdown in water

Pulsed micro-arc discharges using the copper wire electrode with a gap separation of 200μm were operated in water. Temporal change of the gap voltage was observed typically as shown in Fig.3 for an applied voltage of 7kV. The discharges developed with the time lag of 2-4μs after the voltage was applied. The time lag depends on gap separations, smoothness of the electrode surface, and applied voltages. There is a pre-breakdown phase prior to the breakdown [7]. In gas discharges, the discharge time lags consist of two parts, namely, a statistical time lag for the beginning of electron avalanche and a formative time lag for the formation of spark discharge developed through electron avalanche processes. In water, however, the development of spark discharge is different from that in gases for several points. Electrons are easily lost in water. Consequently, the electron avalanche can not develop. When the applied voltage was 7kV, the time lag was, on average, 3μs for the gap separation of 200μm.

The discharge time lags were characterized using the Laue-plot method in order to separate them into the statistical time lag and the formative time lag. The Laue-plot depicted in Fig 4 shows the relation between n/N and the discharge time lag, t as

$$\frac{n}{N} = \exp(-\lambda_L t) \quad .$$

Where N is the number of discharges, n is the number of discharges whose time lags are larger than the discharge time lag of t, and λ is the generation ratio of initial electrons per unit time. The data points were obtained in thirty shots for the same gap separation. Fig. 5 shows the statistical time lags and the formative time lags for the gap separation of 50-250μm. Both the time lags increase with increasing the gap separation.

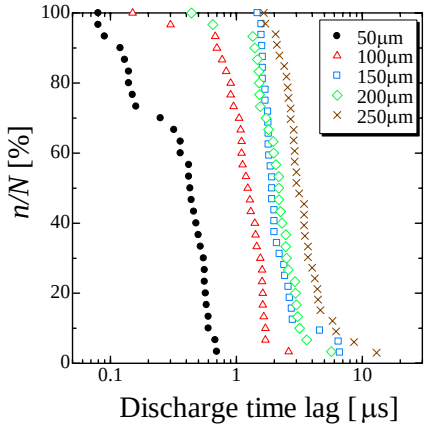

Fig. 4 Discharge time lag at different gap distance.

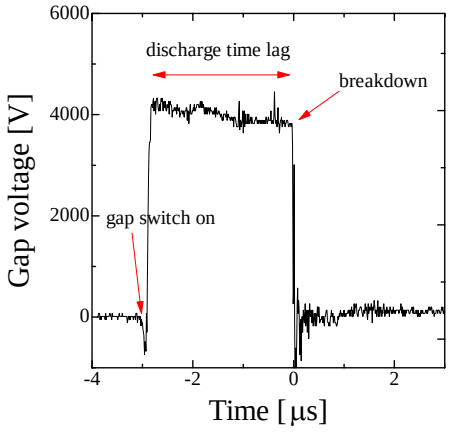

Fig. 3 Gap voltage using a capacitor of 200pF charged to 7kV in water.

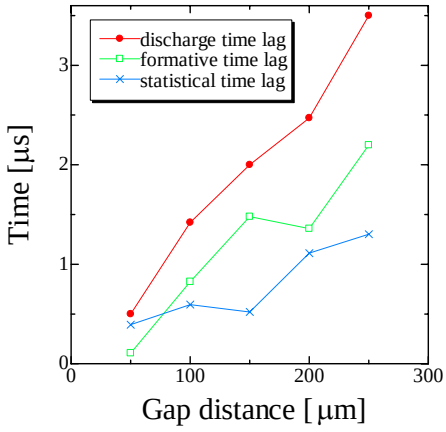

Fig. 5 Discharge time lags depend on the gap distance.

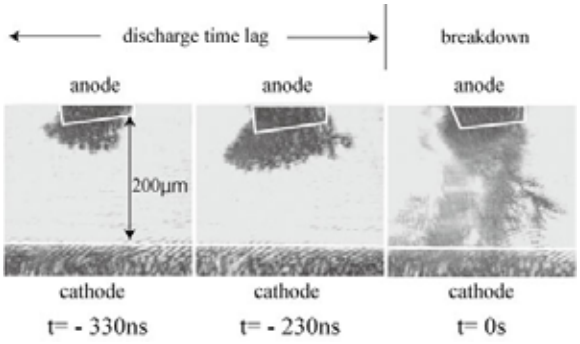

Fig. 6 Images obtained using the laser shadowgraph method.

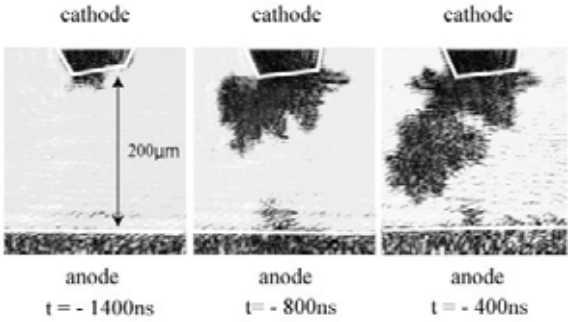

Fig. 7 Images obtained using the laser shadowgraph method. Electrode polarity is reversed.

The temporal evolution of the discharge with the applied voltage of 7kV was observed using the laser shadowgraph method as shown in Fig. 6. Each image was taken for different discharges. The electrical breakdown took place at the copper-wire anode surface, where the electric field was so high. The discharge development with tree like structures, which appear often in the discharges with a needle-to-plate electrode system in liquid, are not observed. It was reported that pre-existing microbubbles play a role in the electrical breakdown in liquids. The possibility of microscopic gas bubbles in liquids is discussed by Bunkin and Bunkin [8]. When the electrode polarity was reversed with same applied voltage, similar images for the temporal development were obtained as shown in Fig. 7. The discharge develops from the wire cathode. In the case

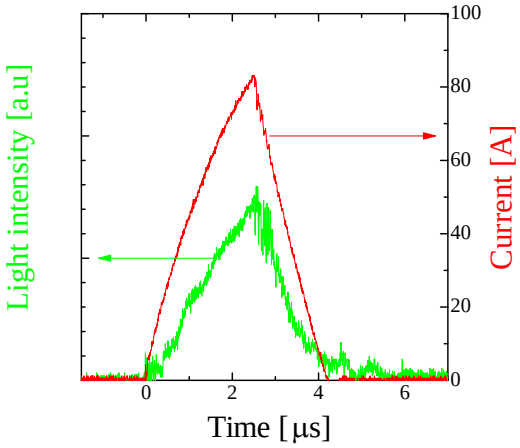

Fig. 8 Temporal change of light intensity and current.

of lower applied voltage, the discharge disappeared on the way before reaching the opposing electrode. Moreover, anything was changeless in the cathode.

2. Pulsed micordischarge in water

The microdischarge developed toward the tungsten plate cathode. A micro-arc channel bridged between the electrodes at t=0. Afterwards, the cylindrical arc channel expanded in the radial direction. Shock waves evolved from the surface of channel and propagated into surrounding water. The light intensity emitted during the discharge time lag phase was so weak that the visible light images could not observed even using the fast ICCD camera. During the discharge phase, however, the optical observation using a PIN diode or the fast ICCD camera was possible. Fig. 8 is the temporal change of the discharge current, of which peak is 83A and pulse width is 4.2μs, and the light intensity emitted from the discharge. The rise and the fall times are 33.2A/μs and 48.8A/μs, respectively. The discharge currents with triangular waveforms are commonly used in the EDMs. The temporal change of the light intensity, whose peak appears at the peak of the current, is similar to that of the current. The light

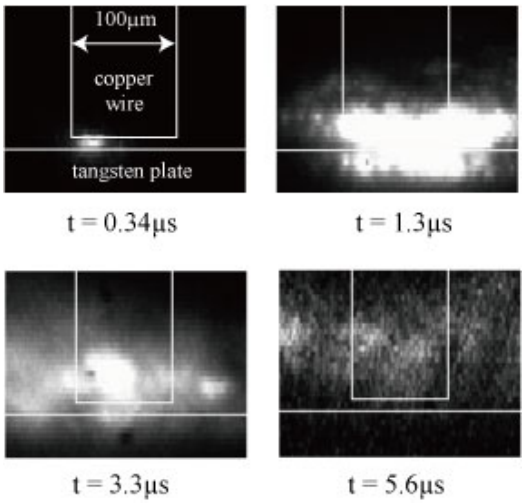

Fig. 9 Snapshots of the discharge taken with the ICCD camera.

increases as the temperature of the discharge volume increases due to joule heating by the current. The light signal with a small amplitude lasted for approximately two microsecond after the current became zero.

Visible light photographs of the discharges taken using the fast ICCD camera with an exposure time of 10ns are shown in Fig. 9. Each photograph was taken for different discharges. The weak light emission appears near the edge of the electrodes at 0.34μs. Exploding bright emission develops between electrodes at 1.3μs. The light intensity of photographs increased with increasing the current. There appeared uniformly distributed weak light spots at 5.6μs, when the current already stopped to flow. The light emission is supposed to be from bubbles generated in heated water.

Micro-craters created at the surface of the tungsten-plate cathode by discharges were analyzed using a scanning electron microscope. Fig. 9 is an SEM photograph of the crater created by one shot of the discharge with the peak current of 88A and the pulse width of 4.1μs. The diameter and the depth of

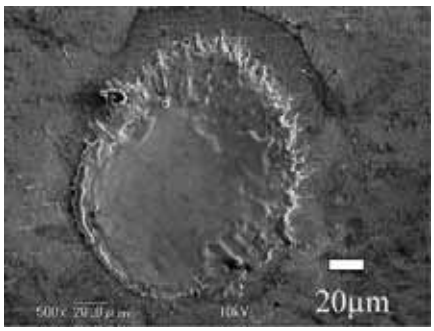

Fig. 10 SEM photograph of the micro-crater in the discharge by EDM power supply.

the crater are 120μm and 10μm, respectively. The crater's edge swelled up because the discharge electrode region was melted.

Ⅳ. Conclusion

Pulsed arc discharges between the micro-gap in liquid, which develop in the erosion processes of EDMs, were examined using the electrical and optical measurements. When the pulsed square-wave voltage was applied in liquid, the discharge took place with the time lag of 2-4 μs at the gap separation of 200 μm. The time lags depend on the gap separation. The electrical breakdown occurred at the surface of the copper anode wire, where the electric field concentrated. When the electrode polarity was reversed, the discharge developed similarly. The visible light intensity emitted from the micro-arc changed with the triangular waveform, which was similar to that of the current. The machining crater with the diameter of 120 μm and the depth of 10 μm was obtained. The detailed understandings of pulsed micro-arc discharges in water make the highly functional EDM possible.

Acknowledgments

This work was supported by a Grant-in-Aid for Scientific Research from the Ministry of Education, Culture, Sports, Science and Technology: Scientific Research on Priority Areas.

References

[1] Takuma Yokoyama, Shuhei Hamada, Shinji Ibuka, Koichi Yasuoka and Shozo Ishii, “Atomospheric dc discharges with miniature gas flow as microplasma generation method”, J. Phys. D: Appl. Phys, Vol.38, pp.1684-1689 (2005).

[2] David Staack, Bakhtier Farouk, Alexander F. Gutsol and Alexander Fridman, “Spatially Resolved Temperature Measurements of Atmospheric-Pressure Normal Glow Microplasmas in Air”, IEEE Transactions on Plasma Science, Vol.35, No.5, pp.1448-1455 (2005).

[3] K. H. Becker, K. H. Schoenbach and J. G. Eden, “Microplasmas and applications“, Journal of Physics D : Applied Physics, Vol.39, No.3, pp.R55-R70 (2006).

[4] Y. Hirata, M. Fukushima, T. Sano, K. Ozaki and T. Ohji, “Micro-arc discharge phenomena”, Vacuum, Vol.59, pp.142-151 (2000).

[5] Fuzhu Han, Li Chen, Dingwen Yu and Xiaoguang Zhou, “Basic study on pulse generator for micro-EDM“, International Journal of Advanced Manufacturing Technology, Vol.33, pp.474-479 (2007).

[6] Bernd M. Schumacher, “After 60 years of EDM the discharge process remains still disputed”, Journal of Materials Processing Technology, Vol.149, pp.376-381 (2004).

[7] Michael Butcher, Andreas A. Neuber, Michael D. Cevallos, James C. Dickens and Hermann Krompholz, “Conduction and Breakdown Mechanisms in Transformer Oil”, IEEE Transactions of Plasma Science, Vol.34, No.2, pp.467-475 (2006).

[8] N. F. Bunkin and F. V. Bunkin, “Bubbstons : stable microscopic gas bubbles in very dilute electrolytic solutions”, Sov. Phys. JETP, Vol.74, pp.271-278 (1992).

New applied study that uses high-speed and low impedance pulse power technology

A.Nishida[1], H.Yoneda[2, 4], K.Oka[2], R.Kodama[1,3,4]

1) Institute of Laser Engineering, Osaka University, 2-6 Yamada-oka, Suita-city, Osaka 565-0871, Japan
2) Institute for Laser Science, University of Electro-communications, 1-5-1 Chofugaoka, Chofu-city, Tokyo, 182-8585, Japan
3) Institute of Laser Engineering, Osaka University, 2-1 Yamada-oka, Suita-city, Osaka 565-0871, Japan
4) Japan Science and Technology CREST

ABSTRACT

We build up high-speed and low impedance micro pulse power system in high power laser plasma experiments to boost the return current in low temperature plasmas, resulting in efficient guiding of energetic electrons. We realized the high speed heating that considered the conductivity of the worm dens matter state. The micro pulse power inject sub TW/cm^2 in a carbon wire before that changes the state. The preparation of the high energy density guiding experiment was complicated.

I. Introduction

With the recent significant progress in laser technology, laser beams are now available that can routinely be focused to intensities approaching >10^{20} W/cm^2. Such high-intensity lasers enable us to access the region of materials having a high-energy density, opening up opportunities for applications in many areas, laboratory astrophysics[1)] and high-density nuclear science[2)], including laser fusion[3)] and so on. Such research relies on the efficient generation of enormous numbers of high-energy charged particles. For example, the energy conversion efficiency from the laser beam to the inwardly directed fast electron beam was indicated between 20 – 40 % at laser intensities on target of 10^{18} W/cm^2- 10^{19} W/cm^2 [4), 5)] and could increase with laser intensity. Laser–matter interactions can create pulses of MeV electrons[4),- 6)] with current densities as large as 10^{12} A/cm^2. However, the divergence of these particle beams[7)] usually reduces the current density to a few times 10^6A/cm^2 at distances of the order of centimetres from the source. Such electron beams propagating in plasmas has the current of much higher than the Alfvén limit[8)] which is defined as the critical current in vacuum, giving $17\gamma\beta$ kA, where $\gamma = 1/(1-(v/c)^2)^{1/2}$ is relativistic scaling factor and $\beta = v/c$, v is the electron velocity and c is the speed of light. At this limit, the self-generated magnetic field makes the Larmor radius of electron orbits in the magnetic field smaller than the beam diameter and stops the beam propagation. Therefore, the current excess the Alfvén limit cannot propagate in the vacuum. On the other hand, in plasmas, background electrons flow backward instantaneously (return current) and compensate the fast electron current almost perfectly because of their high conductivity. In this way, enormous current far excess of Alfvén limit can propagate in plasmas. It should be also noted that plasmas are free from the damage problems which usually solid has, since plasmas are already ionized, thus accept much higher current density. The laser induced high temperature plasma thus can be regarded as an appropriate media for high energy density electron transport. Thus, the conductivity is very important parameter for high energy density electron propagation in plasmas. Recently, we have a novel tool of transient high energy density plasmas to directly control the intense light and high density of energy particles, which we called a plasma photonic device[9)].One of the functions of the devices is control of high density MeV

electrons generated by ultra-intense light taking account of return current in high density plasmas, resulting in an extremely high energy density plasma state. The electron energy density for the cone–wire target can be higher than that for the simple planar target by a factor of about 20–30, that is, 2–3 times higher with the hollow cone and 10 times higher with the wire. This is explained to occur by (1) the rapid heating of the carbon fibre into a plasma fibre, (2) the conduction of the fast electrons through this ‘‘plasma fibre,’’ and(3) the guiding of these electrons by the magnetic and electric fields induced at the fibre edge by their own transport. High temperature plasmas are good conductors to propagate the return current and the energetic electrons follow the conductors.

We expect that they could be used in many future applications because of the control of the high energy-density state allowed by delivery of the laser energy and shaping of the target. Some examples are: point sources of ultra-intense pulse radiation for medical and material science applications; higher energy-density plasma with a higher field for laboratory astrophysics; isochoric heating for precise estimation of equations of state; higher temperature and longer, yet finer plasma for a harder X-ray laser amplification medium[10] and high-density MeV electron guiding for an ultra-compact free electron laser.

Energy PW lasers can create high density energetic electrons with a large amount of the total energy, resulting in control of the energetic electrons with self generated high density and high temperature plasmas. Recently, it is easy to generate high density energetic electrons with ultra-intense laser in table top size. This laser is very short pulses in the range of 20-50fs have been achieved. The table top lasers can generate energetic electrons but be not high temperature conditions to be a good conductor. Here, we have proposed introducing a micro pulse power technology in high power laser plasma experiments to boost the return current in low temperature plasmas, resulting in efficient guiding of energetic electrons. High current pulse power generators with a rise time of nano-sec, which is switched do by a pulse laser trigger system, is developed as the booster of the return current in the cone-wire device to guide the energetic electrons.

When we assumed that 5% of the energy of the ultra-intense laser (Energy:400mJ, Pulse length:40fs) were converted into a high energetic electrons and propagate the plasma fibre is 1%, a large current of 100 kA/MeV transient the wire. Therefore, the circuit causes the dielectric breakdown when it tries to throw the high current from opposite direction like return current that corresponds to the high energetic electrons. So, we proposed that a micro pulse power system which generates large current will assist heating the wire before laser shot. The pulse power technologies have the feature which can efficiently input the energy in minute space so that it may be represented by Z pinch.

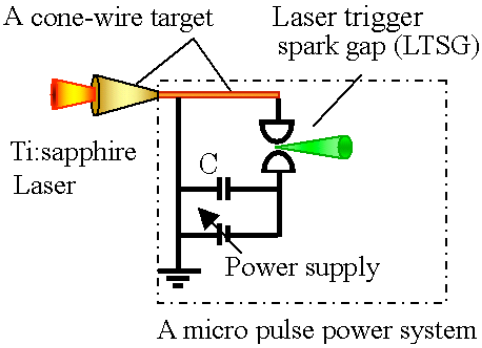

Figure 1. Electron guiding with a micro pulse power

The general sequences of high energetic electrons propagate in the fine fibre to use the micro-pulse power technology can be subdivided as follows. First high current which generated by the micro pulse power technology can increase temperature by the energy deposited in the wire during the Ohmic heating process. The conductivity of the wire increases with increasing temperature (hot conductor). Second Ultra-intense laser shot into the cone-wire target after the wire preheating finished. The energetic electrons which are generated by laser matter interactions propagate the preheated wire. At this time, return current flows the surface of the wire in the opposite direction to high energetic electrons. Return current more heating the wire and become the fibre plasma[11]. Return current flows smoothly by having heated with pulse power, resulting in efficiently guiding of energetic electrons. In addition, electric potential works between the wire so that a high density electrons are easy to propagate and it is keep flowing to high

current in the wire with the micro pulse power technology, the high density electrons are efficiently flow by these effects. Propagation of the high energetic electrons outside the wire induces a strong radial electric field surrounding the fibre like plasmas, and acts to pinch the high energetic electrons along the fibre length.

Now, we are focusing a carbon wire-cone target which used previous electron guiding experiment. Warm dense matter[12], the state of matter between solids and plasmas, which is broadly defined as the parameter space with densities 1 - 10 times of solid density, and temperatures ranging from 0.1 eV to 100 eV. In all previous exploding wire experiments only metallic or metal-like wires were vaporized. The reason for this is the good electrical conductivity of metals. The resulting fast energy input leads to a well reproducible and homogeneous plasma. On the other hand the conductivity of carbon is three orders of magnitude smaller than that of metals. In contrast to metals, the conductivity of carbon increases with increasing temperature. Therefore, developing a preheating system enabled us to use this effect for producing carbon plasmas with the same homogeneity and reproducibility as it is seen for metal plasmas. The conductivity of carbon compared to that of Al from room temperature up to 40 eV. The electric conductivity of the carbon is simple to change with temperature and expansion velocity is more slowly than metals. The carbon wire becomes almost the same electric conductivity as the metal about 5eV ($1.02\times10^5/\Omega^{-1}\cdot m^{-1}$) [13]. The conductivity of a carbon increase with temperature associate with increasing number of free electrons. On the other hand, for example, the conductivity of aluminum is the lowest state from 10eV to 40eV [14] and conductivities do not change as simply as the carbons with the temperature. At high temperatures, a carbon becomes even more conductive than a aluminum. Therefore, it is easy to treat the carbon than other materials in this experiment. We chose carbon because it is simple to describe element, which is solid at room temperature and also easy to handle. And also expansion velocity is very slow than metals.

Ⅱ. Laser trigger spark gap (LTSG)

The laser triggered spark gap was able to switch high currents and high voltages with nanosecond precision. The laser did not only cause the breakdown to occur faster than spontaneous breakdown, it seemed also possible to use the laser to trigger an under-volted spark gap to switch voltages below the self-breakdown voltage of the gap. In many different laboratories different spark gap geometries and positions and energies of the laser focus were investigated and all kinds of gases and liquids were inserted in the spark gaps. Later the spark gaps became more complicated in structure and spark gaps were developed that were able to switch Megavolts. When new lasers were developed (CO_2, UV, Nd:YAG, Ti:Sapphire etc.), they were also tried in spark gaps [15) - 17)] . Detailed studies of the switching plasma were made[18) - 20)] in order to get a better understanding of the switching process. We made a LTSG which has high-speed and low impedance to heat a carbon wire. The switch is triggered KrF laser that maximum energy is 2J, but we didn't measured. This beam was divided into four beams and irradiates four electrodes at the same time.

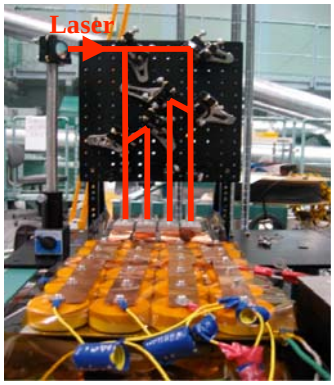

Figure 2. Laser trigger spark gap

The voltage rise time depend on inductance and capacitance. But capacity has already been decided depending on the amount of the current to make a plasma fibre.

Figure 3 shows that channel number depended on inductance. If we increases channel number, circuit inductance is decreases but after 4 channels circuit inductance was saturated. Because other parts (capacitor bank etc.) of this switch has more high inductance than switching point. The four channels LTSG reduce the whole switch inductance more than 67%, therefore rise time

is faster than precious one channel LTSG. In addition low impedance switch create a high current because the electrical circuit inductance was decrees.

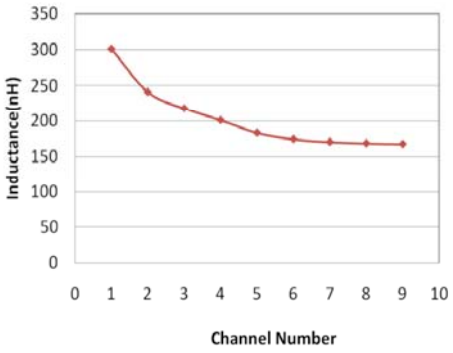

Figure 3. The inductance of LTSG reduces with channel number

Ⅲ. Experimental Setup

An electrical diagram of the experimental setup is presented as Fig. 3. A pulse generator with 4 lines low inductive capacitors 63.4nF connected in parallel are charging voltage of 25kV closing a low inductive LTSG stored energy of 19.8J provides the electrical pulse to drive the wire heat. The high-voltage source charged a coaxial transmission line through a 10 MΩ ceramic high-voltage resistor. The spark gap was situated at the end of the transmission line. 4 lines of 5m length, 0.91Ω low impedance coaxial wave guide line delivers the electrical pulse from the LTSG to the wire. The thin (5μm diameter and 1,4,6mm long) carbon wires were placed in the cathode-anode gap in the coaxial target unit in atmosphere. The size of the wire was small enough to guarantee homogeneous vaporization without impairment due to the skin effect. On the other hand, due to high electric field surrounding the wire at the beginning, the generation of a peripheral discharge could be induced if the diameter of the wire was too small. The wire edge was sandwiched indium (50μm thickness and 100μm square size). The anode-ground voltage was measured with a high voltage probe at the connecting point of waveguide line and wire target holder and this electrical wave form ware captured by oscilloscope.

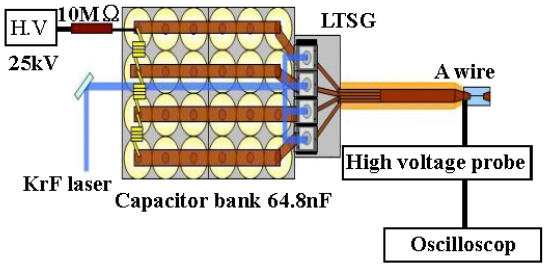

Figure 4. Experimental Setup

Ⅳ. Experimental results

Figure 5 shows each length a carbon wire discharge in same condition. The voltage rise time depends on length of the wire and changes by resistance and the inductance of the wire. In both cases the voltage goes almost same time, and collapses time in 15-20ns. Now we are discussing about 1mm length carbon wire for using electron guiding experiment in the future.

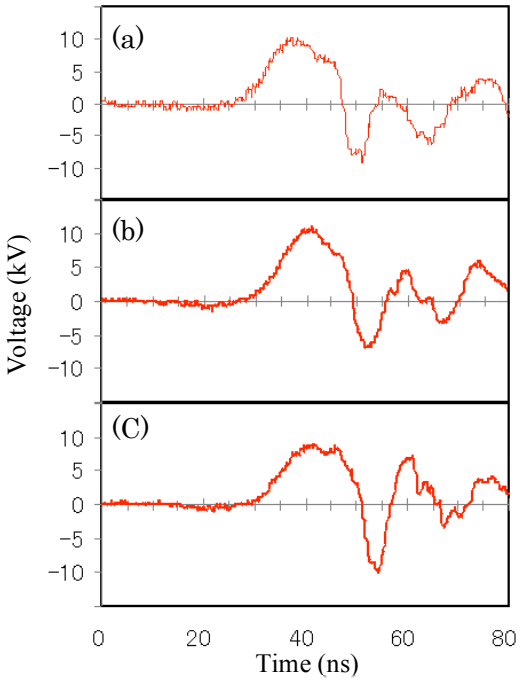

Figure 5. The voltage waveform

The voltage of waveform of wire (diameter is 5 μ m). The Length is different. (a)1mm, (b)4mm, (c)6mm

Figure 5(a) shows t voltage goes to a maximum about 10 kV in 7 ns and drops almost to zero during the next 13ns.After voltage breakdown, the voltage same as for

short-circuit load. The voltage collapse is related to the ionization of the ambient vapor and fast reduction of cathode- anode resistance due to rapid expansion of the corona plasma shell. In this time we didn't measure the current waveform or light emission, but we guess this timing more current values rapidly increased and pass through the high current. This means most energy input the wire in this timing and uses the experiment for high energy density electrons guiding.

We measured a 1mm length and diameter 5 μm carbon wire resistance before connecting the electrical circuit. The carbon wire resistance is 4.2kΩ. When the wire is heated in the state of the solid, we assumed the wire has hardly expanded. It is understood that there is energy of sub t sub TW/cm^2 the injection from Ohm's law if it is assumed that the resistance of the carbon doesn't change while it is being heated.

V. Conclusion

We build up high-speed and low impedance micro pulse power system in high power laser plasma experiments to boost the return current in low temperature plasmas, resulting in efficient guiding of energetic electrons. We realized the high speed heating that considered the conductivity of the warm dens matter state. We checked a carbon wire which length is 1mm, diameter is 5 μm and resistance 4.2kΩ discharge with the micro pulse power system. The rise time of voltage reached in 7ns and changes voltage wave form next 12ns. The wire is in a solid state the energy injected sub TW/cm^2 between that time. Therefore, this was able to achieve the high energy density state that could be created by the table top laser by the micro pulse power and the preparation of the high energy density guiding experiment was complicated. We will try high energy density electrons controlled by ultra intense laser coupled with a micro pulse power discharged fiber in the near future.

Acknowledgments

This research is supported by Japan Science and Technology CREST and JSPS.

References

1) Remington, B. A., Arnet, D., Drake, R. P. & Takabe, H. "Modeling astrophysical phenomena in the laboratory with intense lasers", Science 284, 1488–1493 (1999).
2) Ledingham, K.W. D.,McKenna, P. & Singhal, R. P. "Applications for nuclear phenomena generated by ultra-intense lasers", Science 300, 1107–1111 (2003).
3) Tabak, M. et al. "Ignition and high gain with ultra powerful lasers", Phys. Plasmas 1, 1626–1634 (1994).
4) Wharton, K.B. ,Hatchett, et al. "Experimental measurements of hot electrons generated by ultraintense (>10^{19}W/cm^2) laser-plasma interactions on solid-density targets", Phys. Rev. Lett.,81, 822-825 (1998)
5) Kodama, R., Mima, K. et al. "Fast ignitor research at the Institute of Laser Engineering, Osaka University", Phys. Plasmas 8, 2268-2274 (2001)
6) Key, M. H. et al. "Hot electron production and heating by hot electrons in fast ignitor research", Phys.Plasmas 5, 1966–1972 (1998).
7) Kodama, R. et al. "Fast heating of ultrahigh-density plasma as a step towards laser fusion ignition", Nature 412, 798–802 (2001)
8) Alfvén, H. "On the motion of cosmic rays in interstellar space", Phys. Rev., 55, 425-429 (1939)
9) R. Kodama, Y. Sentokunet al.," Plasma devices to guide and collimate a high density of MeV electrons", Nature, 432, 1005-1008 (2004)
10) Fill, E. et al. "in X-ray Lasers 1998" , (eds Kato, Y., Takuma, H. & Daido, H.) 301–308 (Inst. Phys. Conf. Ser. No. 159, IOP Publishing, Bristol, 1999).
11) J.S.GREEN,K.L.LANCASTER et al.,"Surface heating of wire plasmas using laser-irradiated cone geometries", Nature phsy 3, 853-856(2007)
12) Koenig, M., Benuzzi-Mounaix et al. "Progress in the study of warm dense matter", Plasma Phys. Control. Fusion, 47, B441–B449. (2005)
13) J.Haun et al., "Electrical conductivity of nonideal carbon and zinc plasmas : Experimental and theoretical results" Phys. Rev. Lett.E 65, 046407 (2002)
14) Arvinder S. Sandhu et al.,"Time resolved evolution of structural, electrical,and thermal properties of copper irradiated by an intense ultra short laser pulse" J. Appl. Phy 97,023526(2005)
15) J.R. Woodworth, P.J. Hargis et al, "Laser trigger of a 500-kV gas- filled switch:A parametric study" Appl. Phys. 56, 1382(1984).
16) L. Ya. Polonskiy, A. Yu. Goltsov and A.V. Morozov, "Fast switching with laser-generated continuous plasma columns" Phys. Plasmas, 3, 2781 (1996))

17) B.M. Luther, L. Furfaro, A. Klix and J.J. Rocca, “Fwmtosecond laser triggering of a sub-100 picosecond jitter high-voltage spark gap” Appl. Phys. Lett., 79, 3248 (2001)
18) R.A. Dougal and P.F. Williams, “Fundamental processes in the laser-triggered electrical breakdown of gasses : Unconventional geometries” J. Phys. D., 17, 903 (1984)
19) W.D. Kimura, M.J. Kushner, E.A. Crawford and S.R. Byron,”Low-inductance capacitive probe for spark gap voltage mesurements” IEEE Trans. Plasma Sci., 14,
246 (1986)
20) R. Najafzadeh, E.E. Bergmann and R.J. Emrich, “Schlieren and interferometric study of a laser triggered air spark in the nanosecond regime” J. Appl. Phys., 62, 2261 (1987)

GENERATION OF TERAHERTZ RADIATION FROM THE GYROTRONS WITH PULSE MAGNETS

M.Glyavin[1] , T.Idehara[2], A.Luchinin[1], T.Saito[2] , I.Ogawa[2], LaAgusu[2]

[1]Institute of Applied Physics, Russian Academy of Sciences, (IAP RAS)
46 Ulyanov St., Nizhny Novgorod 603950, Russia
[2]Research Center for Development of Far-Infrared Region, University of Fukui, (FIR FU)
Bunkyo 3-9-1, Fukui 910-8507, Japan

ABSTRACT

The experimental results of terahertz generation from pulsed magnetic field gyrotrons are presented. The successful excitation of high order second harmonic mode at this frequency band has been demonstrated at the FIR FU. The long pulse (1 millisecond) operation has been obtained at the frequencies up to 1.013 THz. The powerful (1.5 kW) generation at the fundamental harmonic frequency 1.022 THz with 50 microseconds shorts has been realized at the IAP RAS.

I. Introduction

Gyrotrons are known as devices capable of producing coherent powerful electromagnetic radiation at millimeter and submillimeter wavelengths. One of the most important and maybe most promising for today gyrotron investigations is development of terahertz gyrotrons.

Development of compact, simple and reliable sources of coherent sub-terahertz (sub-THz) and terahertz (THz) radiation is important for numerous applications, which include plasma diagnostics [1, 2], electron-spin resonance spectroscopy [3], enhancement of NMR sensitivity using dynamic nuclear polarization [4, 5], standoff detection and imaging of explosives and weapons [6], new medical technology [7], atmospheric monitoring [8], chemical technologies, production of high-purity materials, etc. Gyrotrons are much more compact than powerful free electron lasers because they do not require large accelerators or high-voltage modulators. From the other hand the gyrotrons can realized essentially higher output power comparing with solid state devices.

However, to provide cyclotron resonance between gyrating electrons and fast waves excited in smooth waveguides at THz frequencies near cutoff, high magnetic fields are necessary: in the range of 40 T for the fundamental harmonic interaction at the radiation frequency of 1 THz; at higher harmonics magnetic field decreases inversely proportional to the cyclotron harmonic number. The frequency rise needs operating at high order modes to store the reasonable scale of interaction region. The progress in frequency increasing delay by problem of mode competition at high order harmonic modes operation and impossibility realized non-volatile pulsed coils with strong enough magnetic fields and effective cooling for fundamental harmonic operation. It should be taken into account that typically magnetic field, which can be produced in cryomagnets with a large enough inner bore, do not exceed 20 T. Higher magnetic fields can be realized only with the use of pulsed solenoids.

This paper presented the results of the first successful breakthrough from the magic 1 THz benchmark.

II. Powerful fundamental harmonic short pulse 1THz gyrotron (IAP RAS)

A demountable compact THz gyrotron tube with a pulse magnet has been designed, constructed and tested at IAP RAS. This work is based on the previous results obtained with gyrotrons using pulsed solenoids [9] and on the development of an improved pulsed solenoid, producing magnetic field up to 40 T [10]. Gyrotron

photo is shown in Fig. 1 and block diagram of the experimental facility is shown in Fig. 2.

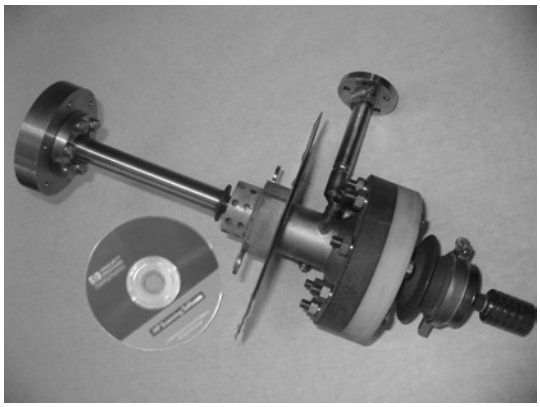

Fig. 1. The gyrotron with the pulse solenoid.

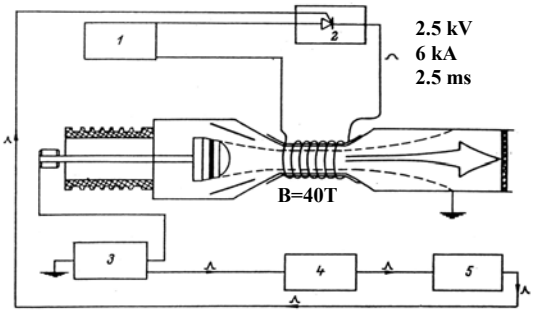

Fig. 2. Block diagram of the experimental facility: 1- capacitor bank 2- thyristor switch, 3- high voltage power supply, 4- delay unit, 5- control unit

The solenoid was made of a composite cable consisting of a 40%Nb-60%Ti alloy mechanically reinforced in an outer copper shell. For reducing ohmic heating and stabilizing the operation, the solenoid was cooled by liquid nitrogen. The cable was wired directly on a thin stainless steel gyrotron body to minimize the coil bore diameter and the energy consumption. Magnetic field was produced in the course of discharge of a bank of capacitors (the storage energy is 5.6 kJ). Due to limitations caused by the pulsed solenoid cooling, the repetition rate was limited by one shot in a minute.

Experimental results were obtained for high frequency operation at the fundamental cyclotron resonance. Detection of microwave power was made by a silicon point contact diode and by the dummy load with sensitivity about 10 mJ in single shot. By varying the magnetic field, a number of various modes with frequencies close to 1 THz and the output power at 1 kW level were excited in a step-tunable manner. At the magnetic field close to 38.5 T, the $TE_{17,4}$ mode was excited at 1.022 THz frequency [11]. The microwave pulse of this mode is shown in Fig. 3. The radiation power averaged over the pulse was 1.5 kW. This power level for a 24 kV, 3 A electron beam corresponds to 2.2% output efficiency. The main reason for a relatively low efficiency is the cavity length which is about two times longer than the optimal one. However, with cavity length increasing, the starting current reduced, that ensures the excitation of the desired mode.

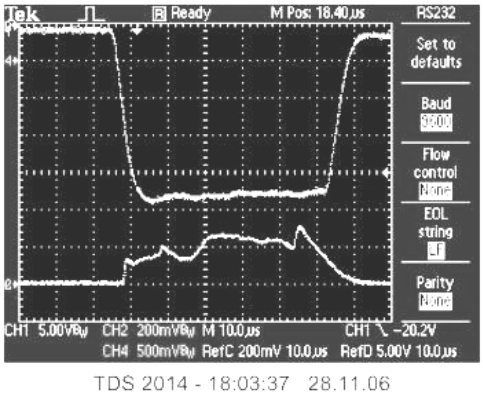

Fig. 3. The $TE_{17,4}$ mode operating pulse. Upper trace – high voltage pulse, lower trace – microwave signal from detector.

To measure the THz frequency in a device operating in single shots the method based on mixing the gyrotron signal with the signal from a millimeter-wave frequency synthesizer [12] have been used. The gyrotron frequency was slightly varied from pulse to pulse and, therefore, to get the intermediate frequency (IF) in a relatively narrow frequency band of the IF amplifier the frequency of the backward-wave oscillator (BWO) was swiped during the microwave pulse several times. Then, by gradually narrowing the bandwidth of BWO frequency modulation it was possible to determine the radiation with the precision determined by the bandwidth of the IF amplifier. The measured frequency 1.022 THz was close to the cyclotron frequency 1.024 THz calculated from the magnetic field value.

So, in the experiment with gyrotron operating in pulsed magnetic field, coherent THz radiation with the microwave power of 1.5 kW and the microwave energy 75 mJ in single shots was obtained for the first time. There are some plans to developed similar gyrotrons with improved solenoids allow of higher repetition rate operation [13], but the effective cooling in such conditions looks problematic.

III. Long-pulse operation of the 1THz second harmonic gyrotron (FIR FU)

Long pulse operation up to 1 ms of a high frequency gyrotron with a pulse magnet has been successfully carried out in a frequency range including 1 THz at FIR FU [14, 15, 16]. The demountable gyrotron tube with high cavity Q-factor and an ice protected pulse magnet with maximum field intensity 20.5 T was developed for second harmonic 1THz generation (Fig.4). The block diagram of the whole system is similar with Fig. 2. The coil with inner diameter 43 mm was made by the copper wire. The coil is inserted in stainless steel cylinder with wall thickness 22.4 mm. Water with alumina powder surrounds the coil and fills the clearance between the coil and a stainless steel cylinder. The whole magnet system is installed in a cryostat and cooled down by liquid nitrogen. Then, water with alumina powder is frozen and fixes the solenoid coil tightly in order to protect the coil from expanding in radial direction. The pulse magnet is powered by a capacitor bank with the maximum stored energy about 300 kJ. The coil current pulse width is from 3 to 5 ms and the gyrotron high voltage pulse width is typically 1 ms.

Fig. 4. The second harmonic gyrotron with the pulse solenoid.

In the experiments, the timing of an electron beam pulse injection is adjusted at the top of the magnetic field pulse, where the variation of field intensity is negligible. The operation cavity modes seem to be $TE_{1,12}$ and $TE_{4,12}$ at the second harmonics with frequencies 903 GHz and 1.013 GHz, respectively. The microwave pulse duration up to 1 ms at 0.903 THz and 0.5 ms at 1.013 THz was observed (Fig.5).

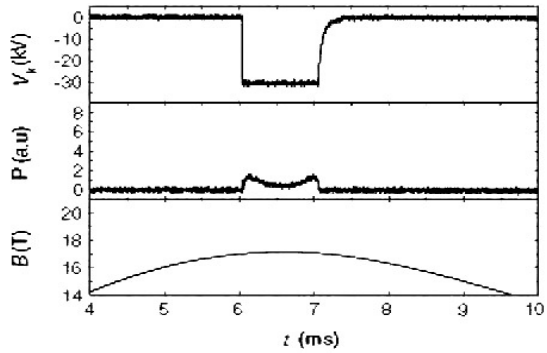

Fig. 5. The typical oscilloscope trace during long pulse operation. Upper trace: high voltage pulse; middle trace: output radiation power; lower trace: pulse magnet intensity.

All frequencies estimated from the field intensities where the power peak appears are plotted in Fig. 6. There are many cavity modes (identified from the estimated frequencies) excited at both fundamental and second harmonic operations. These radiations observed in the frequency range from 0.4 THz to 1 THz are useful for their applications to high power THz technologies. During some shorts than high voltage pulse corresponded to fall down magnetic field the excitation several modes with step by step frequency tuning was observed.

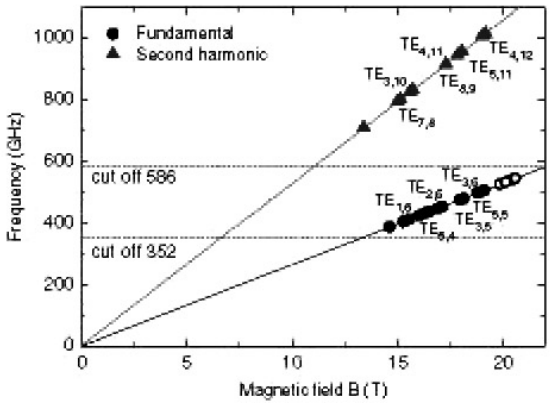

Fig. 6. All frequencies observed at fundamental (circles) and second (triangles) during tube experimental test by variation of magnetic field and modes identified from the expected frequency for 1 THz pulse magnetic field gyrotron.

IV. Summary

The pulse magnetic field gyrotrons have achieved higher than 1THz frequency with 1.5kW

output power level at fundamental harmonic and long pulse operation at the second harmonic. In the latter case, the relatively low magnetic field about 20T give optimism for CW tube development based on modern superconducting magnets.

Acknowledgments

The report was carried out under nice collaboration among research centers in Japan (Fukui, FIR FU) and Russia (Nizhny Novgorod, IAP RAS). This work is partially supported by the common Grant of Japan Society for the Promotion of Science and Russian Foundation for Basic Research (Project No. 06-02-91176), by Grant-in-Aid from the Ministry of Education, Science and Culture of Japan and by the Civilian Research and Development Foundation Grant No. RUPI-2688-NN-05

References

1) P. Woskoboinikow, D.R. Cohn and R. J. Temkin, "Application of advanced millimeter/far-infrared sources to collective Thomson scattering plasma diagnostics", *Int. J. Infrared and Millimeter Waves*, **4**, 2, 205-229, (1983)
2) T. Idehara, S. Mitsudo, M. Ui, I. Ogawa, M. Sato, K. Kawahata, "Development of frequency tunable gyrotrons in millimeter to submillimeter wave range for plasma diagnostics", *J. Plasma Fusion Res. Series,* **3**, 407–410 (2000).
3) S. Mitsudo, Aripin, T. Matsuda, T. Kanemaki, and T. Idehara, "High power, frequency tunable, submillimeter wave ESR device using a gyrotron as a radiation source", *Int. J. Infrared and Millimeter Waves,* **21**, 661–676 (2000)
4) V.S. Bajaj, C.T. Farrar, M.K. Hornstein, I. Mastovsky, J. Bryant, K.E. Kreischer, R.J. Temkin, R.G. Griffin, "Dynamic Nuclear Polarization at 9 Tesla Using a Novel 250 GHz Gyrotron Microwave Source", *J. Magn. Resonance*, **160**, 85-90, (2003)
5) La Agusu, T. Idehara, I. Ogawa, T. Saito, T. Kanemaki, H. Takahashi, T. Fujiwara, "Detailed Consideration of Experimental Results of Gyrotron FU CW II Developed as a Radiation Source for DNP-NMR Spectroscopy", *Int. J. Infrared and Millimeter Waves*, **28**, 499-511, (2007)
6) J. F. Federici, F. Huang, A. Bandyopadhyay, A. Sengupta, D. Gary, R. Barat, D. Zimdars, "THz Standoff Detection and Imaging of Explosives and Weapons", *Proc. SPIE,* **5781**, 75, (2005)
7) T. Tatsukawa, A. Doi, M. Teranaka, H. Takashima, F. Goda, T. Idehara, I. Ogawa, T. Kanemaki, S. Nishizawa, "Submillimeter Wave Irradiation of Living Bodies using a Gyrotron and a Catheter", *Jpn. J. Appl. Phys.*, **41**, 8, 5486-5489, (2002)
8) D. L. Woolard, E. R. Brown, M. Pepper, M. Kemp, "Terahertz frequency sensing ... A time of reckoning future applications?", *Proc. IEEE*, **93**, 1722-1743, (2005)
9) V. Flyagin, A. Luchinin, G. Nusinovich, "Submillimeter-wave gyrotrons: Theory and experiments", *Int. J. Infrared and Millimeter Waves*, **4**, 4, 629-637, (1983).
10) A. Luchinin, M. Glyavin, V. Malyshev, Development of a THz gyrotron based high intensity pulse magnet, *Book of abstracts 6 Int. Workshop "Strong Microwaves in Plasmas",* N. Novgorod, Russia, S40, (2005)
11) M. Glyavin, A. Luchinin, G. Golubiatnikov "Generation of 1.5-kW, 1-THz Coherent Radiation from a Gyrotron with a Pulsed Magnetic Field" *Phys. Rev. Lett.,* 100, 015101 (2008)
12) M. Yu. Tretyakov, Yu. K. Kalynov, "Measurements of the radiation Frequency of a Pulsed SubMM-Wave Gyrotron Using Beat-Note Signals with the Harmonics of a Millimeter-Wave Frequency Synthesizer", *Instrum. and Experim. Techniques*, **49**, 5, 661-668, (2006).
13) M. Read, L. Ives, J. Neilson, G. Nusinovich, "Development of a High Power Pulse THz Gyrotron", *IEEE Int. Vacuum Electronics Conf. IVEC '07,* 347-348, (2007).
14) T. Idehara, H. Tsuchiya, O. Watanabe, LaAgusu, S. Mitsudo, "The first experiment of a. THz gyrotron with a pulse magnet", *Int. J. Infrared and Millimeter Waves*, **27**, 3, 319-331, (2006)
15) O.Watanabe, H.Tsuchiya, H.Mori, LaAgusu, I.Ogawa, T.Saito, T.Idehara "Development of a TeraHertz Gyrotron as a Radiation Source", *Plasma and Fusion Research*, 2, S1043 (2007)
16) T. Idehara, T. Saito, H. Mori, H. Tsuchiya, La Agusu, S. Mitsudo "Long Pulse Operation of the THz Gyrotron with a Pulse Magnet", *Int. J. Infrared and Millimeter Waves*, **29**, 2, 131-141, (2008)

FREE ELECTRON MASER WITH ADVANCED BRAGG RESONATOR FOR MILIMETER WAVESOURCE

Mikiko Kawamura, Kousuke Aizawa, Shuhei Odawara, Keiichi Kamada and Naum S. Ginzburg [a)]

Graduate School of Science and Technology, Kanazawa University, Kanazawa, Ishikawa, 920-1192, JAPAN
[a)]Institute of Applied Physics, Russian Academy of Sciences, Nizhny Novgorod, 603600, Russia

ABSTRACT

New scheme of electromagnetic wave source using an electron beam was proposed and designed. Free electron MASER with an advanced Bragg resonator has an advantage of the frequency selectivity to that with the normal Bragg resonator. The radius of the advanced Bragg resonator is decreased at both ends of the Bragg cavity. A electromagnetic wave with quasi-cutoff frequency is trapped in the cavity and couples with the propagating wave. The higher frequency selectivity like gyrotron is expected. An intense relativistic electron beam for advanced Bragg resonator was prepared. The decrease of energy during the pulse duration was improved by a variable shunt register located parallel to the diode.

I. Introduction

Radiation sources in the frequency range of 0.1-10 THz, called THz gap, are strongly expected by many fields of fundamental physics and applications [1]. THz gap lies between the upper frequency of classical electromagnetism (electron tubes) and the lower frequency of quantum electronics (LASER). There are three candidates for THz sources, LASER, large accelerators and electron tubes [2,3]. For practical use, THz source is requested to be compact size, DC operation with output power over 1 W. Laser and large accelerator are successfully used for the THz sources, However, the efficiency of the THz sources using Laser is not so high and the source using large accelerator is inconvenient for the users. Vacuum tube electronics technology is expected to achieve convenient powerful THz sources.

Gyrotoron is the most developed electron tube for THz source. The selectivity of the frequency is excellent because the quasi-cutoff frequency was used. The problem for the Gyrotron for THz source is that the magnetic field over 20 T is necessary to increase the frequency in sub-millimeter range [4]. One of the other candidates of THz source among electron tubes is free electron maser (FEM). Bragg mirror is utilized as mirrors in the optical distributed feedback LASER (Fig.1) [5,6]. Many successful results of narrow band FEM are obtained by using the Bragg mirror in mm waveband [7,8]. However, as the frequency increases, the traditional Bragg mirror loses the selective features over transverse indexes. The mode competition effects are a very severe problem for FEM. We report here the new scheme of the Bragg resonator for higher frequency selectivity at the high frequency range. And preparations of an intense relativistic electron beam for the proof of

principle experiments of the new scheme are described.

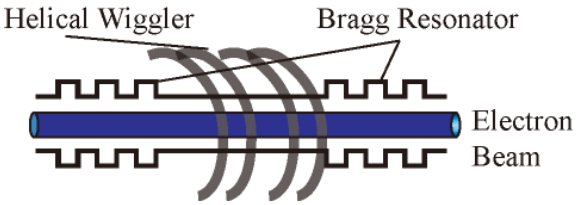

Fig. 1 FEM with the Normal Bragg Resonator

2. Advanced Bragg resonator.

The traditional Bragg mirror was located at the entrance and exit of the tube like mirrors of optical LASER as shown in Fig. 1. Advanced Bragg resonator (ABR) was proposed by Ginzburg[9]. As shown in Fig. 2, ABR is located at the center of the helical wiggler coil. The diameter at both edges of ABR is a little decreased compared with the one at the center part. Due to small variation of the mean radius of the ABR at the boundaries, the cutoff mode is trapped inside the ABR. An injected electron beam interacts with the propagating wave and the latter is coupled with the quasi cutoff mode in the ABR. Interaction between propagating wave and quasi-cutoff mode provides possibility of Doppler frequency upshift and quasi cutoff mode provides possibility of transverse mode selection similar as Gyrotron. So that higher frequency selectivity is realized in the ABR than normal Bragg cavities.

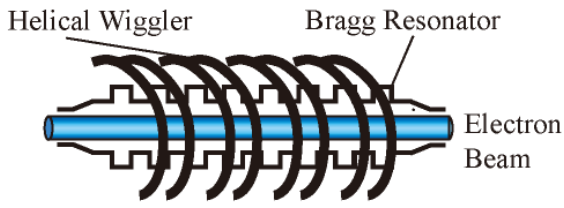

Fig. 2 FEM with the Advamced Bragg Resonator

3. Design of Helical Wiggler Coi

The wiggler coil composed of two helical coils. As currents with opposite direction were propagated through the coils, the axial magnetic field was cancelled and the radial magnetic field was left.

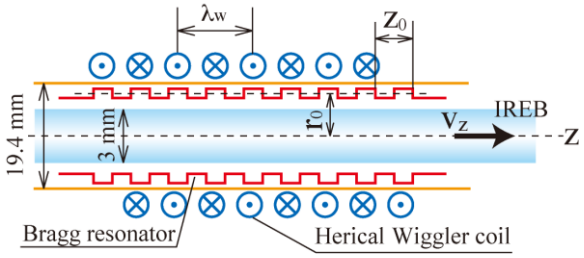

Fig. 3. Helical wiggler coil and Bragg resonator.

We start to design the helical wiggler coil for the radiation with frequency of 40-60 GHz, using an intense relativistic electron beam (IREB) with energy of 700 keV. The radiated wave length λ is expressed with the axial beam velocity v_z and the period of the coil, λ_w as shown in Fig. 3 as below.

$$\lambda = (c - v_z)\lambda_w / v_z \quad ,$$

where c is the speed of light. The λ_w was roughly calculated to be 30-50 mm for our experimental conditions. The strength of the radial magnetic field $|B|$ near the axis is calculated from the equation below.

$$|B| = \frac{\mu_0 I k_w}{\pi}[k_w a K_0(k_w a) + K_1(k_w a)] \quad ,$$

where I is the current, $\lambda_w = 2\pi/k_w$, a is the radius of the coil, K_0 and K_1 are the modified Bessel functions and μ_0 is the permittivity. From experimental conditions, the current required for the $|B|$= 0.1 T should be less than 10 kA. The diameter of the helical wiggler coil was calculated to be 15-30 mm for our experimental conditions as shown in Fig. 4.

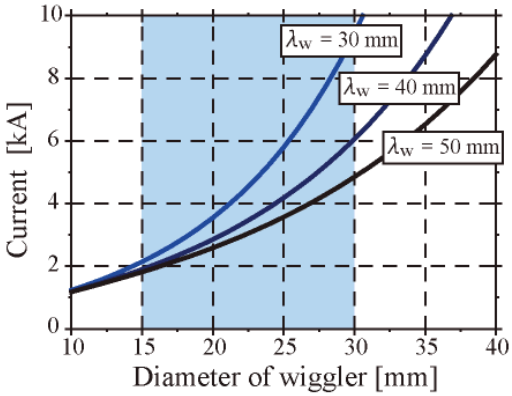

Fig. 4 Diameter of the helical wiggler coil vs the current for strength of the radial magnetic field of 0.1 T.

Following the above estimations, we made a helical wiggler coil as shown in Fig. 5. The period of the coil is 48 mm and the diameter of the coil is 30 mm. The inner diameter of the vacuum vessel is 21 mm. The radial magnetic field of 0.23 T on the axis is expected with the current of 6.2 kA.

Fig. 5. Photos of the helical wiggler coil

4. Design of ABR

At first, the dispersion curves of the beam wiggled by the helical coil and the normal Bragg cavity are calculated. The dispersion relation of the beam passing through helical wiggled magnetic field with wave length of λ_w is described as below.

$$\omega = \left(k + \frac{2\pi}{\lambda_w} \right) v_z,$$

where ω and k are the angular frequency and the wave number, respectively. And that of the TE_{11} mode of the cylindrical waveguide with radius of r_0 was shown in Fig. 6. Two possibilities of the radiated frequency exist in the dispersion relation. To improve the frequency selectivity we looked for the appropriate period of the advanced Bragg resonator using the approximate dispersion relation described below .

$$\omega = c\sqrt{\left(\frac{y_{ij}}{r_0}\right)^2 + \left(k - \frac{2n\pi}{z_0}\right)^2} \quad ,$$

where y_{ij} is j th root of the Bessel function of $J_i(y) = 0$, r_0 is the average radius of the cylindrical Bragg resonator, $n = 0, \pm 1, \pm 2, \bullet\bullet\bullet$ and z_0 is the period of the corrugation. The

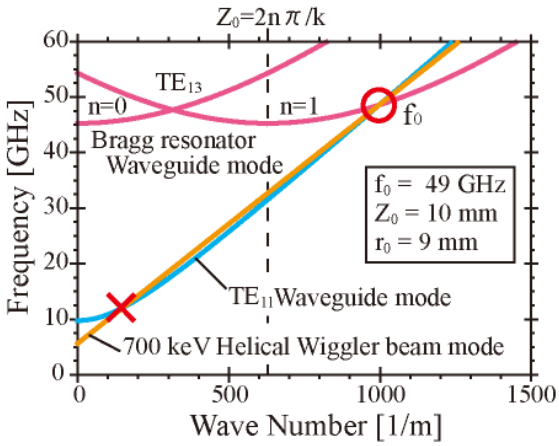

Fig. 6 Dispersion relations of FEM with ABR

waveguide mode and period of the corrugation were changed to find the triple cross point of dispersion curves of the wiggled beam, the circular waveguide and the advanced Bragg resonator. Moreover, the frequency of the triple

point must be near the cut off frequency of the advanced Bragg resonator. As shown in Fig. 6, the frequency f_0 = 49 GHz satisfied the conditions described above with the period length of the wiggler of 10 mm and TE_{13} mode of the advanced Bragg resonator. Based on these approximate estimation, precise parameters of the ABR was decided by the computer simulation.

5. Preparation of an Electron Bram

An intense relativistic electron beam (IREB) is used as a convenient energy source for the radiation sources with power of 1 GW. When intense electron beams generated by a conventional pulse line and a Marx generator are utilized, the time evolution of diode impedance because of diode plasma expansion makes the beam electron energy decrease in time. To prevent output impedance for the pulse line from decrease in time, liquid resister was set in front of the diode as a shunt register (Fig. 7).

The schematic of the experimental setup on the beam propagation is shown in Fig. 8. The

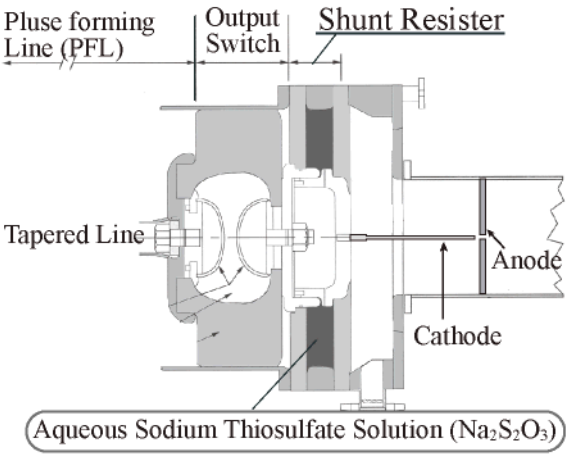

Fig. 7. Shunt resister

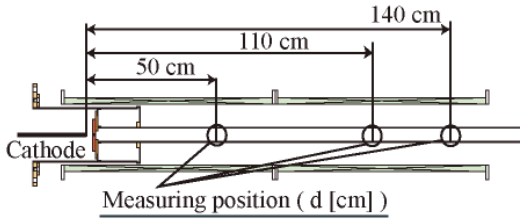

Fig. 8. Schematic of the experiment on beam poropagation.

diameter of the tungsten cathode was 3 mm. The beam was injected through a carbon anode with a 3 mm diameter hole. The diameter of the vacuum vessel was 30 mm immersed in the axial magnetic field of around 1 T.

The diode voltage showed nearly flat voltage over 100 ns as shown in Fig. 9 by using the shunt register. Though the calculated diode impedance decreased from 150 to 70 ohm (Fig. 10) the diode voltage shows nearly constane over 100 ns because of the shunt register. A dashed line in Fig. 9 indicates the calculated diode voltage without the shunt register. With the shunt register the energy variation caused by diode voltage decreased to be less than 5 %.

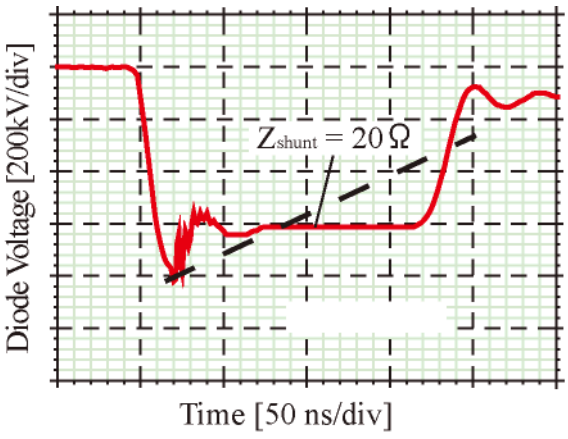

Fig. 9. Diode voltage waveform with the shunt impedance.

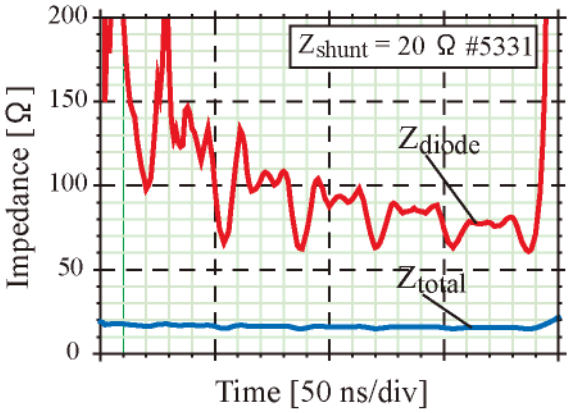

Fig.10. Diode impedance with and without shunt register.

Cross sections of the beam were observed by the damage pattern on a metal plate. A thin brass plate is located at 50,75,110 cm from the anode. After the beam hits the metal plate, we can observe the damage pattern of the beam. The observed damage patterns are shown in Fig. 11. The cross section of the beam kept the diameter of around 3 mm at 110 cm. This shows the cross section of the beam did not changed. As the diameter of the structure for the advanced Bragg resonator was expected to be around 20 mm, the beam with diameter of 3 mm is small enough to propagate through the structure.

We are now ready to carry out the experiments on the advanced Bragg resonator.

6. Conclusion

We proposed and designed an advanced Bragg resonator for higher frequency selectivity of free electron MASER. An intense relativistic electron beam with small energy decrease over 100 ns period was already prepared for the proof of principle experiment of the advanced Bragg resonator.

The energy of the beam in our normal

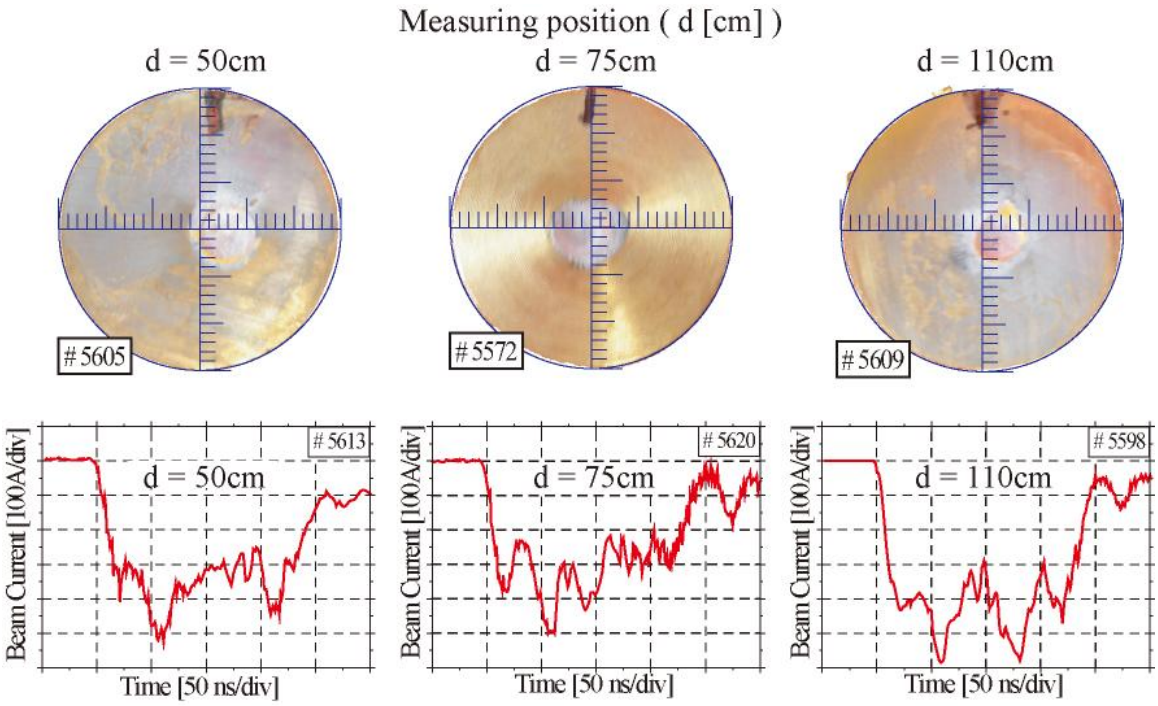

Fig. 11 Experiment results of beam propagation for long distance

operation is about 700 keV. Our estimation of the advanced Bragg resonator shows that 110 GHz radiation is possible with the beam with energy of 700 keV. However in that case, the requirements for the beam parameters and the accuracy in the construction of the resonator become more severe. We will start the proof of principle experiments for advanced Bragg resonator with appropriate frequency.

A part of this work is supported by a Grant-in-Aid for Scientific Research from Ministry of Education, Science, Sports and Culture, Japan.

References

1) P. H. Siegel, "Terahertz Technology", IEEE Trans. on Microwave Theory Tech. **50,** 910-927 (2002)
2) G. P. Gallerano, and S. Biedron, "OVERVIEW OF TERAHERTZ RADIATION SOURCES", Proceeding of the 2004 FEL Conference, 216-221 (2004)
3) V. L. Bratman, "MILLIMETER-WAVE RELATIVISTIC ELECTRON DEVICES", Radiophys. Quantum Electron., **46**, 769-781 (2003)
4)T. Idehara, H. Tsutiya, La. Agusu, H. Mori, H. Murase, T. Saito, I. Ogawa, and S. Mitsudo, "The 1 THz Gyrotron at Fukui University", Infrared and Millimeter Waves, 2007 and the 2007 15th International Conference on Terahertz Electronics. IRMMW-THz. Joint 32nd International Conference 2-9 Sept. 2007 309 - 311
5) V. L. Bratman, G. G. Denisov, N. S. Ginzburg, and M. I. Petelin, "FEL's with Bragg Reflection Resonators: Cyclotron Autoresonance Masers Versus Ubitrons", IEEE J. Quantum Electron., **19**, 282-296 (1983)
6)C. K. Chong, D. B. McDermott, M. M. Razeghi, N. C. Luhmann, Jr., J. Pretterebner, D. Wagner, M. Thumm, M. Caplan, and B. Kulke, "Bragg Reflectors", IEEE Trans. on Plasma Sci., **20**, 393-402 (1992)
7) T. S. Chu, F. V. Hartemann, B. G. Danly, and R. J. Temkin, "Single-Mode Operation of a Bragg Free-Electron Maser Oscillator", Phys. Rev. Lett., **72**, 2391-2394 (1994)
8) J. Chen, M. C. Wang, Z. Wang, Z. Lu, L. Zhang, and B. Feng, "Study of a Raman Free-Electron Laser Oscillator with Bragg Reflection Resonators", IEEE J. Quantum Electron., **27**, 488-495 (1991)
9) N. S. Ginzburg, A. M. Malkin, N. Yu. Peskov, A. S. Sergeev, A. K. Kaminsky, S. N. Sedykh, E. A. Perelshtein, A. P. Sergeev, A. V. Elzhow, "Improving selectivity of free electron maser with 1D Bragg resonator using coupling of propagating and trapped waves", Phys. Rev. Special topics accelerators and beams, **8**, 040705 (2005)

5 GHz SUPERRADIANCE USING NEWLY DESIGNED CORRUGATED WAVEGUIDE

Kousuke Aizawa, Mikiko Kawamura, Shuhei Odawara, Keiichi Kamada and Naum S. Ginzburg [a)]

Graduate School of Science and Technology, Kanazawa University, Kanazawa, Ishikawa, 920-1192, JAPAN
[a)]Institute of Applied Physics, Russian Academy of Sciences, Nizhny Novgorod, 603600, Russia

ABSTRACT

Pulsed intense electromagnetic wave with frequency around 5 GHz and duration of 4 ns was observed, when an intense relativistic electron beam with energy of 500 keV, current of 5 kA and duration of 12 ns propagated through a newly designed corrugated waveguide. Particle-in-cell code KARAT was used to redesign the corrugated waveguide. The radiated power increased to 600 MW measured by thermocouple detector. The experimental data showed good agreement with the simulated results of superradiance.

I. Introduction

Intense electromagnetic radiation sources are successfully developed with frequency of 200 GHz and output power of around 1 MW. However, radiation sources with output power over 1GW are still in an experimental stage. There are some problems with the high power radiation sources. The breakdown caused by the strong electric field of the radiation limits the output power and the duration of the radiation. The beam of low quality makes it difficult to keep the radiation conditions. An intense relativistic electron beam (IREB) is used as a convenient energy source of the radiation sources. But it is difficult to keep the beam energy and current constant because of the expansion of diode plasma. Moreover, its poor repetition rate for operation is also remained to be developed technically.

For high power sources, stimulated emission from electron bunches, i.e. superradiance (SR), is an attractive method of generating ultra short electromagnetic pulses. The SR phenomena takes place before the breakdown and the efficiency of SR is not so sensitive to the beam quality, i.e. the variation of the beam energy and current in time. Different types of SR emission (Cherenkov, cyclotron, etc.) were studied theoretically and generations of SR pulses have been observed experimentally at millimeter waveband through the frequencies 35-150 GHz [1-7]. As the peak output power emitted by SR is proportional to square of the number of electrons, the SR can be utilized as an effective radiation source with output power over 1 GW. We report here the experimental results of S-band SR using a newly designed corrugated waveguide.

2. Experimental Setup

We had reported the S-band SR with frequency of 5 GHz, duration of 4 ns and the output power of 300 MW [4]. The experimental results showed good agreement with the simulated results of SR using the Particle-In-Cell code KARAT. In the SR simulation, the relation between the duration of the beam and the length of the corrugated waveguide affected the output power. We carried out redesign of corrugated waveguide using KARAT mainly about the length and the shape of corrugation etc. for higher output power.

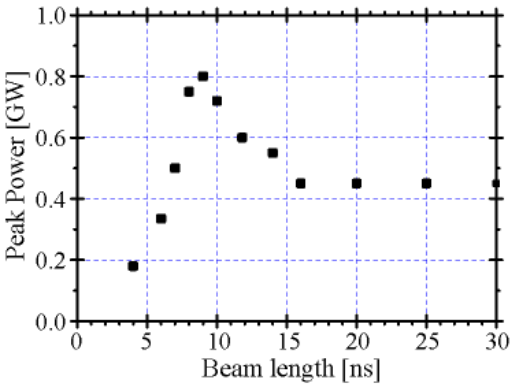

Fig. 1. For a fixed length of the corrugated waveguide, the output power shows dependency to the pulse duration of an electron beam (simulated result).

For a fixed length of the corrugated waveguide, the output power depends on the beam pulse duration of a beam as shown in Fig. 1. This is the typical characteristic of the SR. The length of the new waveguide was determined to the optimum output power for the beam with duration of 14 ns.

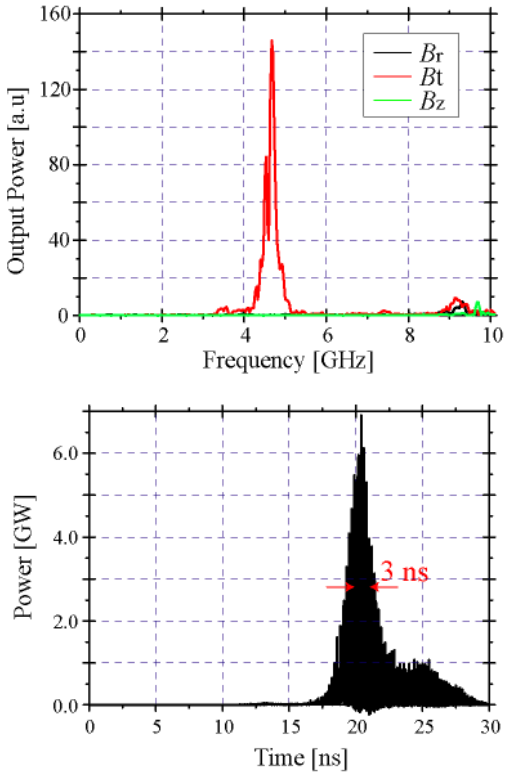

Fig. 3. Simulated spectrum of the radiated microwave (upper) and output power (lower).

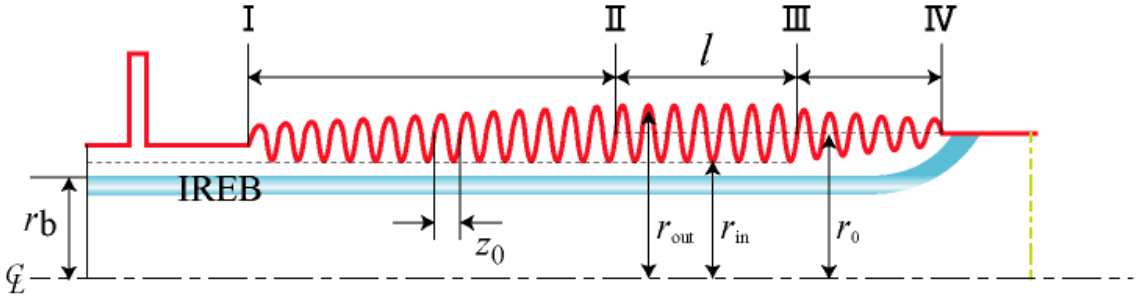

Fig. 2. New corrugated wave guide. r_b=28 mm, z_0=30 mm, r_{out}=39 mm, r_{in}=33 mm, r_0=35 mm, l= 210 mm

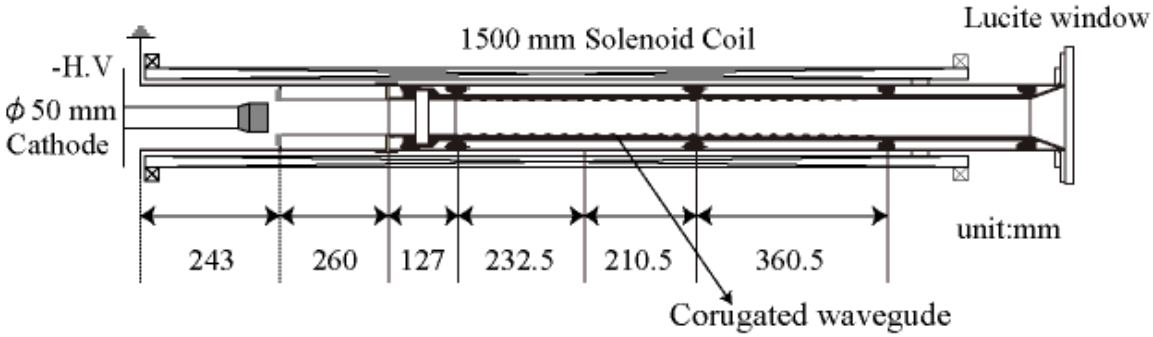

Fig. 4. Experimental setup.

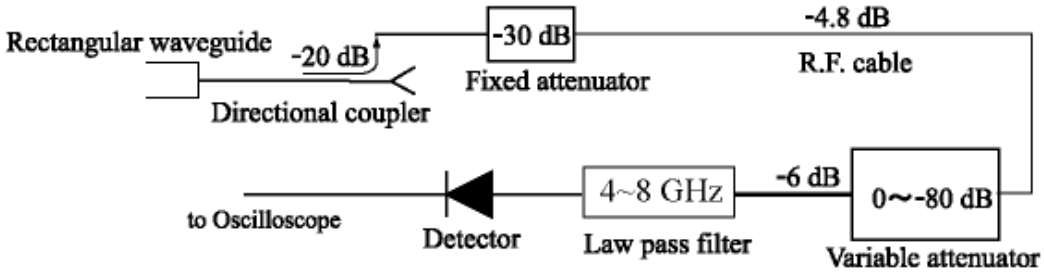

Fig. 5. Microwave measuring system.

Precise parameters of the corrugated waveguide and the beam were also examined by KARAT. To obtain higher output power, the square shaped corrugation was changed to the sinusoidal corrugation and the beam with larger radius was employed.

The newly designed cylindrical corrugated waveguide for 5 GHz SR is shown in Fig. 2 with precise parameters. With the new corrugated waveguide the radiation of the microwave pulse with frequency of 4.8 GHz , output power of 2.3 GW and duration of 3 ns was expected using the simulations by KARAT as shown in Fig. 3.

The schematic of the experimental setup is shown in Fig. 4. A hollow electron beam with energy of around 600 keV, current of 6 kA, duration of 14 ns and outer diameter of 56 mm was injected into the slow wave structure. A solenoid coil applied axial magnetic field of 1.3 T to guide the beam along the axis of the corrugated waveguide. The beam was diverged to the wall at the end of the solenoid coil. The radiated microwave through Lucite window located at the end of the vacuum tube was detected by a horn located more than 1 m far from output window. The microwave received by the horn was attenuated by two variable attenuators. Five low pass filters with frequency range from DC - 4 GHz to DC - 8 GHz were utilized (Fig. 5). Microwaves passing through the low pass filters were detected by tunnel detectors.

To estimate the output power, low power devices were utilized to calibrate the variable attenuators, low pass filters and tunnel detectors. The total output power was estimated from the

angular distribution of the microwave output. The output power was also estimated from the increase of the carbon plate temperature (calorimeter) located at the just behind the horn as shown in Fig. 6. The beam was not hit the carbon plate.

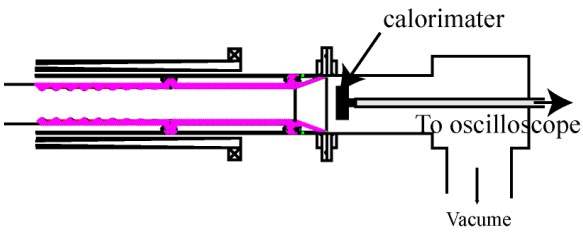

Fig. 6. Calorimeter.

3. Experimental Results

3.1 Frequency and Pulse Duration

The signals detected by tunnel detectors through low pass filters are shown in Fig. 7. Without corrugated waveguide, no signals were detected. With corrugated waveguide, similar signals were detected with DC-5 to -8 GHz low pass filters or without the filter, though no signal was observed through the DC-4 GHz. It shows that the radiated frequency of around 5 GHz was observed. The detected SR pulse duration was 4 ns that agreed with the simulated result (Fig. 3) .

3.2 Mode

Fluorescent tubes were located 500 mm far from the Lucite window to observe the radiation pattern. A donut like pattern shown in Fig. 8 was observed. It corresponds to the emission in TM_{01} mode. This result agreed with the microwave output with one peak around 20 degrees from the beam axis as shown in Fig. 10, so that the radiation mode was identified to be TM_{01} mode.

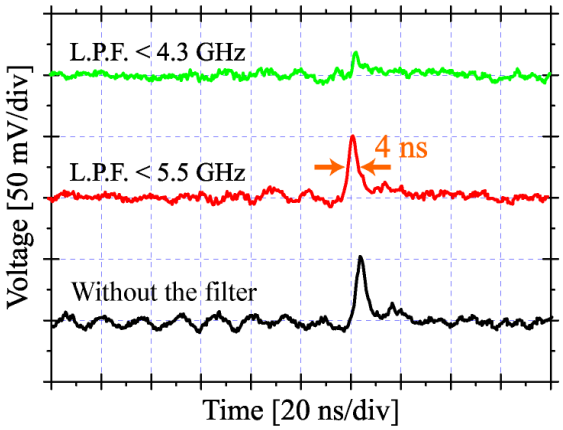

Fig. 7. The signals detected by tunnel detectors with/without low pass filters.

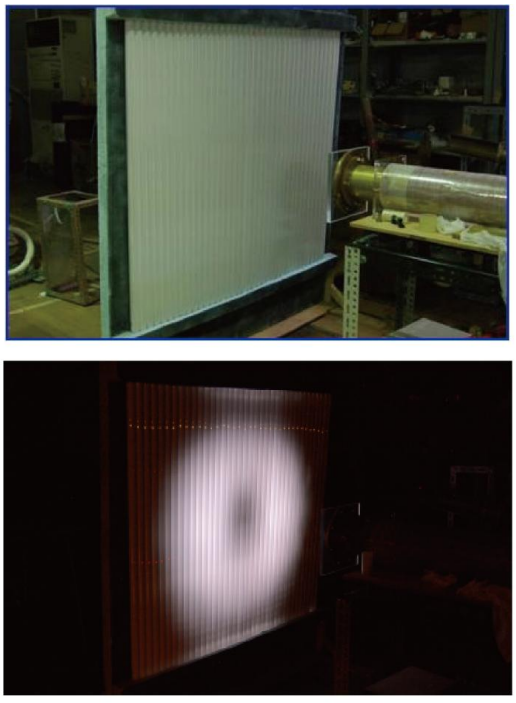

Fig. 8. Fluorescent tube located 50 cm fro the Lucite window showed the donut like pattern,

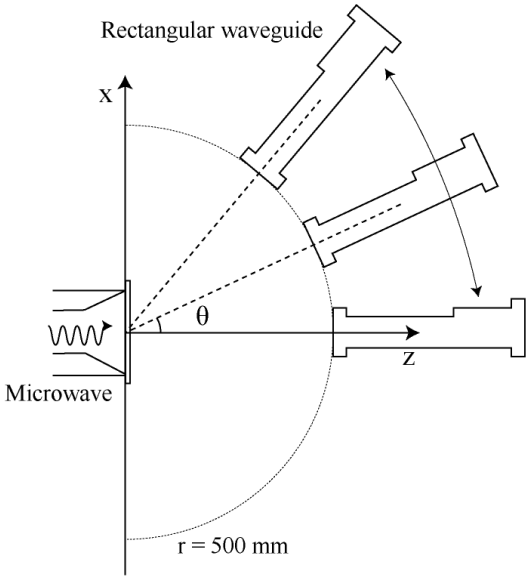

Fig. 9. Angular distribution of output power was measured along the circumference with radius of 500 mm from the center of the Lucite window.

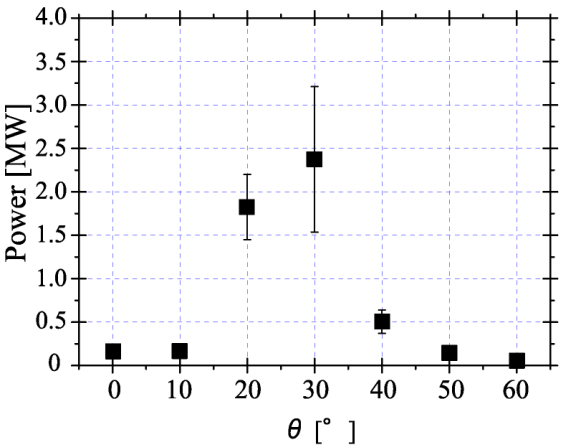

Fig. 10. The angular distribution of output power.

3.3 Output Power

The angular distribution of the radiated microwave was measured by the horn moved along the circumference with radius of 500 mm from the center of the Lucite window (Fig. 9). Total output power was estimated to be 600 MW from the angular distribution shown in Fig. 10. Total output power estimated from the calorimeter was about 400 MW. Both output power showed good agreement.

Table 1. Expeimental/simulated results

	Simulation	Experiment
Frequency	4.98 GHz	around 5 GHz
Power	2.3 GW	600 MW 400 MW (calorimeter)
Pulse duration	3 ns	4 ns
Mode	TM_{01}	TM_{01}

4. Conclusion

The experimental and simulated results are shown in table. 1. The frequency, output power, pulse duration and radiation mode showed good agreement. We concluded that 5 GHz superradiance was observed. Superradiance is an effective method of generation of ultrashort intense electromagnetic pulses with high efficiency and without rf breakdown. The frequency range of superradiance was expanded to S-band.

A part of this work is supported by a Grant-in-Aid for Scientific Research from Ministry of Education, Science, Sports and Culture, Japan.

References

1) N. S. Ginzburg, I. V. Zotova, Sov. Tech Phys. Lett., 15, pp. 573-574, 1989.
2) N. S. Ginzburg, I. V. Zotova, A. S. Sergeev, I. V. Konoplev, A. D. R. Phelps, A. W. Cross, S. J. Cooke, V. G. Shpak, M. I . Yalandin, S. A. Shunailov, M. R. Ulmaskulov , Phys. Rev. Lett., 78, pp. 2365-2368, 1997.
3) N. S. Ginzburg, N. Y. Novozhilova, I. V. Zotova, A. S. Sergeev, N. Y. Peskov, A. D. R. Phelps, S. M. Wiggins, A. W. Cross, K., He W. Ronald, V. G. Shpak, M. I . Yalandin, S. A. Shunailov, M. R. Ulmaskulov, V. P. Tarakanov, Phys. Rev. E, 60, pp. 3297-3304, 1999.
4) S. M. Wiggins, D. A. Jaroszynski, B. W. J. McNeil, G. R. M. Robb, P. Aitken, A. D. R. Phelps, A. W. Cross, K. Ronald,. V. G. Shpak, M. I . Yalandin, S. A. Shunailov, M. R. Ulmaskulov, N. S. Ginzburg, Phys. Rev. Lett., 84, pp. 2393-2396, 2000.

OBSERVATION OF HIGH-POWER MICROWAVE OUTPUT FROM NEWLLY DEVELOPPED BACKWARD WAVE OSCILLATOR FOR 10 GHz

Masatoshi Ohbayashi, Tomoaki Kurihara, Satoshi Matsuura, Sho Iwano, Ritoku Ando

Graduate School of Natural Science & Technology, Kanazawa University, 920-1192, Japan

ABSTRACT

High power microwave source have been developed for scientific purpose. Backward wave oscillator, BWO, is one of the most powerful microwave source in the medium frequency range around 10 GHz. BWO that operate at the frequency 5 GHz, was already developed, and the total power was Giga-watts class, about 630 MW. This time, BWO for higher frequency operation is newly developed. According to the simulation used in the design, total output power is expected to be about 2 GW at 10 GHz, when the electron beam of 1 MeV and 5 kA is used. Operation of the newly developed BWO is monitored in the experiment. The radiation pattern of TM_{01}-mode is checked using neon light bulbs. The operating frequency is confirmed as 10 GHz using a 100m dispersion line. The detail design and result will be presented here.

Ⅰ. Introduction

Pulse type high power microwave, HPM, sources are driven by Intense Relativistic Electron Beam, IREB. IREB is a pulsed electron beam whose energy is from hundred keV to few MeV, the current is from few kA to few tens kA, and the pulse width is from few ns to few μ s.

The peak power of HPM is from few Mega-watts to few Giga-watts, which is about thousands larger than the CW type oscillators. The HPM, realize unique applications, for examples, ablation of materials, ionization of gases, high-energy particle accelerator, *etc*. We have been developing the HPM sources for the applications. To realize the higher power density, the higher frequency is better, and the longer pulse length has benefits for high Joule. But these are competition between the efficiency and long pulse length demerit.

A backward wave oscillator (BWO) that operate at the frequency, 5 GHz, with the pulse width, 5 ns, TM_{01}-mode was already developed by us. The oscillator was developed with collaboration between K.Kamada and N.S.Ginzgurg. [1,2] It was designed based on the theory of superradiance.[1-9] In this regime, the pulse length of the electron beam is so short that the microwave, that is radiated from the electron beam, is not reabsorbed by the electron beam again. And it realize high efficiency to HPM sources. But it is only for the short pulse microwave. This time, BWO for higher frequency operation is newly developed. Because we need HPM with longer pulse length for higher Joule, normal design, that is not based on the theory of super radiance, are carried out.

Ⅱ. Design of BWO

1. Dispersion Curves

This time, BWO is developed for operation at the higher frequency, 10 GHz. Microwave is radiated from electron beam at the slow wave structure, SWS, of BWO. First, the microwave

propagates against to the electron beam, and reflected at narrow part of the drift tube by cutoff (Figure 1). The radius of the drift tube is determined by the equation.

$$f_{cutoff} = \frac{c}{2\pi r} y_{mn}$$

The f_{cutoff} is cutoff frequency, and y_{mn} is n*th* root of m*th* Bessel function ($J_{mn}(y) = 0$). Here, r is radius of waveguide. This time, the diameter of reflector was determined to 22 mm and the cutoff frequency is 10.4 GHz.

The operating frequency is determined from a cross point of dispersion curves of waveguide-mode and beam-mode.

First, we describes about beam mode. There are two mode in beam mode, cyclotron-mode and space charge-mode. Cyclotron mode is related to transverse motion of the beam electron in magnetic field. Space charge mode is related to longitudinal motion of the beam electron and plasma oscillation due to beam electron density. These modes have slow mode and fast mode. Phase velocity of the former is slower than light, and that of latter is faster than light.

These beam modes are expressed by next equations.

$$\omega = kv_z \pm \frac{\omega_p}{\gamma^{3/2}}$$

$$\omega = kv_z \pm \frac{eB_z}{m_0 \gamma}$$

Here, k is wave number, v_z is velocity of propagation, ω_p is plasma frequency, γ is the relativistic factor, m_0 is mass of electron, B_z is magnetic field.

On the other hand, waveguide mode is the mode of microwave propagating in waveguide. Waveguide mode of BWO with periodical structure is expressed with the equation.

$$\omega = c\sqrt{\left(\frac{y_{mn}}{r_0}\right)^2 + \left(k - \frac{2n\pi}{z_0}\right)^2}$$

Here, z_0 is pitch of periodical structure.

Substitute the value used in experiment, for these equations and graph out (Figure 2). As it is shown in Figure 2, line of slow space charge mode crossed with that of waveguide mode (TM_{01}) at frequency about 10 GHz.

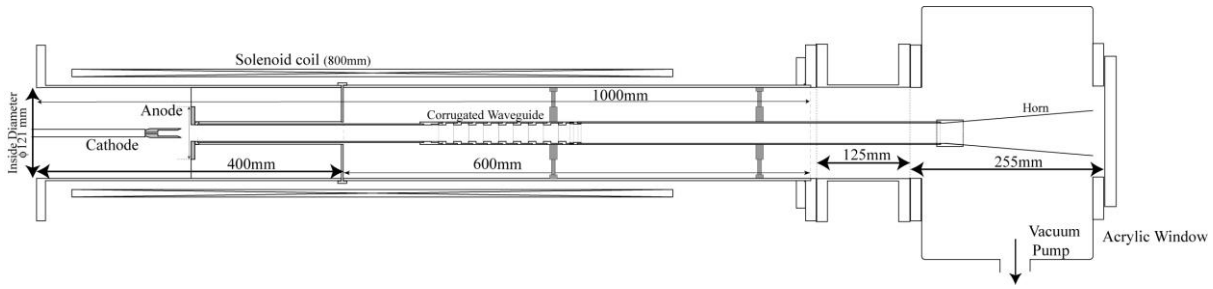

Figure 1: Setup of backward wave oscillator.

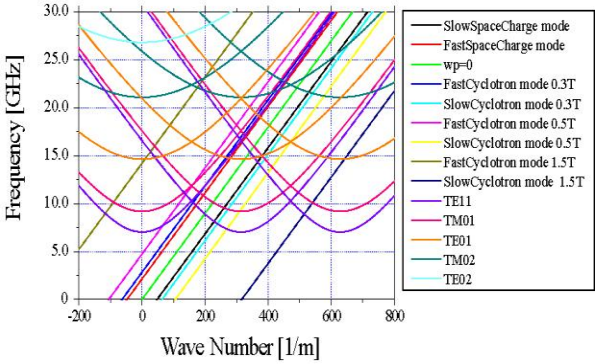

Figure 2: Dispersion curves of beam mode and waveguide mode.

2. Simulation

Electric field distribution of TM_{01} mode, which is expected for the principal radiation, is axial symmetry. The electron beam and the corrugated waveguide are axial symmetry. The 2.5-dimensional PIC-simulation code, KARAT,[10] was used to determine the optimal parameter of oscillator. The parameters, beam distance from the wall of waveguide (x), slot depth (w), length of interaction region (L_2), length of taper (L_1, L_3) and magnetic field, were changed. Figure 3 shows the model of simulation.

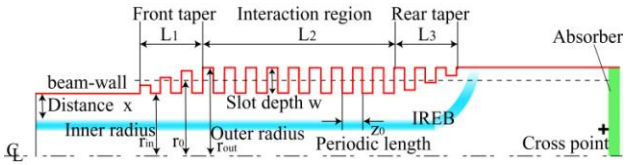

Figure 3: Model of simulation.
Cutoff wavegiude, SWS , and Output window.

First, describe about distance (x). Radius of waveguide couldn't change because of relation with reflector. Therefore, radius of the beam was changed. Figure 4 shows result. As it is shown in Figure 4, the strongest microwave is obtained when the distance was 4 mm.

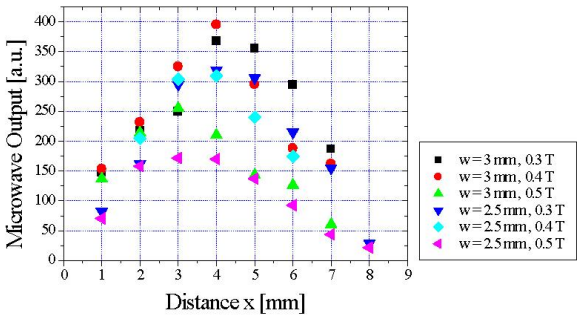

Figure 4: Distance x between beam and wall, *versus*, Peak power (Simulation).

If the beam is too close to the wall of waveguide, the beam bumps into the wall and current can't propagate enough. If the beam is far from the wall of waveguide, the beam doesn't interact enough with periodical structure. Even if the magnetic field is changed, the tendency doesn't change.

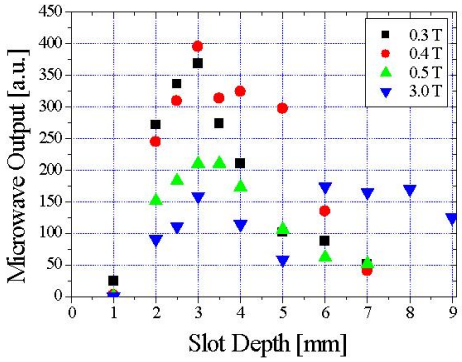

Figure 5: Slot depth of SWS, *versus*, Peak power (Simulation).

Secondary, describe about slot depth. Figure 5 is result when the slot depth is changed. When the slot depth is 3 mm, microwave output is the strongest. If the slot depth is small, interaction doesn't occur enough and output power is small. If the slot depth is too big, output power is also small. A reason of that is backward beam that occurred by the rapid changing of boundary condition.

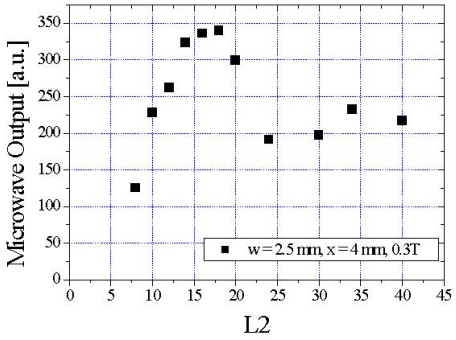

Figure 6: Length of interaction region L_2, *versus*, Peak power (Simulation).

Thirdly, describe about interaction region. Figure 6 is result when change interaction region (L_2). The taper length is not changed to change boundary condition gently. According to Figure 6, the strongest output is got when the length of interaction region is 160 mm (length of 8 slots).

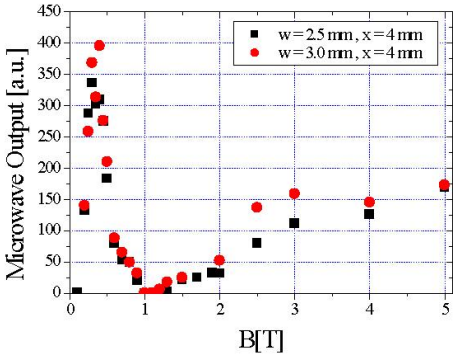

Figure 7: Magnetic field, *versus*, Peak power (Simulation).

Finally, describe about magnetic field. Figure 7 is result when change magnetic field. The magnetic field affects microwave output greatly. We got same tendency from the simulation of several slot depth. Strong output is got when the magnetic field is both weak and strong. When the magnetic field is 0.4 T, the microwave output power is the largest.

We think that reason of weakening near the 1 T is effected by the cyclotron absorption. This occur when waveguide mode interact with cyclotron mode near the frequency 10 GHz.

Ⅲ. Experimental Device

1. Beam propagation

First, we performed experiment about the beam. Figure 8 is figure of equipment.

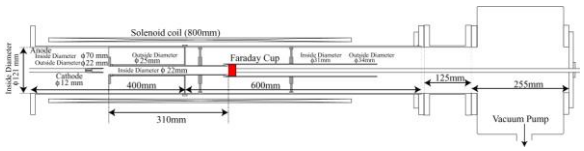

Figure 8: Setup for beam measurement.

Energy of the beam supply is 1 MeV, current of diode is 13 kA, diameter of cathode is 12 mm and that of anode is 22 mm, distance between cathode and anode is 15 mm. Degree of vacuum is under 1×10^{-4} Torr in the chamber. Set the flat surface waveguide. Solenoid coil generate magnetic field to prevent the beam from divergence.

Measurement equipment is Faraday cup that is made up of carbon collector and shunt resistance. Position of Faraday cup is 400 mm far from anode. We measure the beam current. Carbon collector catches beam and almost all beam current flows to ground. Then, measured voltage of shunt resistance and calculate the beam current.

We also observed the shape of the beam cross-section. Set the aluminum blackened plate at the far from 310 mm. It thickness is 0.7 mm. The beam damaged the plate.

2. Measurement of radiation

Part of diode is same parts when the beam experiment. Set the corrugated waveguide. Position of interaction region is middle of solenoid coil. This

BWO has horn to radiate microwave to free space. Window is acrylic that thickness is 15 mm.

First, we check the radiation of microwave with neon lamp screen that is putted 484 neon lamps evenly in square shape. Distance between each lamp is 12 mm. Distance from the window to screen is 275 mm (Figure 9).

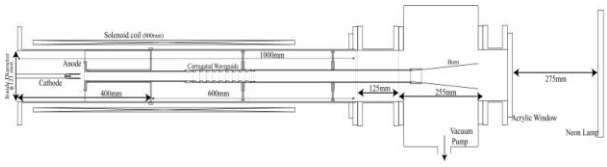

Figure 9: Setup for radiation.

We also identified frequency with a 100 m dispersion line. Propagation velocity in the waveguide is different by frequency. We specified frequency with this differ. Way of that is useful when pulse width is enough shorter than propagation time. This time, pulse width is 50ns. It is enough shorter than propagation time in the dispersion line (360 ns for light).

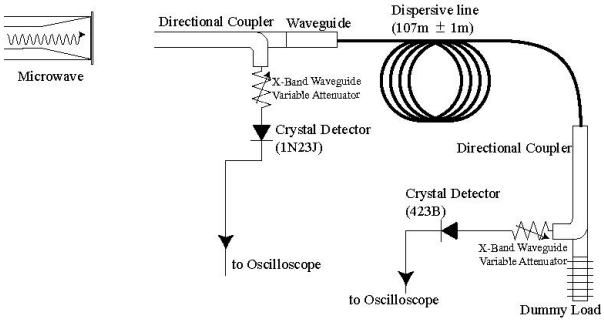

Figure 10: X-band dispersive delay line.

Ⅳ. Result and Discussion

1. Beam experiment

Figure 11 shows the result measurement of beam current. This is beam current in several magnetic fields. When the magnetic field is above 0.5 T, beam current is steady near 5 kA. On the other hand, below 0.5 T, beam current decrease with decreasing magnetic field. Weak magnetic field can't control beam and beam bump into the wall of waveguide.

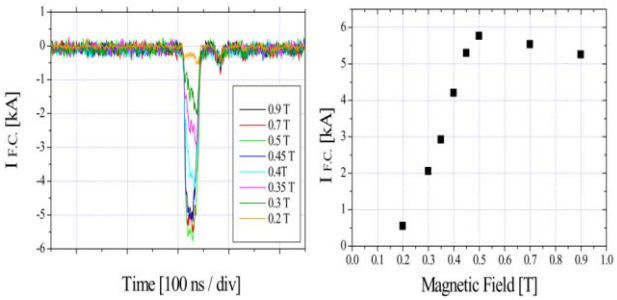

Figure 11: Propagated beam current, *versus*, Magnetic field strength (Experiment).

Next, we observed the shape of beam cross-section. Figures.12-15 are results in the several magnetic fields. According to the result, damage is small at weak magnetic field. Shape and size of beam is that expected in simulation. Enough current can be obtained, when the magnetic field is over 0.5 T.

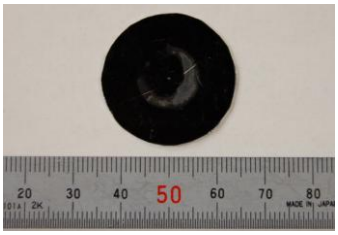

Figure 12: Beam patterns for 0.3 T

Figure 13: Magnetic field, 0.4 T

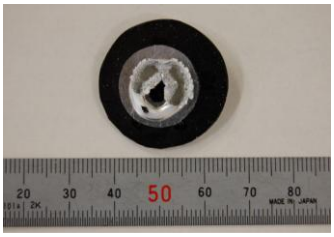

Figure 14: Magnetic field, 0.5 T

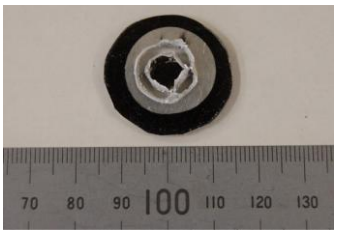

Figure 15: Magnetic field, 0.7 T

2. Radiation Experiment

We checked microwave radiate or not by the neon lamp. This result is in several magnetic fields (Figures 16-19). Neon lamp emitted. Microwave is radiated. The emission of the 0.7 T and 0.9 T is weaker than that of 0.45 T. Same tendency is also confirmed in result of simulation.

Figure 16: Setting of Neon lamps panel.

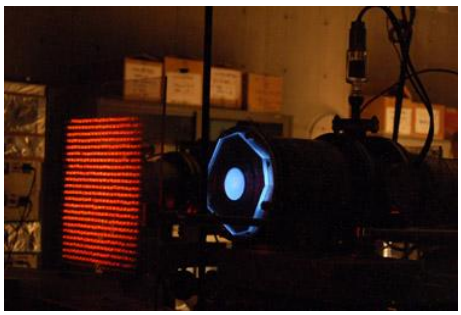

Figure 17: Radiation pattern from output window. Magnetic field, 0.45 T

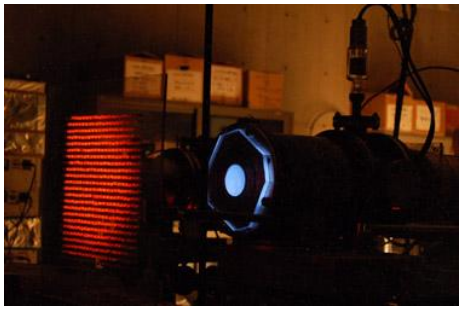

Figure 18: Magnetic field, 0.7 T

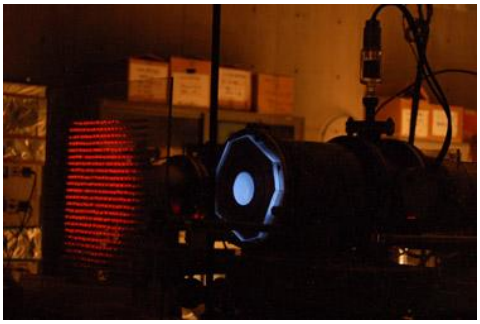

Figure 19: Magnetic field, 0.9 T

Beam current is unchanged if the magnetic field is changed. Therefore, beam is not reason for decreasing output. We think cause of that is cyclotron absorption.

Next is measurement of frequency. Relation between frequency and propagation time becomes as it is shown in Figure 20. As shown in a figure, the range with effective resolution is about 8 GHz to 13 GHz. The results are shown in Figures 21 -23.

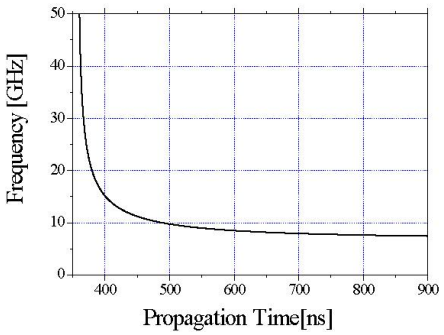

Figure 20: Frequency, *versus*, Propagation time.

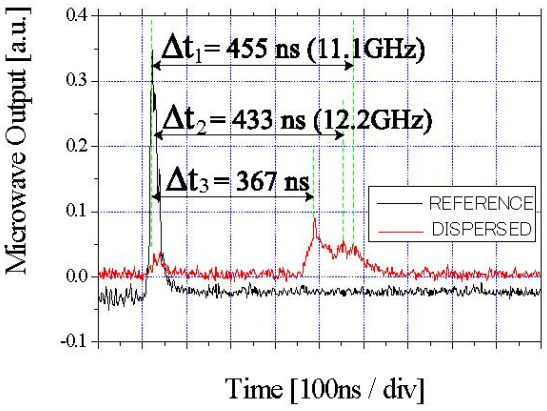

Figure 21: Signals before and after 100 m dispersive line. Magnetic field, 0.45 T

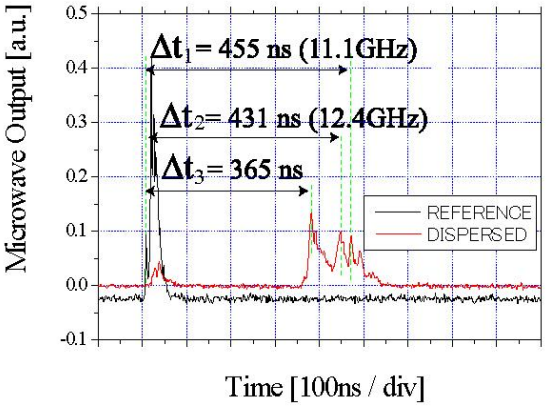

Fig.22: Magnetic field, 0.6 T

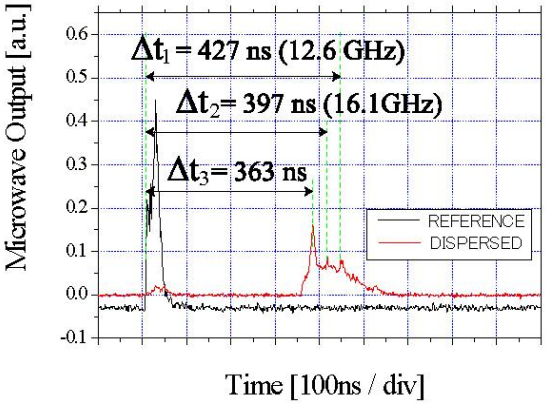

Figure 23: Magnetic field, 0.7 T

As show in the results, the radiation frequency is between 10 GHz and 12 GHz. Even if magnetic field changes, the frequency seldom change. This reason is that the oscillation mechanism is Cherenkov type and not depending on magnetic field strength. In spite of this fact, the output power changes with the field strength. And has a maximum between 0.4 T and 0.7 T in the experiment. The optimal field strength is 0.65 T. The output power drops for the magnetic field over 0.75 T (Figure 24). The dependency of the microwave output power to the magnetic field is similar to that of the simulation.

There is a difference in the optimal field strength between the experiment and the simulation. It may be explained by the degradation of beam propagation at weak field condition, see figure 11. The decrease of beam current is severer than that of simulation under 0.5 T.

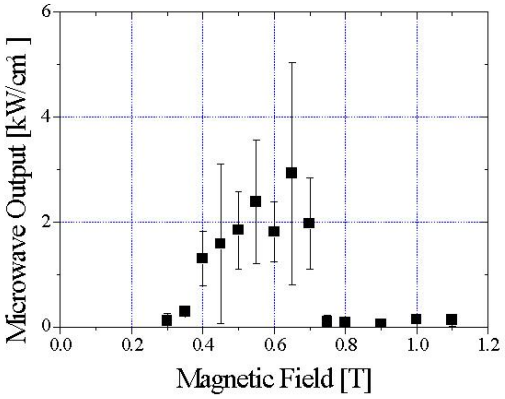

Figure 24: Microwave output, *versus*, Magnetic field (Experiment).

Summary

We designed Backward Wave Oscillator frequency is 10 GHz and developed it. The optimal design is decided by a simulation. In the simulation, output power is about 2 GW, the frequency is 9.6 GHz. In the experiment, magnetic field more than 0.5 T is necessarily to propagate the electron beam. The microwave radiation and the frequency are measured. The radiation pattern shows that it oscillates with

TM_{01} mode, as expected. The frequency is measured by using a dispersive line, and it is about 10 GHz. There is optimum magnetic field, where the microwave output power becomes peak, both in the simulation and experiment.

References

1) N.S.Ginzburg, I.V.Zotova, R.M.Rozental, A.S.Sergeev, M.Kamada, K.Kurihara, H.Shirasaka, R.Ando, K.Kamada, "Increasing superradiant pulse peak power by using electron energy chirp", *Nuclear Instruments and Methods in Physics Research A, vol.507, pp. 61-64 (2003).*
2) N.S.Ginzburg, I.V.Zotova, R.M.Rozental, A.S.Sergeev, M.Kamada, K.Kurihara, H.Shirasaka, R.Ando, K.Kamada:, "Optimization of electron bunch profile for increasing peak power of superradiance pulses", *Opt. Comm., vol.231, no.1-6, pp.303-308 (2004).*
3) R.H.Dicke, "Coherence in Spontaneous Radiation Processes", *Phys.Rev. vol.93 number 1, pp.99-110 (1954).*
4) N.S.Ginzburg *et al*., "Generation of powerful subnanosecond microwave pulse by intense electron bunches moving in a periodic backward wave structure in the superradiative regime," *PHYSICAL REVIEW E vol.60, number.3, pp 3297-3304 (1999)*
5) N.S.Ginzburg *et al*., "Increasing of peak power of superradiation pulses by variation of accelerating voltage", *AIP Conference Proceedings, vol.650, pp.23-28 (2002).*
6) N.S.Ginzburg *et al*., "Experimental observation of cyclotron superradiance under group synchronism conditions", *Sov. Tech Phys. Lett., vol.15, pp.573-574 (1989).*
7) N.S.Ginzburg *et al*., "Cyclotron superradiance of a moving electron bunch under group synchronization conditions", *JETP Letters, vol.60, no.7, pp.513-517 (1994).*
8) N.S.Ginzburg *et al.*, "Theory of the undulator superradiance of an electron beam pulse in the group synchronism regime", *Sov. Tech. Phys. Lett., vol.25, No.4, pp. 296-299 (1999).*
9) V.G.Shpak, M.I.Yalandin, N.S.Ginzburg, *et al*., "A new source of ultrashort microwave pulses based on the effect of superradiance of subnanosecond electron bunches", *Doklady Phys.RAS, vol.44, pp.143 (1999).*
10) V.P.Tarakanov, *User's Manual for Code* KARAT, *ver.*7.09, (1999).

CONVERSION OF 5 GHz MICROWAVE TO LINEAR POLARIZATION AND THE EFFICIENCY.

Tomoaki Kurihara, Masatoshi Ohbayashi, Sho Iwano, Satoshi Matsuura, Ritoku Ando

Graduate School of Natural Science & Technology, Kanazawa University

920-1192, Japan

ABSTRACT

A quasi-optical antenna, called Vlasov antenna, is studied for launching the TM_{01} mode microwave from a waveguide to Gaussian mode in free space. The antenna designs are carried out by using geometrical optics without taking in to diffraction effect. Geometrically, conversion efficiency can be independent on the design. Several antenna designs are tested and its conversion efficiency is investigated at the wavelength 6 cm, *i.e.* 5 GHz that is comparative to the diameter of wave guide. The efficiency can be improved by increasing the diameter of the final waveguide. It changed from 15 % to 75 % in the experiment.

I. Introduction

High power microwaves (HPM) is similar to Laser. Both of them are similarly categorized into a continuous wave (CW), or pulse. The CW oscillators, *e. g.* gyrotron, have been achieved Mega-Watts level output power. On the other hand, pulse type HPM achieves Giga-Watts level. The peak power of pulse HPM is about thousands times larger than that of CW. The electric field is so strong that discharge in atmospheric pressure air is possible without electrodes. [(1)] Discharge on surface of dielectric materials is also possible. [(2)] The pulse duration of HPM can become few nano-seconds and more short. A calorie of the pulse, which is about few Joules, is not high. It makes free targets from heat.

Generally pulse operation has advantage of being able to lower average of electric power, and reduce the size of electric power supply, and evade a problem of heat for the production and transport. The shorter the pulse duration is, the higher the threshold value of discharge tends to be. [(3)] For the present, pulse HPM is not studied very much in this country. Hence we have been studying about generation of short pulse HPM, the application, and proper propagation for it.

Wavelength is much longer than Laser, and the frequency is much lower than it. Properties to dielectric materials are so different for the two electromagnetic waves. Techniques to transport are also different. The microwave can be transport by using metallic cable, metallic waveguide and strip line in substrate, and so on.

Especially, antenna for launching the 5 GHz high power microwave from waveguide to free space is important for future applications. We will report the result of conversion from output of BWO (TM_{01} mode) into linear polarization (TEM_{00} mode). A quasi-optical antennas, which is called Vlasov antenna, is examined. Especially the antenna size and the conversion efficiency is discussed here.

1I. Mode converter

〈2・1〉 Vlasov antenna

Vlasov antenna is consisting of a step-cut waveguide (SC-waveguide) and a cylindrical parabola mirror (CP-mirror), see figure 1. [(4)] First, SC-waveguide radiates the microwave against to the CP-mirror. Second, CP-mirror reflects the radiated rays and makes parallel ray before launching. The focal points of the CP-mirror are aligned along the axis of the SC-waveguide.

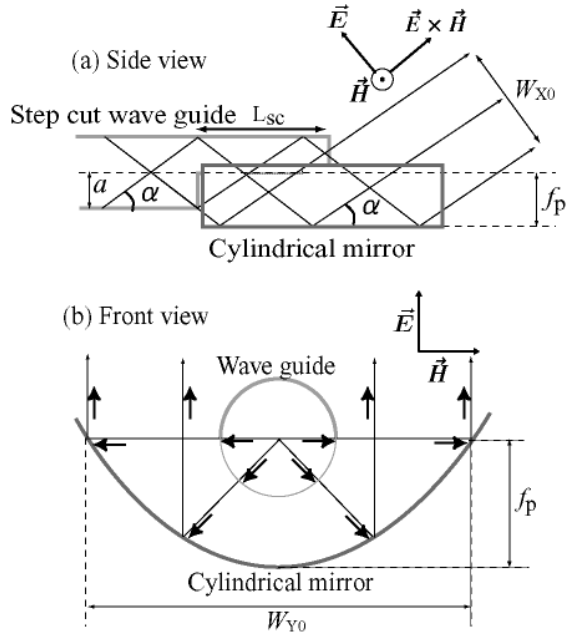

Figure 1 Vlasov antenna.

〈2･2〉 Design by geometrical optics

In this section, we mainly explain about a SC-waveguide. Propagating microwave in a waveguide is assumed to be a plane wave. In circular waveguide, the relation between wavelength in waveguide and one in free space is given by

$$\left(\frac{2\pi}{\lambda_0}\right)^2 = \left(\frac{2\pi}{\lambda_z}\right)^2 + \left(\frac{\zeta_{n,m}}{a}\right)^2 \quad \cdots\cdots (1)$$

The λ_z is wavelength in waveguide, and λ_0 is one in free space. "a" is radius of waveguide. The $\zeta_{n,m}$ is the mth solution of Bessel function $J_n(x)$. In the case of TM_{01} mode, $\zeta_{0,1}$ is 2.40. In addition, eq.(1) changes to next relation given by

$$k_0^2 = k_z^2 + k_\perp^2 \quad , \cdots\cdots (2)$$

where $k_\perp$ is the wave number in vertical direction $k_\perp = (\xi_{n,m} / a)$. Thus emission angle α is given by

$$\alpha = \sin^{-1}\left(\frac{k_\perp}{k_0}\right) = \frac{\lambda_0 \xi_{n,m}}{2\pi a} \quad \cdots\cdots (3)$$

In the cross sectional plane, TM_{01} mode is axis symmetric. And microwave is treated as standing wave. Consequently two waves bouncing between the two walls have negative and positive $k_\perp$. The two waves go across each other, which have the same amplitude.

At the end of waveguide, two waves go straight keeping the two angles of $\pm\alpha$. In the front view, all rays are emitted from the axis of the waveguide just as a point source. After being reflected at the CP-mirror, the wave fronts become parallel.

In the side view, half of ray comes out directly and the other half is reflected at the roof of SC-waveguide. These two rays are merged, and the width of the ray becomes twice. Figure 2 shows the contour of microwave in the propagation.

It is satisfied in both TE and TM mode. The electric field and magnetic field are replaced for TE and TM

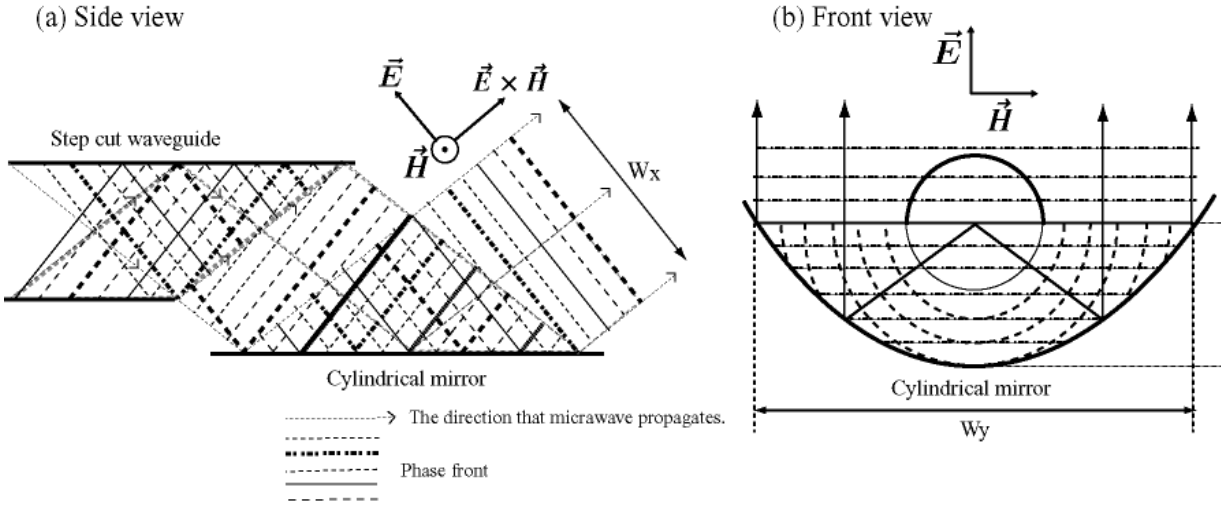

Figure 2: Paths of microwave ray in antenna

modes. The planes of polarization of waves launched from antenna are rotated 90 degrees between the two modes.

We take the *Z*-axis in the direction of beam propagation. The *X*-axis is taken to be perpendicular to *Z*-axis and the reflector. The *Y*-axis is taken to be perpendicular to *X*-axis and *Z*-axis. For TM mode, the electric field is polarized to *X*-direction, and the magnetic field to *Y*-direction.

Thinking geometrically, an aperture of Vlasov antenna is given by following relations.

$$W_x = 4a\cos\alpha \qquad \cdots\cdots(4)$$
$$W_y = 4f_p$$

Here f_p is a focal length of a CP-mirror. According to eq.(4), the size of the aperture is decided only *a* and f_p.

〈2･3〉 Gaussian beam

Gaussian beam has a parameter named "spot size", which is a radius that electric field become 1/*e*, the power does 1/e². Focusing ray, spot size has a minimum value at some place. The place is called "beam waist", at which wave front becomes in the flat, and microwave is converted into linear polarization completely. It is influence of diffraction; spot size varies along to propagation. Spot size is often treated as beam radius, and we can write next relation about it. [5]

$$\omega_{(z)} = \omega_0\left[1+\left(\frac{\lambda_0 z}{\pi\omega_0^2}\right)^2\right]^{1/2} \qquad \cdots\cdots(5)$$

The $\omega_{(z)}$ is spot size after *z* propagation, and ω_0 is a minimum size at beam waist. Using this relation, we can calculate the spot size after propagation by ω_0 easily. Additionally, when $z >> \omega_0$, we can rewrite eq.(5) to next relation,

$$\omega_{(z)} = \frac{\lambda_0 z}{\pi\omega_0} \qquad .\cdots\cdots(6)$$

The $\omega_{(z)}$ is the size that power becomes to e^{-2}, therefore, we can write the following relation about power density.

$$I(x,y) = \frac{2P_0}{\pi\omega_x\omega_y}\exp\left(-\frac{2x^2}{\omega_x^2}\right)\exp\left(-\frac{2y^2}{\omega_y^2}\right) \qquad \cdots\cdots(7)$$

Here, $I_{(x,y)}$ is the power density at the coordinates, P_0 is the total power, ω_x and ω_y are the spot sizes of each directions. On the beam axis (Z-axis), it is assumed that $x = y = 0$, and (7) is able to be rewritten that

$$P_0 = \frac{I_0}{2}\pi\omega_x\omega_y \qquad .\cdots\cdots(8)$$

According to eq.(8), we can estimate the total power of Gaussian beam by the power density and spot sizes.

By the way, we assumed that microwave is converted into linear polarization at the focal plane of reflector previously. It is assume that the focal point of reflector is the position of a beam waist (*Z*=0). The minimum spot sizes in *X* and *Y* direction at beam waist were supposed geometrically. We can write next relations about the Vlasov antenna.

In this time, we chose the four types of SC-waveguide. They were three different radius waveguides (*a* = 3.0 cm, 3.6 cm, 4.98 cm). Thinking geometrically, conversion efficiency doesn't depend on the radius of waveguide (ω_0 depends on radius). But 5 GHz microwave, which we used in this time, has much longer wavelength than millimeter-wave, it was possibility that the antenna was under influence of diffraction. For this reason, we made three types of SC-waveguide. We show the sizes of antennas and spot sizes at *Z* = 0 cm (beam waist), 50 cm, 75 cm, 100 cm (Table 1).

III. Experiment Ⅰ

〈3･1〉 Setting

We set a horn antenna at the end of BWO to prevent the HPM from reflecting on the end of the waveguide. The radius of the horn antenna was 5.0 cm. In the later experiment we set a Vlasov antenna at the rear of the horn antenna for mode conversion.

Table 1.
Design of three antennas, and the spot sizes after launched (calculated).

Type	Ⅰ	Ⅱ	Ⅲ
a	3.0 cm	3.6 cm	4.98 cm
f	6.0 cm	6.0 cm	8.0 cm
α	49.8 degree	39.7 degree	29.7 degree
*L*sc	5.5 cm	14 cm	29 cm
Z = 0 cm ($\omega_X \times \omega_Y$)	3.8 cm × 12 cm	5.5 cm × 12 cm	8.7 cm×16 cm
Z = 50 cm	25.1 cm × 14.4 cm	18.2 cm × 14.4 cm	14 cm × 17.1 cm
Z = 75 cm	37.4 cm × 17 cm	26.6 cm × 17 cm	18.6 cm × 18.4 cm
Z = 100 cm	49.8 cm × 20 cm	35.1 cm × 20 cm	23.6 cm × 20 cm

〈3･2〉Detecting power

Waveforms of detecting power from BWO are shown in figure 3. After entering a rectangular waveguide, the microwave passed through directional coupler, and it was attenuated by attenuators and cable (Figure 4). At last it was detected by tunnel detector, and checked the frequency with low pass filter (L.P.F). The resolution of L.P.F is limited to 1 GHz; therefore, this measurement is not too strict. However, HPM could not be detected not over 4 GHz. Additionally the detected waveform is like to simulation that was showed in figure 5. Thus we think that microwave oscillate in almost 5 GHz.

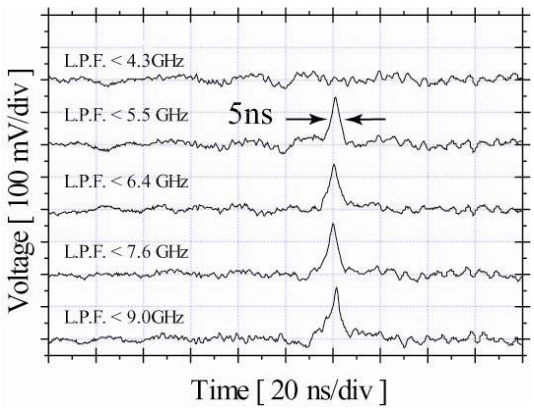

Figure 3. Waveforms of microwave detected after passing L.P.F s.

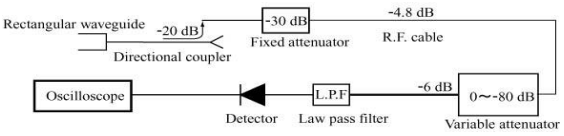

Figure 4. Microwave detecting system.

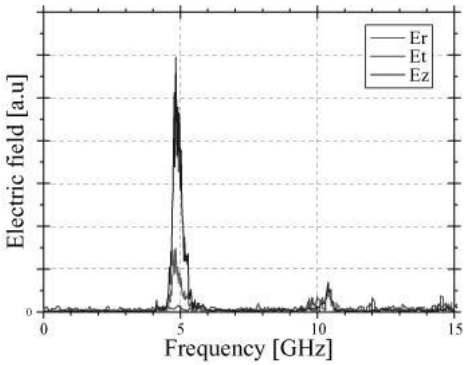

Figure 5. Frequency spectrum of BWO output (Simulation).

〈3･3〉Total power before conversion

Detecting microwave, the receiving antenna shaped rectangular horn was set in front of the emission antenna. We measured the power while changing the position (Figure 6). The result of measurement is presented in Figure 7.

The total power is assumed by integrating the graph of power distribution. For example, the total power was about 160 MW as a result of Figure 7.

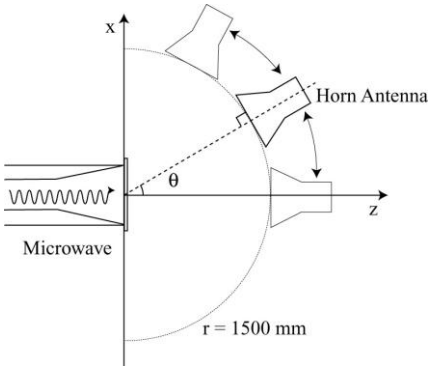

Figure 6. Power detecting method.

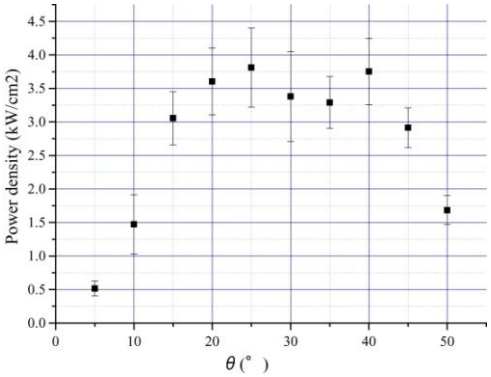

Figure 7. Power density profile before mode conversion *vs.* radiation angle.

Emission patterns are shown Figure 9.

In the last section, we wrote that the conversion efficiency is independent on the radius of the waveguide according to geometric optics. However, it is evident that the emission patterns were under influence of the radius of waveguide. The bigger the radius is, the more strongly fluorescent tubes shined.

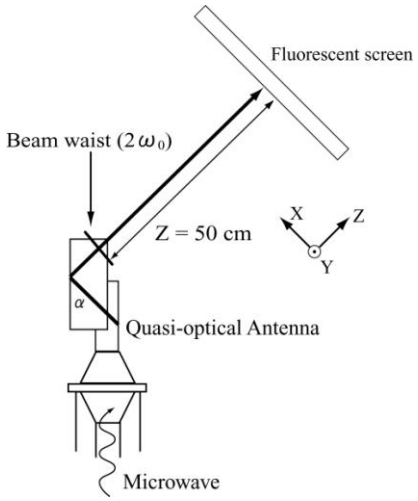

Figure 8. Vlasov antenna. Radiation pattern are measured by fluorescent tubes array which is set at the distance of 50 cm.

Ⅳ. Experiment Ⅱ

〈4･1〉 Setting of a Vlasov antenna

Vlasov antenna was set behind the horn antenna. In this time, the CP-mirror was set to be parallel to Y-direction. Y-direction is parallel to the plane of the CP-mirror.

In consequence, the direction of electric field was parallel to X-direction that is parallel to the ground. And Z-direction is perpendicular to X and Y-direction.

〈4･2〉Measurements of emission patterns with fluorescent tubes

Irradiating a microwave to a fluorescent tube, it brightens up. The threshold value that a fluorescent tube brightens is about 20 kW/cm^2. And so, arraying fluorescent tubes in the shape of a screen, we observed emission patterns. A fluorescent screen was set at the distance of 50 cm from Vlasov antenna, and was perpendicular to *Z*-axis (Figure 8).

(a) a = 3.0 cm

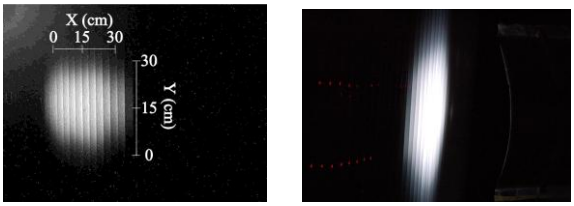

(b) a = 3.6 cm **(c)** a = 4.98 cm

Figure 9. Emission pattern from quasi-optical antennas.

〈4･3〉 Measurements of detecting

We measured the power with each Vlasov antenna. The same detecting system at the preceding section was used. The receiving antenna was set at

Table 2. Results of the experiments

Type	a	spot size(calculation) ($\omega_X \times \omega_Y$)	spot size(experiment) ($\omega_X \times \omega_Y$)	total power	coversion efficiency
Ⅰ	3.0 cm	25.1 cm × 14.4 cm	26.3 cm × 18.3 cm	15 MW	15 %
Ⅱ	3.6 cm	35.1 cm × 20 cm	41.5 cm × 23.5 cm	65 MW	41 %
Ⅲ	4.98 cm	23.6 cm × 20 cm	22.5 cm × 18.6 cm	75 MW	75 %

the distance of Z=50 cm when Type Ⅰ antenna was used, at Z=100 cm when Type Ⅱ and Type Ⅲ. The distributions were measured along *X* and *Y* axis every 5 cm around a peak (Figure 10). The total power before mode conversion was about 160 MW when Type Ⅱ, and about 100 MW when Type Ⅱ and Type Ⅲ.

The results of measurements are shown at Figure 11. The line in the graph is Gaussian curve. It is assumed that the Vlasov antenna could convert TM_{01} mode into linear polarization.

To approximate these graphs by eq.(7), ω_x and ω_y were decided. And the total power was estimated by spot sizes and peak power using eq.(8). Spot size and conversion efficiency were shown in table2. The more it enlarges the radius of the SC- waveguide, the more efficiency has improved. In the best value, it was 75%. In general, the efficiency of Vlasov antenna is confirmed that it is about from 80 % to 90 %[(4)(6)]. Therefore this value is reasonable.

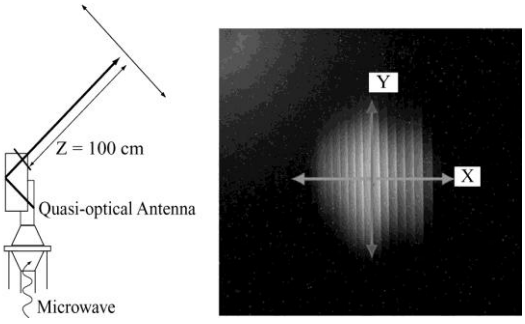

Figure 10. Radiation pattern measured by floresent tubes array.

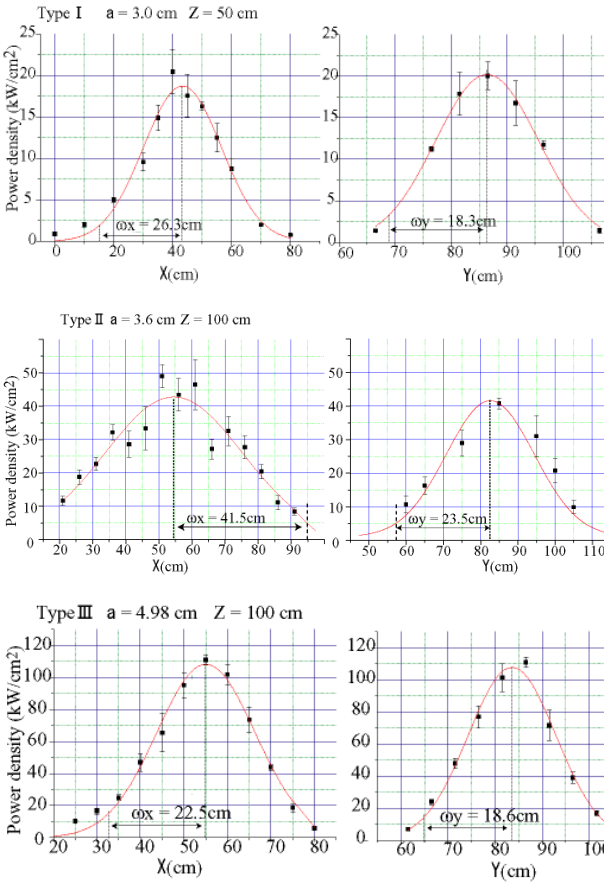

Figure 11. Profiles of Gaussian beam for each antenna designs.

Ⅴ. Conclusion

The Vlasov antenna is designed by geometric optics. This antenna is able to convert TM_{01} mode into linear polarization. The conversion efficiency has improved by enlarging the radius of SC-waveguide. The efficiency is 75 % in the best value. This enables us to apply the HPM to plasma generation and ablation, etc. And we'll study the Vlasov antenna for microwave for future.

This research was partially supported by the Ministry of Education, Science, Sports and Culture, Grant-in-Aid for scientific research (C), 2005, 17540466.

Reference

1) Y. Oda, *et al*, "Atmosphere pressure dependence of the microwave rocket's performance powered by a high power gyrotron", J. Plasma Fusion Res., Vol.83, No.3, pp. 296-299(2007)
2) N. S. Ginzburg, N. Yu. Novozhilova, I. V. Zotova, A. S. Sergeev, and N. Yu. Peskov : "Generation of powerful subnanosecond microwave pulses by intense electron bunches moving in a periodic backward wave structure in the superradiative regime." Physical Review, Vol.60, No.3, pp. 3297-3303 (1999)
3) S. Bhattacharjee and H. Amemiya : "High power sharp pulse microwave discharge : interpulse regime." Fusion and Plasma Physics, Vol.22C, pp.2595 - 2598 (1998)
4) S. N. Vlasov, L. I. Zagryadskaya and M. I. Petelin: "Transformation of a whispering gallery mode, propagating in a circular waveguide, into a beam of waves." Radiofizika, Vol.15, No.12, pp.14-17 (1972)
5) O. Fukumitsu, "Approach to optical electronics" , Shoukoudou(1988), in Japanese
6) S. N. Vlasov, I. M. Orlova, "Quasi-optical transformer which transforms the waves in a waveguide having a circular cross section into a highly directional wave beam", Radiofizika, Vol.17, No.1, pp. 148-154(1974)